UNIVERSITY OF CALIFORNIA

Santa Barbara

# Heterogeneous Integration for Reduced Phase Noise and Improved Reliability of Semiconductor Lasers

A dissertation submitted in partial satisfaction of the

requirements for the degree Doctor of Philosophy

in Electrical and Computer Engineering

by

Sudharsanan Srinivasan

Committee in charge:

Professor John Bowers, Chair

Professor Larry Coldren

Professor Luke Theogarajan

Professor Rod Alferness

June 2015

The dissertation of Sudharsanan Srinivasan is approved.

_____
Larry Coldren

_____
Luke Theogarajan

_____
Rod Alferness

_____
John Bowers, Committee Chair

June 2015

Heterogeneous Integration for Reduced Phase Noise and Improved Reliability of Semiconductor Lasers

Copyright © 2015

by

Sudharsanan Srinivasan

*Dedicated to my parents Srinivasan and Lakshmi*

ACKNOWLEDGEMENTS

I will be forever grateful to my adviser, Prof. John Bowers, for all his help throughout my time at UCSB. To begin, he provided an excellent opportunity to perform cutting edge research in photonics by accepting my application to join his group. His passion for research is something that all his students strive to achieve. I have certainly grown to see him as a role model for me on how to be an effective researcher, through determination and constant hard work. His commitment to provide every student in his group a fair chance of reaching his/her project goals even if it requires purchasing state of the art equipment or other material is commendable. His intuition to research methodology is unique and has prevented many distractions or tangential pursuits and hurdles in my research. I would also like to thank him for giving me exposure to the broader research community through conference travels, even if I did not have a paper to present.

Next, I would like to thank my committee members Prof. Luke Theogarajan, Prof. Larry Coldren and Prof. Rod Alferness for their inspiration and guidance in my research work. I would also like to thank the following faculty members, Prof. Nadir Dagli, Prof. Dan Blumenthal, Prof. Pierre Petroff, Prof. Chris Palmstrom, Prof. Mark Rodwell, Prof. Chris Van-de-Walle, Dr. Milan and Dr. Dan Cohen, for their coursework and excellent teaching which has taught me a great deal at an accelerated pace. I would like to thank the staff members, Ceanna, Alyssa, Christine, Shannon and Val for taking care of the paper work and purchasing a never ending list of equipment. Your dedication in what you do gives the students strength and peace of mind to focus on research.

I would like to thank my friends at Aurrion, Alex Fang, Anand Ramaswamy, Byungchae Kim, Jeff Wise, John Hutchinson, Eric Hall, Greg Fish and Erik Norberg for allowing us to

use their testing facility and providing mask space and fabricating some of the lasers shown in this thesis. Alex Fang and Anand Ramaswamy were great mentors in the beginning and helped me acclimatize to the new and fast paced research environment.

I would like to thank all Bowers group members, present students and alumni/ alumnae for their support when I had questions related to research or otherwise: Di Liang, Martijn Heck, Yongbo Tang, Doaxin Dai, Jonathan Doylend, Andy Chang, Sid Jain, Geza Kurczveil, Molly Piels, Ben Curtin, Jared Bauters, Hui-Wen Chen, Tony Lin (Chieh-Ting), Jock, Nick Julian, Michael Davenport, Daryl Spencer, Chong Zhang, Jared Hulme, Tin Komljenovic, Eric Stanton, Alex Spott, Emmett Perl, Minh Tran, Lin Chang, Tony Huang, Yichen Shen, Alan Liu, Justin Norman. A special thanks to Di Liang who had been a patient cleanroom mentor and was key in my first successful fab run. It is unfortunate that we did not continue to work together. Daryl and I have taught each other much in the optics lab during the EPHI program and this knowledge will be invaluable to me. Michael Davenport and Tin Komljenovic have helped me a lot in the last leg of my thesis work and I thank them for that. I would like to thank our group fabrication engineer Jon Peters. He has been a reliable source of help in all the projects I have been involved.

I would like to thank other graduate students or alumni/ alumnae in other research groups who have helped me on many occasions: Aaron Bluestone, Avantika Sodhi, Kim Nguyen, John Garcia, Erica Lively, Wenzao Li, Henrik Poulsen, Demis John, Michael Belt, Renan Moreira, Selim Dogru, John Parker, Rob Guzzon, Abi Sivananthan and Chinhan Lin.

I would like to thank the cleanroom staff Jack Whaley, Tom Reynolds, Tony Bosch, Don Freeborn, Mike Silva, Adam Abrahamsen, Aidan Hopkins, and Bill Mitchell for running a great cleanroom facility. I would like to thank the interns Alois Arrighi, Bassem Tossoin,

Ardit Velia and Silvia Chan for their help in screening devices and completing certain device characterization experiments.

I would also like to thank my former and present room-mates Scott Dirkse, John Smith Mac-Donald, Shawn Owens, Dinesh Ramaswamy, and Aseem Wadhwa for being of great help outside the academic environment.

Last, but not the least, I would like to thank my parents for their support and guidance throughout my life. They have been a part of all big decisions in my life including my decision to pursue higher education in the United States.

VITA OF SUDHARSANAN SRINIVASAN
June 2015

EDUCATION

Bachelor of Technology, Indian Institute of Technology, Madras, June 2009
Master of Science in Electrical and Computer Engineering, University of California, Santa Barbara, December 2010

AWARDS

Robert Weiderhold IEE Fellowship, 2009

PROFESSIONAL EMPLOYMENT

2009-15: Graduate Student Researcher, Department of Electrical and Computer Engineering, University of California, Santa Barbara

PUBLICATIONS


[1] **S. Srinivasan**, R. Moreira, D. Blumenthal, and J. E. Bowers, "Design of integrated hybrid silicon waveguide optical gyroscope," *Optics Express,* vol. 22, pp. 24988-24993.

[2] **S. Srinivasan** and J. E. Bowers, "Integrated High Sensitivity Hybrid Silicon Magnetometer," *Photonics Technology Letters, IEEE,* vol. 26, pp. 1321-1324.

[3] **S. Srinivasan**, M. Davenport, M. J. R. Heck, J. Hutchinson, E. Norberg, G. Fish, J. Bowers, "Low phase noise hybrid silicon mode-locked lasers," *Front. Optoelectron.,* vol. 7, pp. 265-276, 2014-09-09.

[4] **S. Srinivasan**, A. Arrighi, M. J. R. Heck, J. Hutchinson, E. Norberg, G. Fish, and J. E. Bowers, "Harmonically Mode-Locked Hybrid Silicon Laser With Intra-Cavity Filter to Suppress Supermode Noise," *Selected Topics in Quantum Electronics, IEEE Journal of,* vol. 20, pp. 8-15.

[5] **S. Srinivasan**, N. Julian, J. Peters, L. Di, and J. E. Bowers, "Reliability of Hybrid Silicon Distributed Feedback Lasers," *Selected Topics in Quantum Electronics, IEEE Journal of,* vol. 19, pp. 1501305-1501305.

[6] **S. Srinivasan**, Y. Tang, G. Read, N. Hossain, D. Liang, S. J. Sweeney, J. E. Bowers, "Hybrid Silicon Devices for Energy-Efficient Optical Transmitters." vol. 33, pp. 22-31.

[7] M. J. R. Heck, J. F. Bauters, M. L. Davenport, J. K. Doylend, S. Jain, G. Kurczveil, **S. Srinivasan**, T. Yongbo, and J. E. Bowers, "Hybrid Silicon Photonic Integrated Circuit Technology," *Selected Topics in Quantum Electronics, IEEE Journal of,* vol. 19, pp. 6100117-6100117.

[8] **S. Srinivasan**, A. W. Fang, D. Liang, J. Peters, B. Kaye, and J. E. Bowers, "Design of phase-shifted hybrid silicon distributed feedback lasers," *Optics Express,* vol. 19, pp. 9255-9261.

[9] C. Zhang, **S. Srinivasan**, Y. Tang, M. J. R. Heck, M. L. Davenport, and J. E. Bowers, "Low threshold and high speed short cavity distributed feedback hybrid silicon lasers," *Optics Express,* vol. 22, pp. 10202-10209.

[10] J. Bovington, **S. Srinivasan**, and J. E. Bowers, "Athermal laser design," *Optics Express,* vol. 22, pp. 19357-19364.

[11] D. Liang, M. Fiorentino, **S. Srinivasan**, J. E. Bowers, and R. G. Beausoleil, "Low Threshold Electrically-Pumped Hybrid Silicon Microring Lasers," *Selected Topics in Quantum Electronics, IEEE Journal of,* vol. 17, pp. 1528-1533.

[12] D. Liang, M. Fiorentino, **S. Srinivasan**, S. T. Todd, G. Kurczveil, J. E. Bowers, and a. R. G. Beausoleil, "Optimization of Hybrid Silicon Microring Lasers," *Photonics Journal, IEEE,* vol. 3, pp. 580-587.

[13] D. Liang, **S. Srinivasan**, D. A. Fattal, M. Fiorentino, H. Zhihong, D. T. Spencer, J. E. Bowers, and R. G. Beausoleil, "Teardrop Reflector-Assisted Unidirectional Hybrid Silicon Microring Lasers," *Photonics Technology Letters, IEEE,* vol. 24, pp. 1988-1990.

[14] D. Liang, **S. Srinivasan**, J. Peters, A. Fang, and J. E. Bowers, "Demonstration of Enhanced III-V-On-Silicon Hybrid Integration by Using a Strained Superlattice as a Defect Blocking Layer," *ECS Transactions,* vol. 33, pp. 421-426, October 1, 2010.

[15] **S. Srinivasan**, A. Arrighi, M. J. R. Heck, J. Hutchinson, E. Norberg, G. Fish, and J. E. Bowers, "Suppression of supermode noise in a harmonically mode-locked hybrid silicon laser using an intra-cavity filter," in *Optical Fiber Communication Conference*, San Francisco, California, p. Th3A.4.

[16] **S. Srinivasan**, D. T. Spencer, M. Heck, E. Norberg, G. Fish, L. Theogarajan, and J. E. Bowers, "Microwave generation using an integrated hybrid silicon mode-locked laser in a coupled optoelectronic oscillator configuration," in *CLEO: 2013*, San Jose, California, p. CTu2G.2.

[17] **S. Srinivasan** and J. E. Bowers, "Reliability of hybrid III-V on Si distributed feedback lasers," in *Semiconductor Laser Conference (ISLC), 2012 23rd IEEE International*, pp. 10-11.

[18] **S. Srinivasan**, L. Di, M. Fiorentino, R. G. Beausoleil, and J. E. Bowers, "Micro-ring resonator based electro-absorption modulators on the hybrid III-V on silicon platform," in *Optical Interconnects Conference, 2012 IEEE*, pp. 22-23.

[19] M. L. Davenport, **S. Srinivasan**, M. J. R. Heck, and J. E. Bowers, "A Hybrid Silicon/InP Integrated All-Passive Feedback Stabilized Mode-Locked Laser," in *Optical Fiber Communication Conference*, San Francisco, California, p. Th3A.5.

[20] D. Liang, **S. Srinivasan**, D. A. Fattal, M. Fiorentino, H. Zhihong, D. T. Spencer, J. E. Bowers, and R. G. Beausoleil, "Reflection-assisted unidirectional hybrid silicon microring lasers," in *Indium Phosphide and Related Materials (IPRM), 2012 International Conference on*, pp. 12-15.

ABSTRACT

Heterogeneous Integration for Reduced Phase Noise and Improved Reliability of Semiconductor Lasers

by

Sudharsanan Srinivasan

Significant savings in cost, power and space are possible in existing optical data transmission networks, sensors and metrology equipment through photonic integration. Photonic integration can be broadly classified into two categories, hybrid and monolithic integration. The former involves assembling multiple single functionality optical devices together into a single package including any optical coupling and/or electronic connections. On the other hand monolithic integration assembles many devices or optical functionalities on a single chip so that all the optical connections are on chip and require no external alignment. This provides a substantial improvement in reliability and simplifies testing. Monolithic integration has been demonstrated on both indium phosphide (InP) and silicon (Si) substrates. Integration on larger 300mm Si substrates can further bring down the cost and has been a major area of research in recent years. Furthermore, with increasing interest from industry, the hybrid silicon platform is emerging as a new technology for integrating various active and passive optical elements on a single chip. This is both in the interest of bringing down manufacturing cost through scaling along with continued improvement in performance and to produce multi-functional photonic integrated circuits (PIC).

The goal of this work is twofold. First, we show four laser demonstrations that use the hybrid silicon platform to lower phase noise due to spontaneous emission, based on the following two techniques, viz. confinement factor reduction and negative optical feedback. The first two demonstrations are of mode-locked lasers and the next two are of tunable lasers. Some of the key results include; (a) 14dB white frequency noise reduction of a 20GHz radio-frequency (RF) signal from a harmonically mode-locked long cavity laser with greater than 55dB supermode noise suppression, (b) 8dB white frequency noise reduction from a colliding pulse mode-locked laser by reducing the number of quantum wells and a further 6dB noise reduction using coherent photon seeding from long on-chip coupled cavity, (c) linewidth reduction of a tunable laser down to 160kHz using negative optical feedback from coupled ring resonator mirrors, and (d) linewidth reduction of a widely tunable laser down to 50kHz using on-chip coupled cavity feedback effect.

Second, we present the results of a reliability study conducted to investigate the influence of molecular wafer bonding between Si and InP on the lifetime of distributed feedback lasers, a common laser source used in optical communication. No degradation in lasing threshold or slope efficiency was observed after aging the lasers for 5000hrs at 70°C and 2500hrs at 85°C. However, among the three chosen bonding interface layer options, the devices with an interface superlattice layer showed a higher yield for lasers and lower dark current values in the on-chip monitor photodiodes after aging.

TABLE OF CONTENTS

1. Introduction ..... 1

A. Hybrid Silicon Platform ..... 3

B. Laser Phase Noise ..... 5

C. Yield and Reliability ..... 12

D. Summary ..... 13

2. Lowering Phase Noise of Mode-Locked Lasers ..... 14

A. Introduction ..... 14

B. Long Cavity Mode-Locked Lasers ..... 15

C. Coupled Cavity Mode-Locked Lasers ..... 24

1. Without On-Chip Feedback ..... 27

2. With On-Chip Feedback ..... 30

3. Discussion ..... 33

D. Summary ..... 35

3. Lowering Phase Noise of Tunable Lasers ..... 37

A. Coupled Cavity Tunable Laser ..... 37

1. Laser Design ..... 38

2. Theory ..... 39

3. Linewidth and Wavelength Tuning Measurements ..... 48

4. Summary and Future Work ..... 52

B. Coupled Ring Resonator Mirror Based Tunable Laser ..... 52

1. Laser Design and Fabrication ..... 53

2. Measurement Results ..... 55

3. Discussion ..... 57

4. Summary ..... 61

C. Conclusions ..... 61

4. Reliability of Hybrid Silicon DFB Lasers ..... 62

A. Introduction ..... 62

B. Experiment ..... 64

C. Results and Discussion ..... 67

D. Conclusion ..... 71

5. Hybrid Mode Locking ..... 72

6. Conclusions and Future Work ..... 79

B. Low Phase Noise Mode-Locked Lasers ..... 80

C. Low Phase Noise Tunable Lasers ..... 81

A. Reliability Study ..... 81

D. Future Work ..... 82

Appendix 1. Temperature Effects on Photoluminescence ..... 84

Appendix 2. Coupled Opto-Electronic Oscillator ..... 89

References ..... 93

LIST OF FIGURES

Figure 1.1. Thermal expansion coefficient values for InP and Si in the temperature range of 300°K to 800°K. Wafer bonding is done at ~573°K. .....3

Figure 1.2. (a)-(f) Schematic drawing of the wafer bonding steps involved in realizing hybrid silicon lasers. Each InP chip shown in (b) can have a different set of epitaxial layers optimized for a specific device like laser, modulator or detector. Figures are not to scale. .....5

Figure 1.3. Constellation diagram showing limitations on spectral efficiency because of phase noise. .....6

Figure 1.4. (a) Schematic cross-section of the gain region identifying the layers with the optical mode overlaid. (b) Carrier confined volume and (c) photon confined volume. Figure not to scale. .....8

Figure 1.5. An analogy explaining the linewidth reduction from reducing confinement factor. (a) Pipe of uniform width $W_1$ with an incompressible fluid that translates the changes in position of piton A faithfully to the changes in position of piston B. (b) Pipe of non-uniform width showing reduction in standard deviation of location of piston B due to Langevin force function. .....9

Figure 1.6. Diagram showing the conversion from laser frequency noise to mirror reflectivity fluctuations, using a filter element in the laser cavity with frequency dependent transmission. .....10

Figure 2.1. Plot of timing jitter requirement versus sampling rate for different bits of resolution of the ADC [12]. .....14

Figure 2.2. Schematics of the MLLD with an intra-cavity filter. Black lines indicate passive Si waveguides. SOA-Semiconductor optical amplifier, SA-saturable absorber [23] © 2014 IEEE .....16

Figure 2.3. Fiber coupled light vs. current curves for counterclockwise (CCW) lasing direction. CCW is with respect to schematic in Figure 2.2 [23] © 2014 IEEE. ..17

Figure 2.4. (a) RF power and (b) side-mode suppression ratio (SMSR) as a function of SOA current and SA voltage. Resolution bandwidth (RBW) - 3MHz [23] © 2014 IEEE. 18

Figure 2.5. Optical spectrum – (a) wide span and (b) close-up into the dashed box region in (a), electrical spectrum – (c) wide span and (d) close-in, for the MLLD with a 20GHz FSR intra-cavity filter. The RBW in (c) and (d) are 3MHz and 1kHz respectively. The SOA current is 220mA and the SA voltage is -0.5V [23] © 2014 IEEE.....19

Figure 2.6. Schematic of the gain, absorber and waveguide sections inside the laser cavity [12].....20

Figure 2.7. (a) Optical spectrum of the ring cavity laser showing 20GHz spaced optical lines (resolution bandwidth 20MHz) and (b) electrical spectrum showing the fundamental and its harmonic. Notice the spurs at 1.5 and 18.5GHz [12].....21

Figure 2.8. (a) Optical linewidth measurement and (b) single sideband phase noise of the 20GHz signal for the fundamental and harmonic MLLDs. The black lines in both plots are a guide to the eye with an ideal quadratic dependence with frequency [12]..22

Figure 2.9. Schematic showing the laser circuit. Black lines indicate the silicon waveguide, SOA-semiconductor optical amplifier, SA-saturable absorber. .....25

Figure 2.10. (a) Light-current curves for different absorber bias voltages for three (a) and five (b) QW device. .....27

Figure 2.11. (a) RF spectrum (resolution bandwidth-RBW 3MHz) for the three (a) and five (b) QW device. Bias points (a) 75mA-SOA current, -0.4V-SA voltage and (b) 67mA-SOA current, -0.8V-SA voltage. ..... 28

Figure 2.12. Optical spectrum (RBW-0.02nm) for the three (a) and five (b) QW device. Bias points are the same as in Figure 2.11. ..... 28

Figure 2.13. Autocorrelation traces (blue) for the three (a) and five (b) QW device. Bias points are the same as in Figure 2.11. The red lines are the sech-squared fit to data. 29

Figure 2.14. Phase noise comparison of the 17.4GHz signal for the three and five QW devices. Bias conditions are the same as in Figure 2.11. ..... 30

Figure 2.15. (a) 3dB, (b) 10dB linewidth and (c) oscillation frequency of the microwave signal as a function of feedback SOA current and thermal tuner current. The optimum bias condition is at 2.5mA SOA current and 7mA tuner current. Data measured from three QW device. ..... 31

Figure 2.16. (a) 3dB, (b) 10dB linewidth and (c) oscillation frequency of the microwave signal as a function of feedback SOA current and thermal tuner current. The optimum bias condition is at 0.25mA SOA current and 2mA tuner current. Data measured from five QW device. ..... 31

Figure 2.17. RF spectrum showing the best linewidth achieved with feedback for the three (a) and five (b) QW device centered at 17.362GHz and 17.367GHz respectively. RBW-10kHz. ..... 32

Figure 3.1. A schematic view of the tunable laser, with an integrated external cavity. Tuners are yellow (two phase sections and two rings for wide tuning), and SOAs are orange (one is the laser active section, and one is used as an ON/OFF switch or to control the

level of feedback). The monitor photodiode (MPD) is used to measure the laser output power for adjustment of laser parameters. .....38

Figure 3.2. Schematic of the laser used for modeling. SWF - single wavelength filter. Orange rectangle - gain section. .....40

Figure 3.3. The mode locations in the main cavity and the feedback cavity, showing non-uniform mode spacing. Only a few modes are shown for simplicity.....40

Figure 3.4. Normalized reflection (a), phase (b) and linewidth reduction factor (c) of the laser without external cavity as a function of frequency offset from resonance ($\alpha_H$=4). (d) Measured linewidth (red diamonds) as a function of laser phase tuner power. The blue line is a guide to the eye. .....43

Figure 3.5. (a) Normalized reflection, (b) phase and (c) linewidth reduction factor of the laser with external cavity as a function of frequency offset from resonance ($\alpha_H$ = 4). (d) RIN measurement when external SOA is under high bias current (Resolution bandwidth (RBW) – 3MHz). Inset: Close-up RIN over a narrow frequency range showing alternating broad and narrow peaks. RBW – 500kHz. .....44

Figure 3.6. (a) Theoretical and (b) measured curves for normalized modulation response of the laser with and without external cavity stabilization. The laser quiescent current was 70mA. The peaks around 8GHz in measured spectra are due to photon-photon resonance [37] that is not included in our simplified theoretical model.....46

Figure 3.7. (a) Theoretical and (b) Measured RIN spectrum with and without external cavity stabilization. RBW – 1MHz. .....47

Figure 3.8. Overlaid optical spectra from 27 different set points showing >54nm tuning range with SMSR > 45dB (RBW - 0.02 nm).....48

Figure 3.9. (a) Best measured linewidth across the full tuning range. (b) Measured spectrum for the 50kHz result (RBW - 30kHz). (c) Bias currents (blue diamonds) applied to external SOA for linewidths measured and shown in (a) and a trend line (black).50

Figure 3.10. (a) Microscope image of the hybrid silicon laser. (b) Schematic of the laser showing the design using CRR mirrors. Wavelength tuning is achieved by thermally tuning the waveguides (black lines) underneath the tuners (yellow lines). The orange section is the SOA for gain. P-laser anode, N-laser cathode, H1, H2, H3-positive terminal for each heater pads. The negative terminal of all heaters is shorted to laser cathode. .....53

Figure 3.11. (a) CRR mirror schematic. Reflection spectrum of each CRR mirror (a) and the composite mirror loss spectrum (b) of the laser cavity. Inset: Net modal gain ($\Gamma g-\langle\alpha_i\rangle$) of a 1mm long SOA, where $\Gamma$ is the confinement factor, g is the material gain and $\langle\alpha_i\rangle$ is the internal loss per unit length. .....55

Figure 3.12. L-I-V curve for the tunable laser diode at 20°C. .....56

Figure 3.13. Coarse tuning of the laser between 1553nm and 1582nm.....56

Figure 3.14. Self heterodyne linewidth measurement (black dots) and the corresponding Lorentzian fit (green line). The resolution bandwidth is 10kHz.....57

Figure 3.15. Simulation results for (a) effective cavity length as a function of wavelength showing almost tripling of length at resonance and (b) location of each longitudinal mode and the spacing from its nearest neighbor, reduced by one-third at resonance. 58

Figure 3.16. Simulated values for parameters A, B, F around resonance wavelength (1577.58nm) showing large reduction in linewidth ($\propto 1/F^2$) on the long wavelength side of the resonance.....59

Figure 3.17. Thermal image of the heater when supplied with 30mW(4V), showing non-uniform heating at the hairpin bend in the center due to crosstalk. .....60

Figure 4.1. (a), (b) Schematic diagram and TEM image of the longitudinal cross-section of a symmetric quarter-wave shifted hybrid Si DFB laser [62] © 2013 IEEE. .....63

Figure 4.2. (a) Threshold current of DFB lasers with three different epitaxial layer structures before aging tests, (b)-(d) The simulated conduction band (red) and valence band (blue) diagram for the three structures, (e) Representative Light-Current (L-I) curves for 50 DFB laser diodes of structure A before aging [62] © 2013 IEEE. .....66

Figure 4.3. Scanning electron microscope (SEM) image of a complete carrier used in the aging test [62] © 2013 IEEE.....67

Figure 4.4. (a)-(f) Threshold current of devices at various aging conditions - Structure A (blue), Structure B (red) and Structure C (green). (g)-(h) Degradation data for two structures along with the sub-linear fit (black) [62] © 2013 IEEE.....69

Figure 4.5. Dark current (-4V) of photodetectors fabricated on structures A (blue), B(red) and C(green), (a) before aging test and (b) after aging test [62] © 2013 IEEE. ..70

Figure 4.6. (a) Close-up TEM image of a failed device made using an epitaxial wafer with structure A showing no defects in the active layer. (b) A stitched image of a 15μm long longitudinal cross-section of the same laser diode with no defects in the active layer [62] © 2013 IEEE. .....71

Figure 5.1. (a-e) RF power as a function of SOA current and SA voltage at the first five harmonics; fundamental (1.99GHz), 2$^{nd}$ (3.98GHz), 3$^{rd}$ (5.97GHz), 4$^{th}$ (7.96GHz) and 5$^{th}$ (9.95GHz) respectively. (f) Weighted sum of RF powers at the first five harmonics. Resolution bandwidth (RBW) - 3MHz [23] © 2014 IEEE. .....73

Figure 5.2. Optical spectrum (a), autocorrelator trace (b), electrical spectrum – wide span (c) and close-in (d). The RBW in (c) and (d) are 3MHz and 1kHz respectively. The SOA current is 140mA and the SA voltage is -1.3V [23] © 2014 IEEE. ..... 74

Figure 5.3. Electrical spectrum (RBW – 3MHz) (a), optical spectrum (b), sampling oscilloscope trace (c) autocorrelator trace (d) for active locking at 2GHz. The bias conditions are same as in Figure 5.2. The RF power at the signal generator is 0dBm [23] © 2014 IEEE. ..... 75

Figure 5.4. Electrical spectrum (RBW – 3MHz) (a), optical spectrum (b), sampling oscilloscope trace (c) autocorrelator trace (d) for harmonic locking at 7.96GHz. The bias conditions are same as in Figure 5.2. The RF power at the signal generator is 0dBm [23] © 2014 IEEE. ..... 76

Figure 5.5. Electrical spectrum (RBW – 3MHz) (a), optical spectrum (b), for harmonic locking at 20GHz. The SOA current is 206mA and the SA voltage is -1.4V. The RF power at the signal generator is 10dBm [23] © 2014 IEEE. ..... 77

## 1. Introduction

The ubiquity of computing and communication devices and the need to provide easy exchange of information between them has fueled the growth of large scale communication networks over the past few decades. The exponential growth in data traffic in these networks has demanded constant innovation both at the architectural and at the device level. A significant amount of this information exchange is still done electrically and is becoming more and more difficult due to limited processor pin counts and limits from power dissipation per unit area. The advantages of optical communication such as low propagation loss, large available bandwidth and no electro-magnetic interference (EMI) with third party channels are the reasons for wide-spread growth of the internet to all parts of the globe. Three significant revolutionary innovations were required for this to happen, viz. the low propagation loss optical fiber, room temperature operational continuous wave (CW) laser diode and the erbium doped fiber amplifier (EDFA). The cost of the optical components for an optics enabled inter- and intra-continental communication system was justifiable as they were cheaper and more power efficient than other alternatives. From a physics point of view, using optics for communication is certainly the best choice for its advantages stated above. However, bringing optics closer, for board-to-board, chip-to-chip and intra-chip communication in present day server networks has been met with challenges of component cost which include material cost, manufacturing cost, testing, installation and maintenance cost. We are at the brink of another revolution to come that will meet these cost metrics and influence the way networking is done in the future. The transition from bulk optical components to sophisticated integrated electronic and photonic circuits will be seen as analogous to the adoption of transistor technology over vacuum tubes.

The prevailing vision for future optics based networking has been to closely integrate various optical components meant for information exchange, in intimate contact with electronic circuits meant for processing information. The dominant electronics technology, known as the complementary metal-oxide-semiconductor (CMOS) process is based on large, 300mm or more, silicon substrates. However, silicon being an indirect bandgap material is a very inefficient light emitter and hence we require other direct bandgap materials to generate, amplify and detect light. Indium phosphide (InP) and gallium arsenide (GaAs) are the chief substrate materials used to make lasers, modulators and detectors for optical communication and are often the standard against which device performances on other material platforms are compared. Photonic integration of more than one device was first attempted on these two native substrates and is still pursued, to demonstrate the advantages of large scale photonic integration from reduced size, weight and power consumption. However, the manufacturing cost does not scale down proportionally due to limited substrate sizes, 150mm or less, and hence prohibitive for large scale production. A more recent advancement in this area was to show the feasibility of bonding direct bandgap materials to silicon or silicon-on-insulator substrates at a wafer scale. This was further developed to fabricate various electrically controlled active optical devices including lasers, amplifiers, modulators and detectors on silicon, comparable in performance to devices fabricated on native substrates. The devices were self aligned to the silicon waveguides on chip which can be used to carry light to other locations. This technology reduces the cost significantly spent on optics alignment during the packaging process. Silicon is also transparent for wavelengths between 1.2μm and 10μm and is well suited for guiding light relevant for telecom, which is in the wavelength region around 1.55μm because the optical attenuation of glass fibers is the lowest. The large refractive index contrast between silicon (3.47) and air

(1) or oxide of silicon (1.44) allows for compact waveguide circuits. A wide variety of passive silicon waveguide circuits like wavelength multiplexers/ demultiplexers, filters, couplers have been demonstrated and are now available commercially. Therefore, silicon is quickly becoming the material of choice for manufacturing photonic components and together with wafer bonding of III-V material to silicon for increased functionality, is expected to overcome the communications bottleneck in computing and telecommunications equipment. Furthermore, this approach is practical considering the material and process compatibility between silicon photonics and the dominant CMOS electronics technology.

### *A. Hybrid Silicon Platform*

The thermal expansion coefficient mismatch between epitaxial layers grown on InP substrates and silicon make the wafer bonding a critical step in the integration process. Figure 1.1 shows the thermal expansion coefficient of InP [1] and Si [2] as a function of temperature.

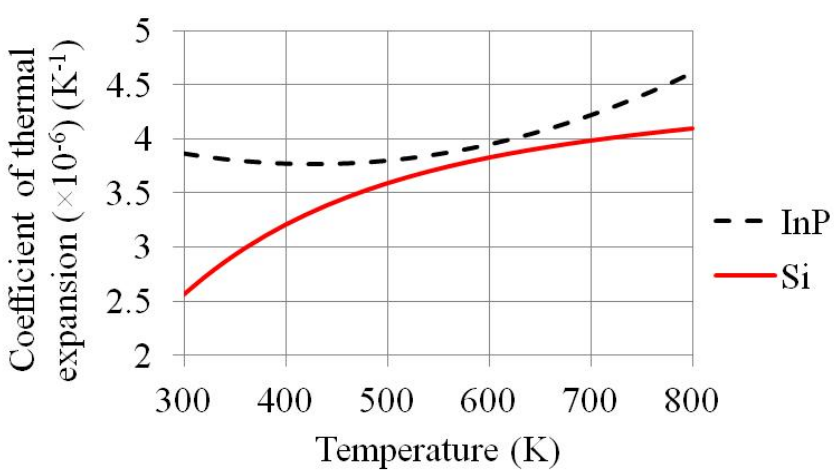


**Figure 1.1. Thermal expansion coefficient values for InP and Si in the temperature range of 300°K to 800°K. Wafer bonding is done at ~573°K.**

A few common techniques for wafer bonding these two material systems found in literature include hydrophilic direct wafer bonding [3], oxygen plasma assisted wafer

bonding [4], oxide mediated wafer bonding [5] and benzocyclobutene (BCB) based adhesive bonding [6]. The devices in this thesis were fabricated using the oxygen plasma assisted wafer bonding technique. This technique creates a very thin layer of oxide on the two wafer surfaces and generates additional dangling bonds for a strong covalent bond formation at low anneal temperatures in the range of 250°C - 300°C. The oxide layer created between the two surfaces after bonding is in the range of 5nm to 20nm. This thickness is an important parameter as the closer the epitaxial layers are to the silicon layer, greater is the influence on the optical mode shape due to changes in silicon waveguide dimension. Therefore, the confinement factor in the quantum well (QW) active region and the effective index of the optical mode can be controlled using the silicon waveguide width underneath. Figure 1.2 is a schematic that show the major steps in the wafer bonding process to realize lasers on silicon.

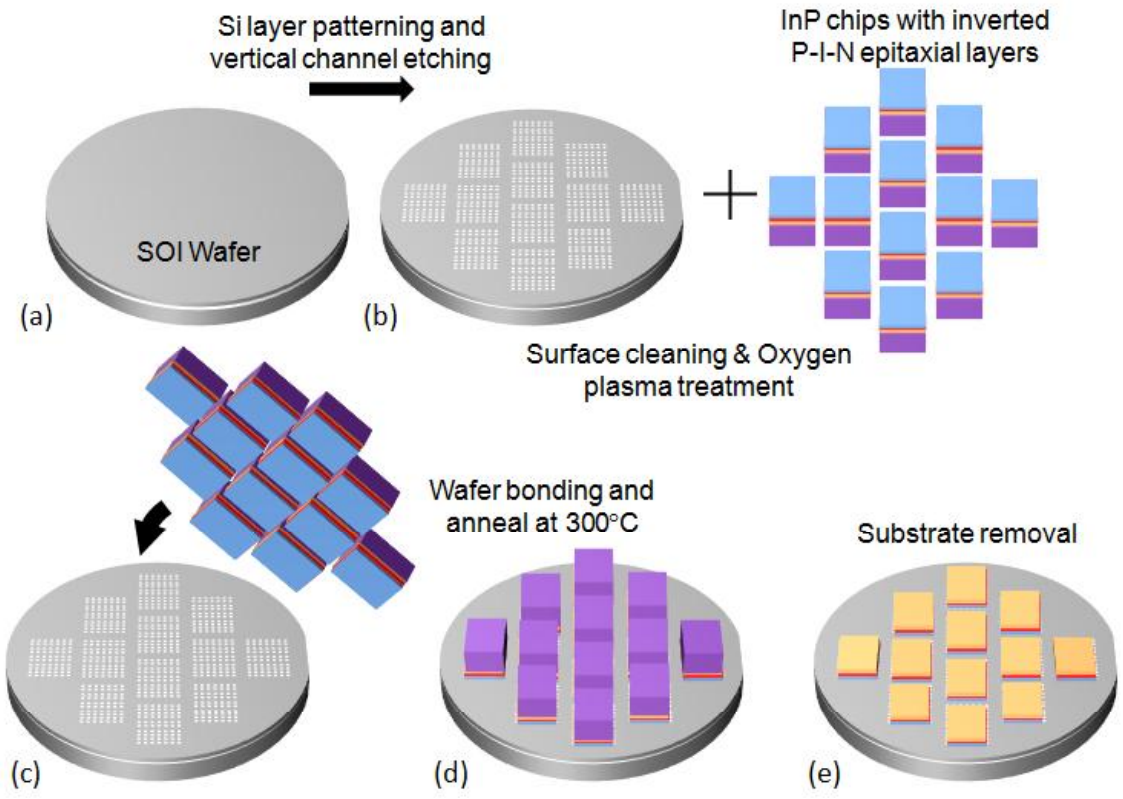

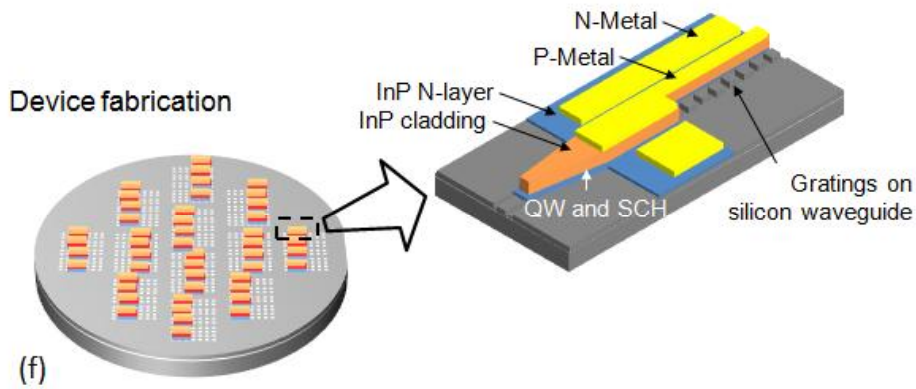


**Figure 1.2. (a)-(f) Schematic drawing of the wafer bonding steps involved in realizing hybrid silicon lasers. Each InP chip shown in (b) can have a different set of epitaxial layers optimized for a specific device like laser, modulator or detector. Figures are not to scale.**

This approach is heterogeneous integration, but we use the historical term [7] hybrid silicon laser.

### *B. Laser Phase Noise*

An important characteristic of a laser is its linewidth. For instance, spectral efficiency in coherent optical communication can be improved by lowering phase noise of the laser source or in other words if the communication channel is well characterized, the limit to spectral efficiency is determined by the phase noise of the laser. Figure 1.3 shows a constellation diagram with eight points which requires that the net phase excursion needs to be less than $\pi/4$.

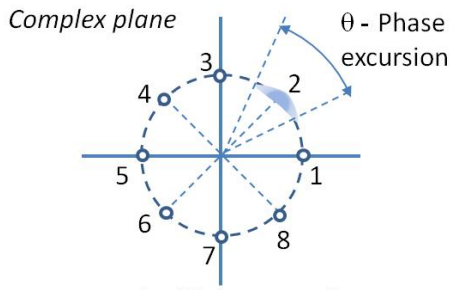


$$\text{Spectral efficiency} \propto \log_2 M$$

$$M = \left\lfloor \frac{2\pi}{\theta} \right\rfloor$$

**Figure 1.3. Constellation diagram showing limitations on spectral efficiency because of phase noise.**

The dominant source of this phase (or frequency) noise is amplified spontaneous emission (ASE). The spontaneous emission events in the active region contribute in two ways to the linewidth. One is a direct contribution from spontaneous emitted photon field adding in quadrature to the steady state laser cavity photon field. The other is an indirect contribution from the spontaneously emitted photon causing a change in photon density in the cavity which through the course of relaxation oscillations stabilizes itself and the resulting fluctuation in laser frequency is from the fluctuating carrier density during the stabilization process. These two contributions are added together to derive the Schawlow-Townes-Henry linewidth ($\Delta\upsilon_{STH}$) expression for a semiconductor laser, shown in Eqn. 1.1 [8, 9].

$$\Delta\upsilon_{STH} = \frac{\Gamma R'_{sp}}{4\pi N_p}\left(1+\alpha^2\right) \tag{1.1}$$

where $\Gamma$ is the confinement factor defined as the ratio of the active region volume (V) to the volume occupied by photons ($V_p$), $R'_{sp}$ is the spontaneous emission rate that couples into the lasing mode, $N_p$ is the photon density in the laser cavity and $\alpha$ is the linewidth enhancement factor.

In a Fabry-Perot laser where there is no accumulation of photons in any segment of the cavity, unlike in a quarter wave shifted distributed feedback laser, the linewidth goes inversely proportional to the length of the laser diode due to decreasing mirror loss rate. A more intuitive way of thinking is to observe that the number of longitudinal modes is increasing with increasing length, which means the probability of an emitted spontaneous photon to interact with the lasing mode is inversely proportional to the number of longitudinal modes. This is also equivalent to saying that reducing $R'_{sp}$ reduces linewidth. The linewidth is also inversely proportional to the optical output power of the laser which is directly related to the intracavity photon density ($N_p$). Finally, reducing the confinement factor $\Gamma$ also reduces the linewidth. This is understood by observing that the volume occupied the photons in a laser cavity is not the same volume occupied by the carriers that provide gain. Since all the spontaneous emission events are confined in the QW active region the perturbation to the photon field is weakened by this factor. The confinement factor is a very important parameter in the discussion of semiconductor laser linewidth and hence we will go into further detail to introduce the techniques used in this thesis work to reduce the linewidth. We will also look into how the hybrid silicon platform can be used effectively to reduce the confinement factor.

Figure 1.4 (a) shows the cross-section of a typical hybrid silicon laser gain medium. Figure 1.4 (b) and (c) show the carrier confined volume and photon confined volume respectively. The confinement factor can be further approximated using the individual laser dimensions as follows:

$$\Gamma = \frac{V}{V_p} = \Gamma_x \Gamma_y \Gamma_z = \left(\frac{W}{L_x}\right)\left(\frac{Nt}{L_y}\right)\left(\frac{L}{L_z}\right) \tag{1.2}$$

where x, y and z denote the lateral, transverse and longitudinal directions. W, t and L are the dimensions of the quantum well layer in each direction, and $L_x$, $L_y$ and $L_z$ form the dimensions of a cuboid of equivalent volume as the photon confined volume. N is the number of quantum wells used.

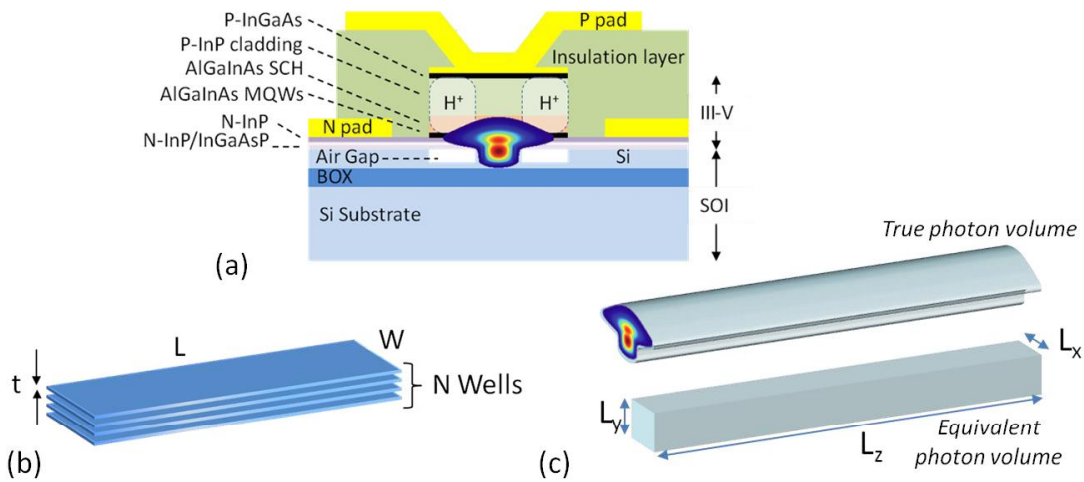


**Figure 1.4. (a) Schematic cross-section of the gain region identifying the layers with the optical mode overlaid. (b) Carrier confined volume and (c) photon confined volume. Figure not to scale.**

To understand the reduction in linewidth from reducing confinement factor we will look at an analogy that simplifies the understanding of this effect. It also does not require very detailed calculations and helps get to the physics quickly. Let us consider a pipe of uniform width $W_1$, as in Figure 1.5 (a), filled with an incompressible fluid and contained within two pistons A and B. We apply a Langevin forcing function $F_x$ on piston A that perturbs its location. The distribution of the location of piston A is a Gaussian with standard deviation $\sigma_x|_A$. The Langevin force mimics the spontaneous emission event. Since the fluid is incompressible, piston B follows the motion of piston A and the standard deviation of the location of piston B ($\sigma_x|_B$) is the same as that of piston A. If the output linewidth of the laser

is seen analogous to $\sigma_x|_B$, Figure 1.5 (a) describes a situation where the confinement factor is unity. Now if we increase the width of the pipe only around piston B, as shown in Figure 1.5 (b), by a width $W_2$ the influence of the force $F_x$ can be minimized. The compressed fluid volume when piston A moves to the right by $\Delta x_A$ is given by $W_1\ \Delta x_A$ and the amount piston B has to move to the right to accommodate the compressed volume is given by $\Delta x_B = W_1\ \Delta x_A / (W_1 + W_2)$. Thus the value of $\sigma_x|_B$ is reduced by a factor $1 / (1 + (W_2 / W_1))$. This situation describes the case when the confinement factor is less than unity. This technique of noise reduction can be described as noise dilution. In the case of a laser diode with three dimensional photon confinement the linewidth can be reduced by reducing any or all the three individual confinement factors $\Gamma_x$, $\Gamma_y$, $\Gamma_z$. We demonstrate linewidth reduction in four different lasers by reducing $\Gamma_y$ and $\Gamma_z$ throughout the course of Chapters 2 and 3.

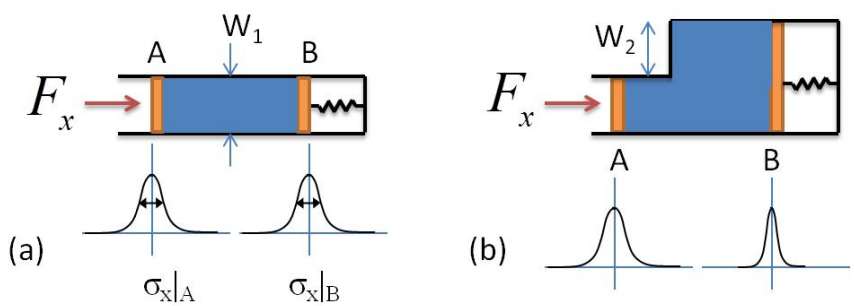


**Figure 1.5. An analogy explaining the linewidth reduction from reducing confinement factor. (a) Pipe of uniform width $W_1$ with an incompressible fluid that translates the changes in position of piton A faithfully to the changes in position of piston B. (b) Pipe of non-uniform width showing reduction in standard deviation of location of piston B due to Langevin force function.**

The above technique helps reduce the linewidth by manipulating the laser cavity. There is yet another passive optical technique to reduce laser frequency noise. This involves the mirrors of the laser. The rate equations for a laser involving the carrier density and photon density show a negative correlation between the two quantities. That is to say that the only source of photons in the cavity comes from carrier recombination events and an increase in the steady state population of either comes from a reduction of the other. This can be used to

our advantage to form a negative feedback loop by just using the elements that define the laser. Figure 1.6 shows a situation when the mirror reflectivity is a function of frequency. This can be achieved by including resonant structures in the laser cavity that act as filters. The slope of the changing mirror reflectivity is important and works only if the derivative of mirror reflectivity with respect to frequency is positive.

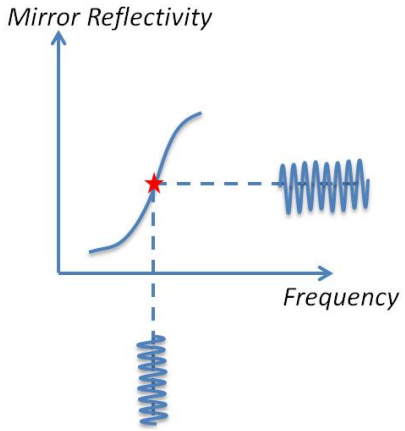


**Figure 1.6. Diagram showing the conversion from laser frequency noise to mirror reflectivity fluctuations, using a filter element in the laser cavity with frequency dependent transmission.**

When the laser is biased in such a way that it operates at the frequency marked by the red star in Figure 1.6 fluctuations in lasing frequency, changes the mirror reflectivity. For frequencies less than the inverse cavity photon lifetime we can assume that the laser achieves steady state between its carrier and photon population. Now, when the laser frequency increases by a small amount the mirror loss goes down and the steady state photon population rises which depletes the carrier density and the gain. This in turn increases the refractive index through the linewidth enhancement factor which reduces the laser frequency thus forming a negative feedback loop. This technique can be very useful in realizing large reductions in frequency noise due to spontaneous emission.

The versatility of the hybrid silicon platform lies in realizing cavity structures that can maximally utilize these frequency noise reduction techniques. The light after receiving gain

along the hybrid section can couple down to the silicon waveguide layer completely where we can tailor the photon lifetime and/ or include resonant filters to fully control the laser cavity properties. These various cavity designs can be optimized to a large extent independent of the gain medium and hence provides an opportunity to abstract the laser optimization methodology into two levels, one being at a fundamental material optimization level which include: choice of whether the active medium is either quantum wells or quantum dots, the strain in the material, the conduction and valence band offsets, the layer thicknesses, the background doping, separate confinement heterostructure (SCH) layer design and the design of other n- and p-contact layers. The other level involves optimizing the photonic circuit which includes the taper transition section, characterization of passive silicon photonic components like couplers, filters, themal tuners etc. This abstraction also helps to explore if the so called "material" limit can be surpassed through effective circuit design.

It is important to highlight that the two techniques described above to reduce frequency noise are all optical techniques which do not require any other master laser source. The advantage being all the necessary optical elements can be integrated onto a single chip using the hybrid silicon platform. Injection locking using a narrow linewidth master laser source and several other techniques that involve electronic or opto-electronic feedback, where the feedback signal is part way electrical and part way optical, have demonstrated linewidth reduction and is beyond the scope of this thesis.

### *C. Yield and Reliability*

Yield and reliability are very important topics that finally decide if a technology is manufacturing ready. The advantage of a large substrate size is no longer relevant if the yield or reliability is poor. When it comes to estimating yield for a photonic integrated circuit (PIC) which include many optical elements it is necessary that all the elements function properly. Even if one device fails the functionality of the PIC may be compromised. Hence, it is important to maintain near 100% efficiency at every step in the manufacturing process and this includes achieving successful bonding over the entire die area. Although, the wafer bonding technique provides a very strong bond between the two materials the yield depends on the number of particulate impurities trapped between the bonded interfaces. The yield can be >95% if the surfaces are kept clean throughout the bonding process [10]. However, after the bond is complete the wafer is subject to certain constraints in temperature for the fabrication steps that follow. Appendix 1 contains the results of a study where the photoluminescence (PL) intensity is monitored on a control sample throughout the device fabrication steps which include the high temperature plasma enhanced chemical vapor deposition (PECVD) of silicon oxide and the contact metal anneal. No reduction in PL intensity is observed which confirms the integrity of the QW active region after the processing is complete. The sample was then taken to higher temperatures and the PL intensity dropped to ~35% of its original value at 420°C. The sample also showed some bubbling on the surface when heated to 440°C. Chapter 4 discusses in detail the reliability experiment conducted on hybrid silicon DFB Lasers and also provides some yield numbers for that process run.

### *D. Summary*

This chapter starts with the motivation for photonic integration on silicon to implement information exchange at all distance scales using optics. We introduce certain salient features of the hybrid silicon platform that shows potential in realizing this vision. Monolithically integrated lasers play a key role in achieving complete integration of an optical system on chip and works to the strength of any technology that makes it possible. As alluded to earlier, yield and reliability of hybrid silicon devices can be of significant importance for the wide spread use of this technology. We illustrate two all optical techniques to reduce semiconductor laser linewidth and introduce a laser cavity design approach to implement them on an integrated platform.

Chapters 2 and 3 show results from mode-locked lasers and tunable lasers respectively. These lasers are fully integrated on-chip and exhibit very low phase noise. We quantify this reduction and compare certain results to theoretical predictions. Chapter 4 will discuss the reliability results conducted on hybrid silicon DFB lasers. Chapter 5 shows results from hybrid mode-locking long cavity lasers and serves as an annex to Chapter 2 in highlighting the importance of photonic filtering in harmonically mode-locked cavities. In Chapter 6 we provide our concluding statements and shed some light on possible future work in this area. This thesis also includes some appendices with information that could be beneficial to future researchers in this area.

## 2. Lowering Phase Noise of Mode-Locked Lasers

### *A. Introduction*

Mode-locked laser diodes (MLLDs) are gaining interest as compact microwave signal sources for high bit rate communication systems, optically sampled analog to digital converters (ADCs), frequency metrology, and arbitrary waveform generation. In the case of ADCs, the aperture jitter present in complementary metal-oxide-semiconductor (CMOS) and SiGe electronic technology, which is around 1ps [11], is a major limiting factor in reaching higher sampling rate and resolution. Figure 2.1 shows the requirement for timing jitter of the source versus sampling frequency for different number of resolving bits. This dictates that for an 8 bit resolved ADC, the timing jitter should be 100fs or less for sampling frequencies in the X/Ku band.

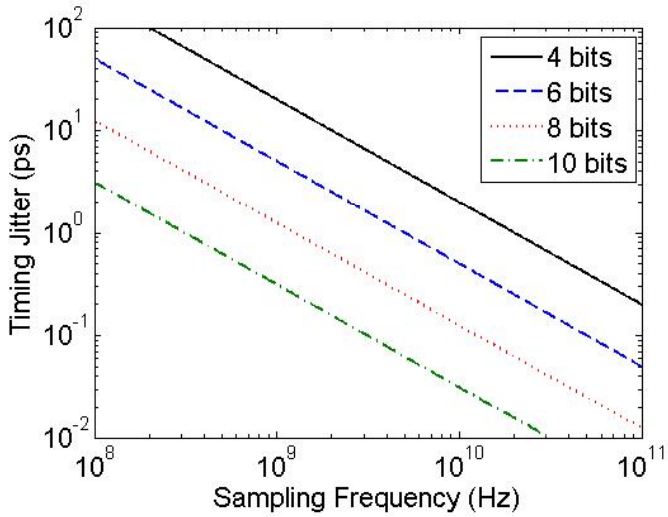


**Figure 2.1. Plot of timing jitter requirement versus sampling rate for different bits of resolution of the ADC [12].**

The short cavities of MLLDs enable very high repetition rates, such as ~100 GHz demonstrated in Reference [13]. They are also robust and have long lifetimes. This is particularly an important feature for low-noise lasers as they require minimum start-up and

monitoring. Monolithic semiconductor lasers usually consume much less power than their bulk counterparts with assembled components. Semiconductor manufacturing techniques allow for large scale production of these lasers with tightly controlled performance variations.

Despite all the beneficial factors listed above, there have been only a few demonstrations where high frequency operation and low timing jitter have been simultaneously achieved [14-17]. Moreover, these demonstrations often involve external cavity arrangements that are not readily scalable in terms of large scale manufacturing. To drive down cost, we need to integrate the external cavity elements on-chip and we demonstrate this integration using the hybrid silicon platform.

This chapter has been divided into two sections. Section B includes results from mode-locked lasers at 1550nm wavelength and demonstrates the benefit of long cavity lasers to reduce phase noise. In other words we lower phase noise by lowering the longitudinal confinement factor. Section C shows results from mode-locked lasers at 1310nm wavelength and discusses the impact on phase noise from lowering both transverse and longitudinal confinement factor. Transverse confinement is reduced by reducing the number of quantum wells and the longitudinal confinement is reduced using a long on-chip coupled cavity. Section D concludes with a summary of all the findings.

### *B. Long Cavity Mode-Locked Lasers*

In a mode-locked laser with a fixed length of gain section and a relatively long passive section, the optical phase noise due to spontaneous emission goes down as the square of the passive section length if the internal losses are held constant. The phase noise of the generated radio-frequency (RF) signal is dominated by spontaneous emission noise and a

valid design strategy for achieving narrow RF linewidth is harmonic mode-locking of long cavity lasers [18]. However, the supermode noise from the competing longitudinal modes of the laser, when harmonically mode-locked at a multiple of the fundamental repetition rate, needs to be suppressed to reduce the integrated timing jitter. Therefore we design an on-chip hybrid silicon mode-locked laser with a passive section length of ~4cm and incorporate an intra-cavity ring resonator filter to simultaneously achieve narrow RF linewidth and low supermode noise.

Some of the design advantages of this technology, over fabricating these lasers on indium phosphide (InP), are as follows. First, the high index contrast silicon waveguides have lower losses and smaller bend radii, which make long, compact on-chip cavities possible [19-21]. Second, two-photon absorption is around two orders of magnitude lower in silicon [22]. This allows for higher power densities and consequently higher pulse peak powers in the waveguide. Lastly, the width of the silicon waveguide underneath the III/V region controls the confinement of the optical mode with the quantum wells. Therefore, the waveguide design can be optimized for making high-saturation power amplifiers with reduced non-linear gain compression while maintaining adequate absorber saturation.

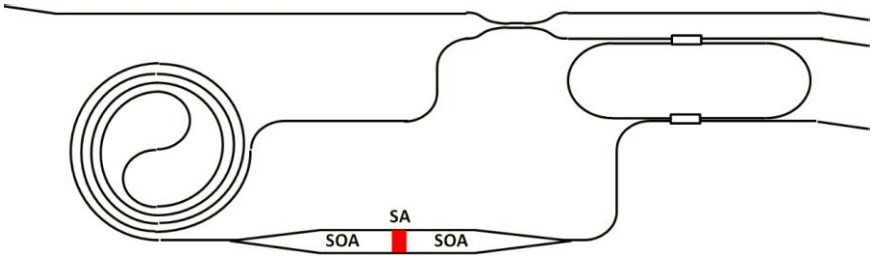


**Figure 2.2. Schematics of the MLLD with an intra-cavity filter. Black lines indicate passive Si waveguides. SOA-Semiconductor optical amplifier, SA-saturable absorber [23] © 2014 IEEE .**

Figure 2.2 shows a schematic of the fabricated ring laser with 3.967cm cavity length (~2GHz repetition rate), and includes a 20GHz free spectral range (FSR) ring resonator filter inside the laser cavity. We use two 50:50 multi-mode interference (MMI) couplers

(estimated excess loss <0.5dB per MMI) to couple in and out of the filter with low insertion loss. Realizing these structures on low-propagation loss silicon waveguides of 1dB/cm is the key to reducing the impact on operating power from excess loss, and achieving high quality factor filters for better side-mode suppression. Light from the ring laser is coupled out to a bus waveguide using directional couplers with a 10:90 splitting ratio. The laser has two 700 μm long symmetric gain sections separated by a small reverse biased section that acts as a saturable absorber (SA), for stable mode locking operation [24]. The electrical isolation is achieved by ion implantation. In the hybrid section, the confinement in the III-V active layers was designed to be 6% with a constant Si rib waveguide width of 1.5μm. The absorber length was 50μm. The output waveguide terminates at an anti-reflection coated facet at an angle of 7° for minimizing reflections back into the laser cavity. The size of each laser is $7 \times 1.5\text{mm}^2$.

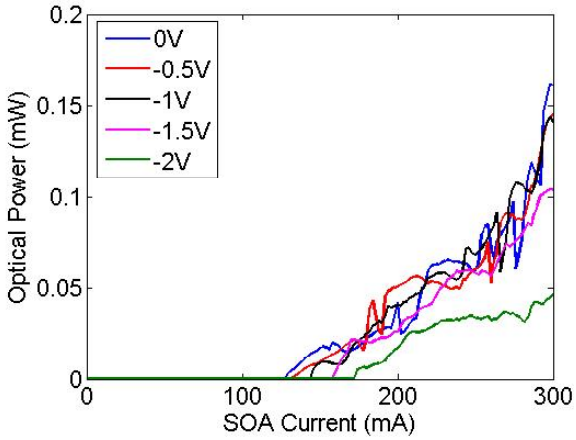


**Figure 2.3. Fiber coupled light vs. current curves for counterclockwise (CCW) lasing direction. CCW is with respect to schematic in Figure 2.2 [23] © 2014 IEEE.**

The chip is placed on a temperature controlled copper plate held at 20°C. Light is coupled out of the chip using a 2μm spot size lensed fiber. The estimated coupling loss is 6dB. The RF port of the bias-T connected to the absorber was terminated at 50Ω. The continuous wave light-current (L-I) curves at 20°C for different absorber voltages are shown

in Figure 2.3. The features on the L-I curves are from switching in lasing direction and possibly from multiple lateral modes. The change in threshold current as a function of decreasing SA bias voltage is in accordance with increasing cavity losses from reverse biasing. Another important aspect that influences the shape of the L-I curve is the mismatch between an integer multiple of the laser cavity repetition rate and the FSR of the ring resonator. As the SOA injection current is increased the laser cavity length changes slightly and moves the lasing modes into or out of resonance with the ring resonator thereby increasing or decreasing the output power respectively. The data is shown for the counter clockwise (CCW) lasing direction, which had higher output power.

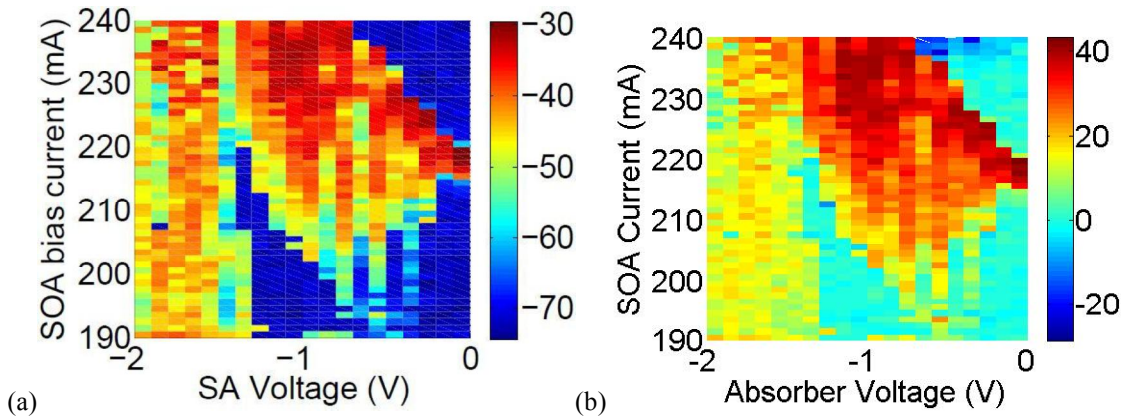


**Figure 2.4. (a) RF power and (b) side-mode suppression ratio (SMSR) as a function of SOA current and SA voltage. Resolution bandwidth (RBW) - 3MHz [23] © 2014 IEEE.**

Figure 2.4 (a) shows the RF power at the 20GHz tone as a function of SOA current and absorber voltage. The electrical spur mode suppression across the entire spectrum of the ESA is shown in Figure 2.4 (b). The maximum spur mode suppression shown in this plot is limited by the noise floor of the ESA. We note that for voltages less than -1.5V, although the RF power is high for certain bias conditions, the spur mode suppression is poor. The spurs were either at 2GHz or 2GHz away on either side of the 20GHz peak. From Figure 2.4, the regions around (-1V, 230mA) and (-0.5V, 220mA) simultaneously show high RF power and

large spur mode suppression. Further investigations were carrier around these operating points.

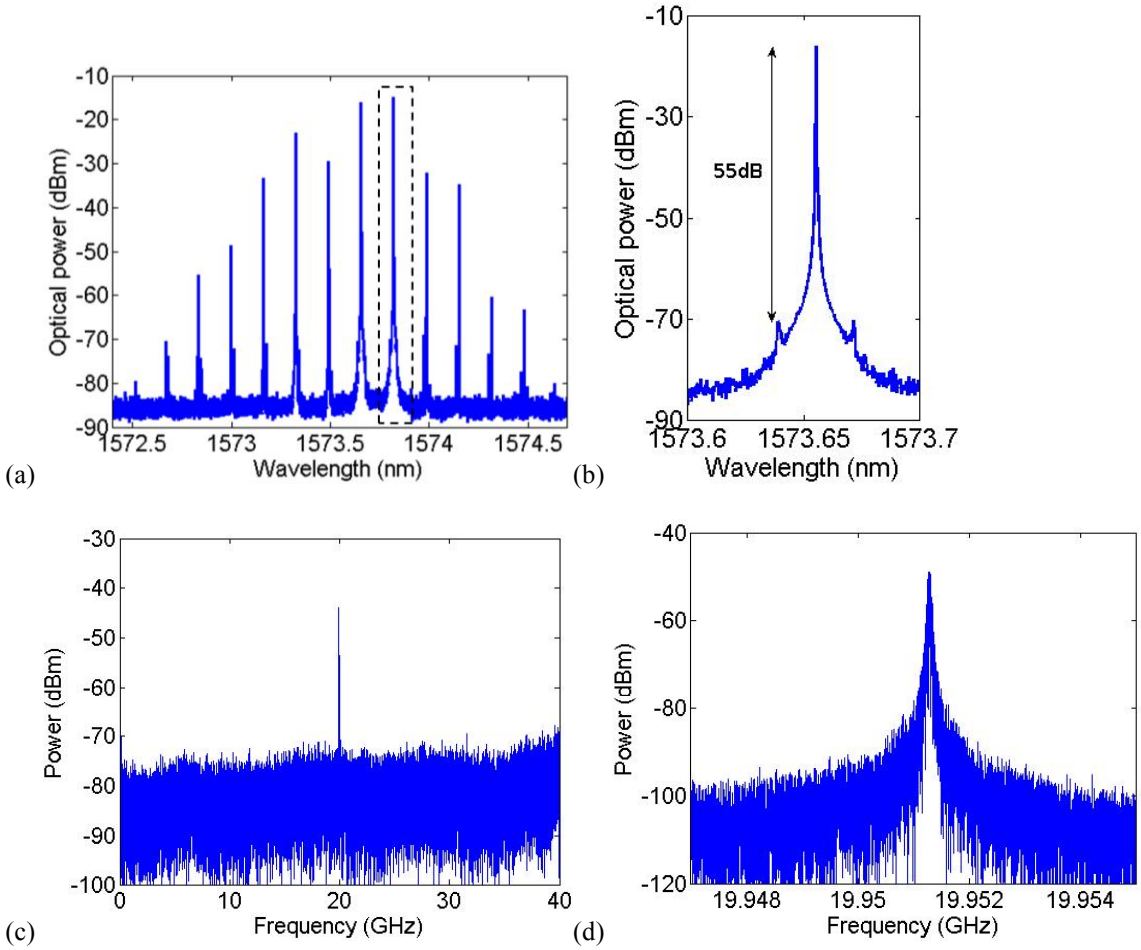


**Figure 2.5. Optical spectrum – (a) wide span and (b) close-up into the dashed box region in (a), electrical spectrum – (c) wide span and (d) close-in, for the MLLD with a 20GHz FSR intra-cavity filter. The RBW in (c) and (d) are 3MHz and 1kHz respectively. The SOA current is 220mA and the SA voltage is -0.5V [23] © 2014 IEEE.**

Figure 2.5 shows the optical and electrical spectrum taken at an SOA current of 215mA and absorber voltage of -1.3V. At this stage, the absorber has no RF drive and the plots indicate passive mode-locking. With this design we were able to achieve up to 55dB optical side mode suppression at the peak of the comb. The ESA shows a clean spectrum with a peak at 19.951GHz and no harmonics of the 2GHz cavity seen. The 3dB RF linewidth estimate is 52kHz using a Voigt fit. In order to quantify the improvement we also fabricated

20GHz fundamental ring laser cavities with the same absorber length. We will now present results from this laser and compare optical and microwave phase noise from both lasers.

The 20GHz fundamental ring cavity mode-locked laser (see Figure 2.6) consists of a ~4mm long ring resonator on silicon coupled to a bus waveguide using an 85:15 multi-mode interference (MMI) coupler. The 50μm long saturable absorber is centered in a 1mm long semiconductor optical amplifier (SOA). The output waveguides are angled and facets anti-reflection (AR) coated to minimize reflections.

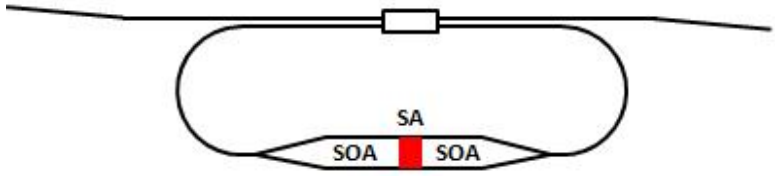


**Figure 2.6. Schematic of the gain, absorber and waveguide sections inside the laser cavity [12].**

The laser showed fewer optical comb lines, as shown in Figure 2.7 (a). The gain section was biased with 189mA and the saturable absorber was at 0V. The fiber coupled output power was 1mW with an estimated 6dB coupling loss. The electrical spectrum in Figure 2.7 (b) is obtained from collecting the laser output using a 50GHz photodiode followed by 21dB RF gain to lift the spurs above noise floor. We see two tones corresponding to the fundamental and its harmonic. Additionally we see spurs at ~1.5GHz and its beat note (~18.5GHz) with the fundamental, within the analyzer bandwidth. The power at these spurs increase with increasing injection current into the SOA. We believe these spurs are due to a group of optical modes that not locked with the main group of modes and have a pulse repetition rate offset of ~1.5GHz from the fundamental frequency. The 3dB RF linewidth was 1.5MHz, nearly 30 times larger than the previous case because of the reduced ratio of the passive section length to the gain section length.

The major pulse broadening effects are spectral gain narrowing, caused by the finite gain bandwidth of the laser medium, and cavity dispersion. We hypothesize the limitation in optical bandwidth is coming from the tapers that not only control propagation loss, across wavelength, through mode mismatch but also through absorption by the quantum wells if insufficiently pumped. The net effect is the lasing wavelength is red-shifted, and excitation of the higher order lateral mode modulates the gain spectrum across wavelength which reduces the optical bandwidth.

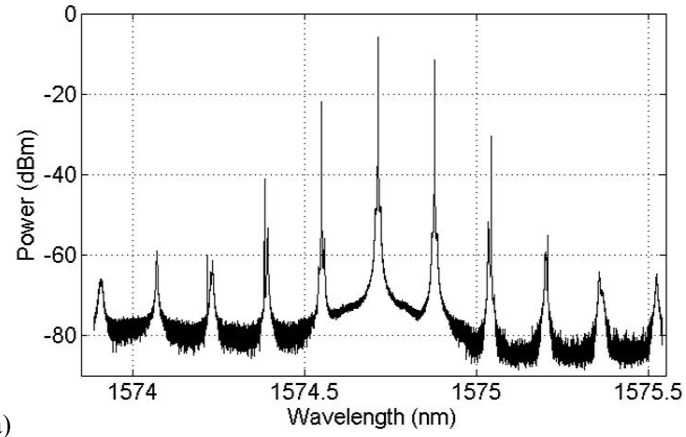


(a)

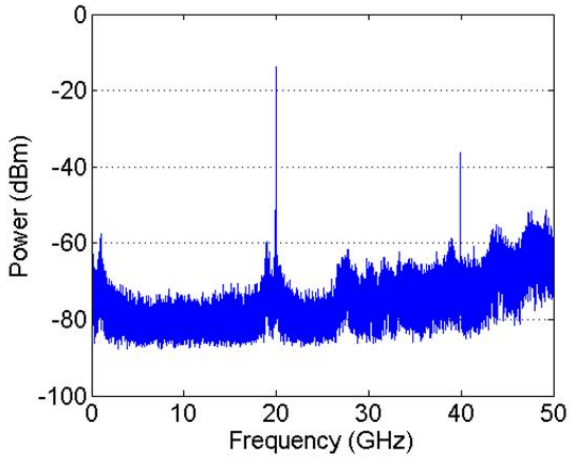


(b)

**Figure 2.7. (a) Optical spectrum of the ring cavity laser showing 20GHz spaced optical lines (resolution bandwidth 20MHz) and (b) electrical spectrum showing the fundamental and its harmonic. Notice the spurs at 1.5 and 18.5GHz [12].**

The optical linewidths from a heterodyne measurement are shown in Figure 2.8 (a), for both lasers. The reference fiber laser linewidth was 30kHz. We see a 10× improvement in

optical linewidth from the increased cavity length. The linewidth also grows quadratically around the central mode as expected. The phase noise of the microwave frequency generated from these two lasers is shown in Figure 2.8 (b). 20dB of off-chip optical gain was used in the case of the harmonically mode locked laser for this measurement. The 30× improvement in linewidth shows up as 14dB (= 10log10(30)) improvement in the $1/f^2$ phase noise. The timing jitter obtained from integrating phase noise from 100kHz to 100MHz reduces from 4.3ps to 1.3ps. We hypothesize the reason for deviation from the $1/f^2$ line in Figure 2.8 (b), is spurious reflections from the tapers within the laser cavity. On the other hand, the phase noise result from the long cavity laser is comparable to the state of the art results for quantum well based semiconductor passively MLLDs. This demonstration is also the first of its kind with all the photonic elements of the MLLD to achieve low phase noise integrated on a single chip.

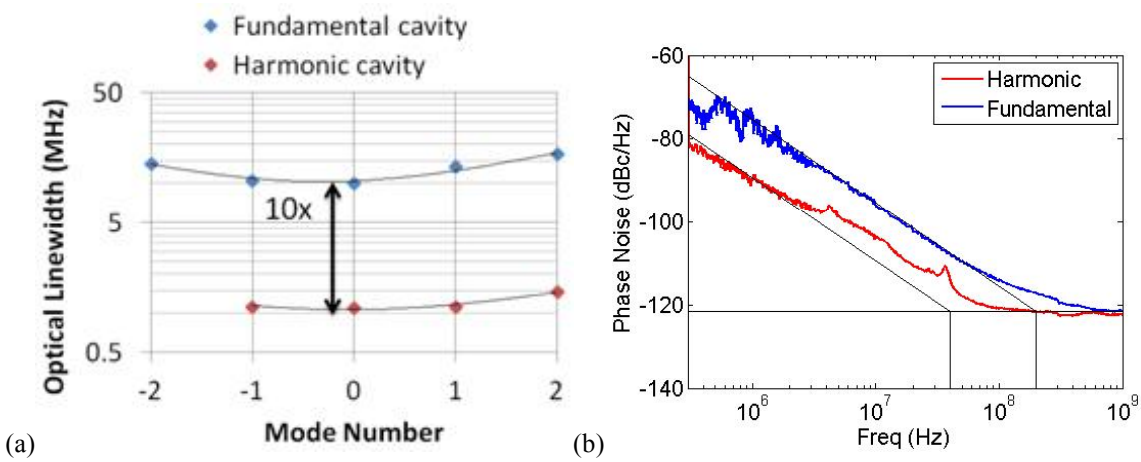


**Figure 2.8. (a) Optical linewidth measurement and (b) single sideband phase noise of the 20GHz signal for the fundamental and harmonic MLLDs. The black lines in both plots are a guide to the eye with an ideal quadratic dependence with frequency [12].**

We now recap all the results sequentially for ease of following. First, we presented passive mode-locking results from a MLLD with a fundamental repetition rate of 2GHz. The laser was designed to harmonically lock at the tenth harmonic by incorporating a silicon ring

resonator with a 20GHz FSR monolithically integrated inside the 2GHz laser cavity. This technique was used to achieve low microwave phase noise from the long passive section length while maintaining a high operating frequency. The physics of the filter operation inside the laser cavity can be understood in both the time and frequency domain. Conventional harmonic mode-locking of a 2GHz cavity at 20GHz, say using a signal generator driving the saturable absorber, generates ten independent (or uncorrelated) pulses circulating inside the laser cavity. This is because each of the ten pulses grows to their steady state value independently from uncorrelated spontaneous emission events. In the time domain, the ring resonator mixes each of the ten pulses inside the 2GHz cavity because of it memory effect. This constant mixing of photons among the ten pulses helps the gain section to correlate the photon phases. The greater the quality factor (Q), the greater is the correlation strength and the spur mode suppression is enhanced. In the frequency domain, the drop port spectrum of a ring resonator super-imposes onto the cavity loss thereby reducing the contention for gain from other longitudinal cavity modes except for the modes aligned with the passband of the resonator.

Second, we showed results from a 20GHz fundamental mode-locked laser. We observe a 30× increase in RF linewidth and a 10× increase in optical linewidth of the individual comb lines. We also observe a 14dB increase in the Lorentzian phase noise of the 20GHz microwave frequency in the short cavity laser. Thus we demonstrate an approach to lower phase noise in passively mode-locked lasers using the hybrid silicon platform which provides both silicon based low loss passive components viz. waveguides, ring resonators, and MMI couplers and active gain or loss sections to realize high frequency and low phase noise microwave signals. Further increase in length is possible by integrating low loss silicon nitride waveguides [25] with the gain regions [26].

Future work in terms of hybrid section optimization would include analyzing structures with modified confinement factor, by changing the Si waveguide width or reducing the number of quantum wells, for optimum gain and absorption saturation. The trade-off between output power saturation and confinement factor for different optical mode widths are shown in Reference [27]. However, the Si waveguide width is not a free parameter for confinement control because in wide waveguides the optical mode width in the active region increases beyond the current channel width and the overlap with unpumped quantum well section increases, thereby increasing loss. Therefore, the current channel width also needs to be altered for wide waveguide designs. Widening the Si waveguides can also start supporting higher order lateral modes which start contending for gain and reduce the laser efficiency significantly. Ultimately the overlap of the optical mode with the charge carriers in the quantum well needs to be optimized. More experimental results, including results from other lasers on the same die, is included in Chapter 5 and Appendix 2 for interested readers.

### *C. Coupled Cavity Mode-Locked Lasers*

Some of the better phase noise results for a MLLD use quantum dot (QD) active region and the low optical confinement factor in the QD material is often cited as the primary reason for reduced timing jitter, because of reduced amplified spontaneous emission [28]. The hybrid silicon technology inherently allows the manipulation of the confinement factor in the quantum well (QW) active region by means of changing the silicon waveguide width underneath. One can also incorporate fewer QWs in the active region to reduce confinement further. In this text we discuss the integration of a 1.3μm QW based colliding pulse mode-locked laser with two different QW numbers, three and five. In order to get further reduction

in optical and microwave linewidth, we adopt the technique shown in References [14, 29, 30], where a portion of the pulse emitted from the laser is fed back into the cavity to reduce amplified spontaneous emission (ASE) noise. We achieve the feedback on chip, without the need for any coupling optics by adding a ~4cm long waveguide delay at the output of the laser back mirror and terminating with a semiconductor optical amplifier (SOA) followed by a 100% reflecting loop mirror. The purpose of the SOA was to overcome the losses of the waveguide delay and also serve as a control switch to adjust the level of on-chip feedback. This technique of stabilization using intentional feedback is also known to stabilize the laser from other unknown spurious reflections, which can come from the rest of the photonic circuit.

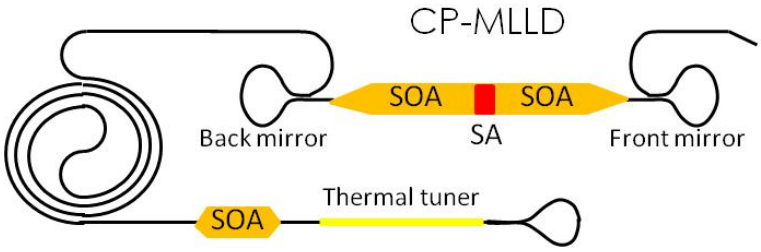


**Figure 2.9. Schematic showing the laser circuit. Black lines indicate the silicon waveguide, SOA-semiconductor optical amplifier, SA-saturable absorber.**

The schematic of the photonic circuit is shown in Figure 2.9. Traditionally the cavity length of linear cavity mode-locked lasers is difficult to control precisely as they depend either on cleaving or polishing the facets that act as the laser mirrors. In our design we make use of Sagnac loop mirrors in silicon to form mirrors on both sides of the gain section. This way we keep the advantage of precisely controlling the repetition rate like in ring cavity lasers shown in Section B. The mirror reflectivity is determined by the coupling strength of the directional coupler in the Sagnac loop mirror. Near 100% reflection can be achieved by making a 50:50 directional coupler. All the lasers reported in this section have the same

circuit configuration and the only variation is in the number of quantum wells in the active region. The basic colliding pulse mode-locked laser diode (CP-MLLD) consists of 1.2mm long SOA with a centered 40μm absorber and two 15μm isolation sections, one on either side of the absorber. The reflectivity of the front facet is 10% and that of the back mirror is 55%. The total cavity length is 3.934mm which corresponds to a fundamental cavity frequency of 8.7GHz. The output of the front facet loop mirror is terminated at the chip facet at an angle to avoid reflections. The output from the back mirror goes through a spiral silicon delay line followed by an SOA and a 100% loop mirror reflector using a 1×2 MMI. The total feedback cavity length is 39.343mm, which is designed to be exactly ten times the base laser cavity length. There is a thermal tuner in the feedback cavity to control the phase of the fed back pulses. The feedback cavity SOA is 560μm long to partially compensate the waveguide loss. The total device area is $2.5\times1\text{mm}^2$.

We divide the experimental results into two parts. First, we consider the various laser cavities without feedback. This corresponds to applying a -3V bias on the feedback cavity SOA. Using gain measurements on a different SOA of the same length, the estimated single pass loss is >20dB at this bias. The feedback was negligible as the thermal tuner had little effect on the microwave signal. Second, we consider the same laser cavities with feedback and show the region of optimum bias conditions to achieve narrow linewidth. All the experiments were carried out on a temperature controlled stage kept at 20°C. The RF port of the bias-T connected to the absorber was terminated at 50Ω. The light output is collected using a 2μm spot-size lensed fiber, which is spliced to a 37dB return loss isolator.

1. Without On-Chip Feedback

The light-current (L-I) curves for the device with five and three QWs are shown in Figure 2.10. The threshold current is slightly higher for the five QW laser as expected, and the fiber coupled output power level is comparable. We begin with identifying the bias conditions for mode-locking in colliding pulse operation. The light output is collected with a high speed detector with a bandwidth and responsivity of 50GHz and 0.23A/W respectively. Figure 2.11 shows the RF spectrum for the two devices in colliding pulse operation at the optimum bias point. We observe a greater suppression of the fundamental in the three QW device by more than 13dB. We also notice a noise pedestal at the foot of the 17.4GHz signal for the five QW device.

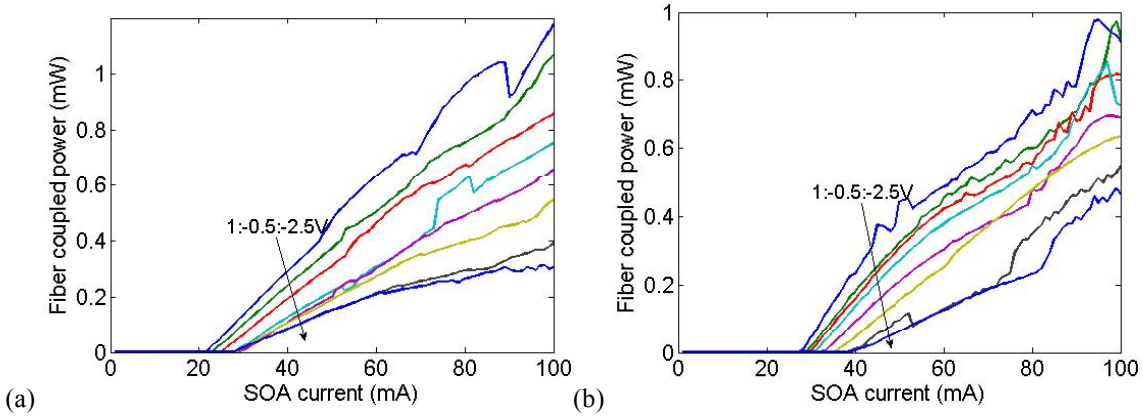


**Figure 2.10. (a) Light-current curves for different absorber bias voltages for three (a) and five (b) QW device.**

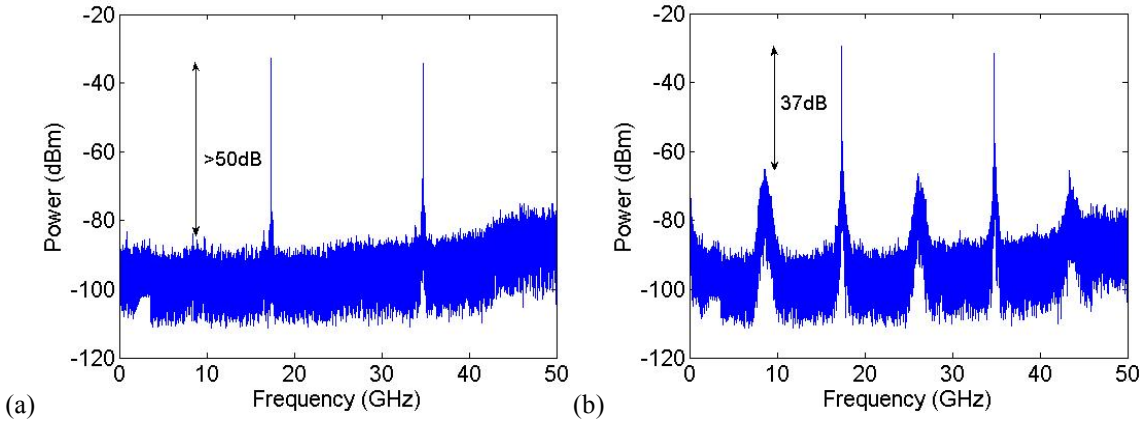

**Figure 2.11. (a) RF spectrum (resolution bandwidth-RBW 3MHz) for the three (a) and five (b) QW device. Bias points (a) 75mA-SOA current, -0.4V-SA voltage and (b) 67mA-SOA current, -0.8V-SA voltage.**

We then obtained the optical time and frequency domain data of the laser output at these bias points. Figure 2.12 shows the optical spectrum from the two lasers. The lasing wavelength is red shifted in the five QW device, most likely due to the increased absorption in any of the un-pumped areas of the hybrid section, which include the isolation region and a portion of the tapers. Another interesting observation is the difference in the peak to valley extinction ratio for the comb lines (distance between the top and bottom envelope). The ASE noise power is significantly higher in the five QW device.

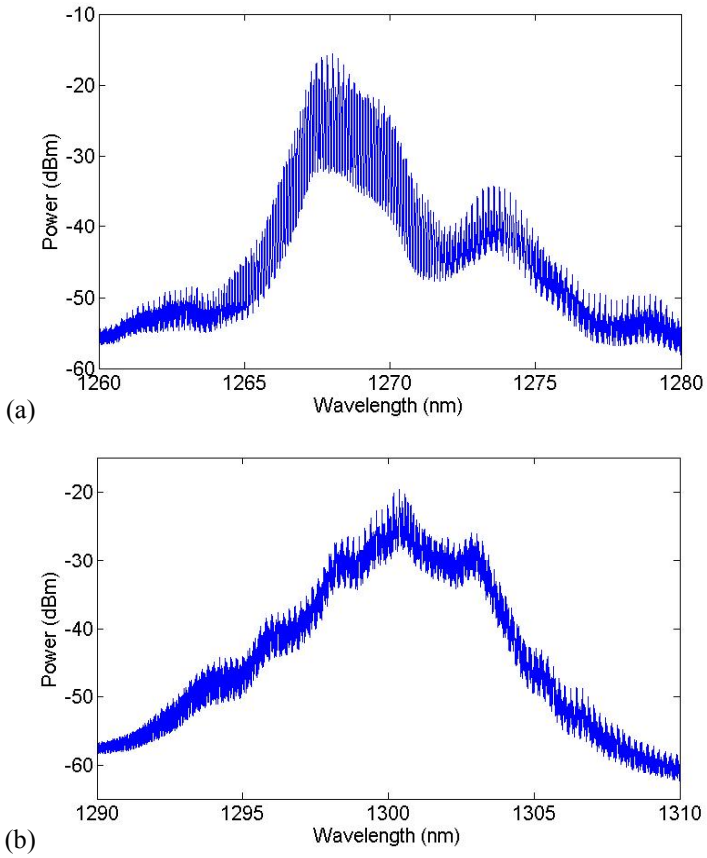


**Figure 2.12. Optical spectrum (RBW-0.02nm) for the three (a) and five (b) QW device. Bias points are the same as in Figure 2.11.**

The laser output was amplified using a praseodymium-doped fluoride fiber amplifier (PDFA) to measure the autocorrelation signal. Figure 2.13 compares the optical pulses

obtained from the two devices. Since the lasing wavelength was not the same, the gain from the PDFA was different in the two cases and the strength of the autocorrelation signals were different despite the comparable optical power from the devices. The pulsewidths for the three and five QW devices are 7.7ps and 4ps respectively. The corresponding time-bandwidth products (TBP) are 0.335 and 0.348 respectively. The five QW device shows a pedestal, indicative of a slow decay or a trailing pulse. The trailing pulse could come from one of two reasons. First, the insufficient suppression of the group of modes locked at the fundamental appears as a daughter pulse once every two cycles. Second, the daughter pulse has the same repetition rate as the main pulse and is from a second group of higher order lateral modes in the cavity. We will discuss more on this topic in the following paragraphs.

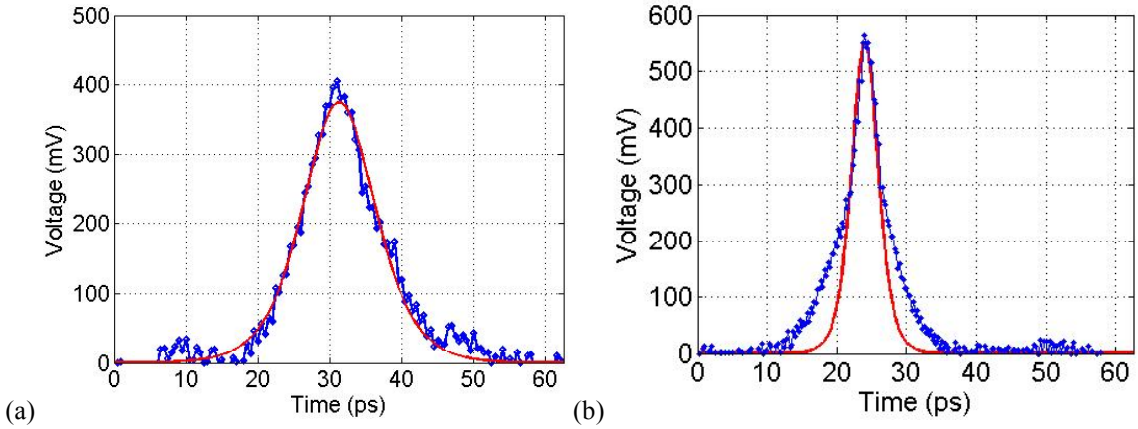


**Figure 2.13. Autocorrelation traces (blue) for the three (a) and five (b) QW device. Bias points are the same as in Figure 2.11. The red lines are the sech-squared fit to data.**

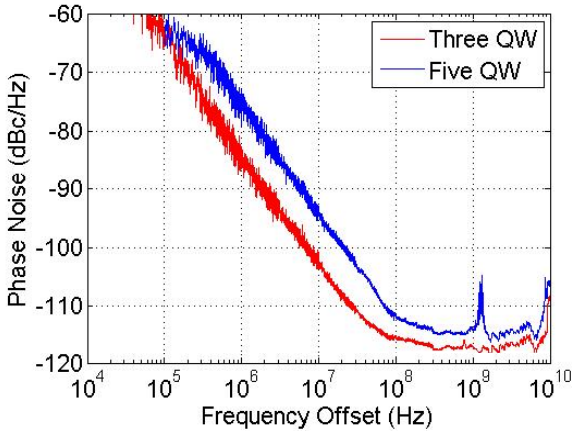

**Figure 2.14. Phase noise comparison of the 17.4GHz signal for the three and five QW devices. Bias conditions are the same as in Figure 2.11.**

Figure 2.14 shows the improvement in phase noise of the microwave signal by reduced spontaneous emission in the three QW device. The improvement is as large as 8dB in the $1/f^2$ region. On the same note, the 3dB linewidth of the three QW device was 44kHz while that of the five QW device was 200kHz. The spur at ~1GHz in the phase noise of the five QW device is an indication of reflections of the SOA taper in the feedback cavity. The timing jitter obtained from integrating the phase noise from 100kHz to 100MHz, was 2.7ps and 9.5ps for the three and five QW device respectively. We now discuss measurements with on-chip feedback.

2. With On-Chip Feedback

While the lasers are in colliding pulse operation as shown in the previous section, we start applying a forward bias to the SOA to increase the power being fed back into the lasing cavity, and mapping the microwave linewidth for various feedback cavity SOA current and thermal tuner current. Changing the feedback SOA current corresponds to changing the reflectivity and changing the thermal tuner current alters the phase delay.

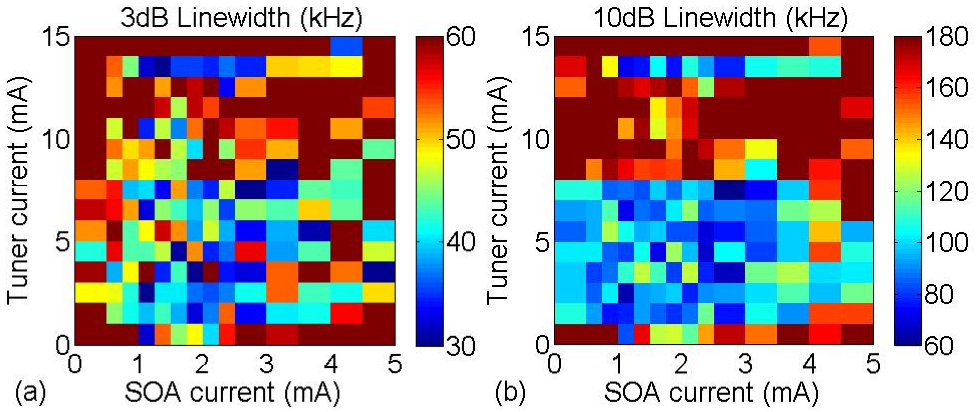

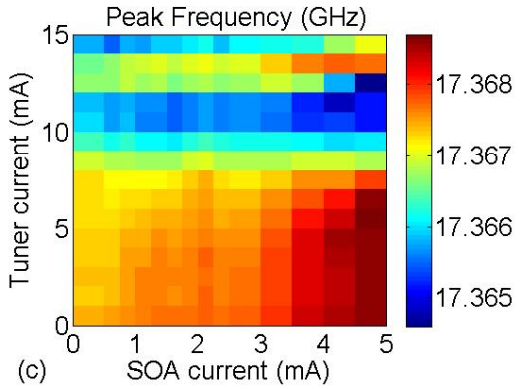


**Figure 2.15. (a) 3dB, (b) 10dB linewidth and (c) oscillation frequency of the microwave signal as a function of feedback SOA current and thermal tuner current. The optimum bias condition is at 2.5mA SOA current and 7mA tuner current. Data measured from three QW device.**

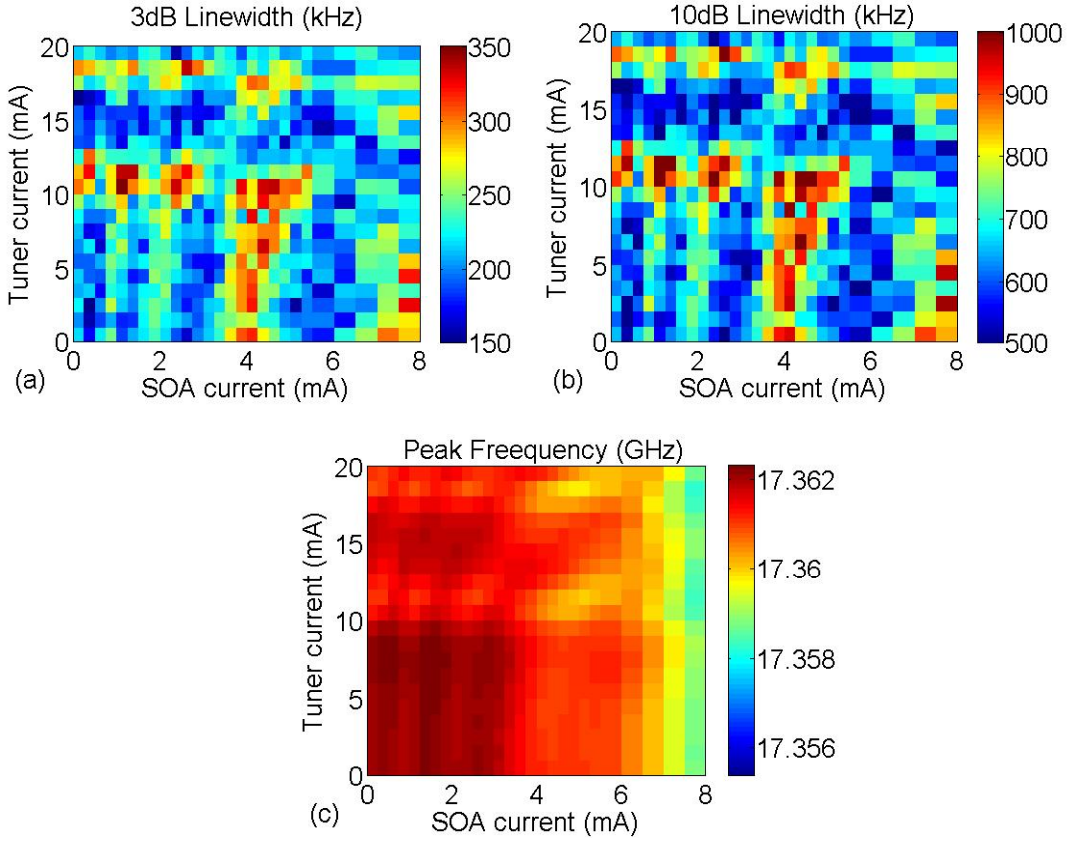


**Figure 2.16. (a) 3dB, (b) 10dB linewidth and (c) oscillation frequency of the microwave signal as a function of feedback SOA current and thermal tuner current. The optimum bias condition is at 0.25mA SOA current and 2mA tuner current. Data measured from five QW device.**

We measure the RF spectrum by averaging ten traces with a sweep time for each trace set to 125ms. The linewidth is extracted by fitting a Lorentzian to the data. The linewidth measurements were taken when the laser SOA was pumped using a battery powered supply

to reduce the amount of Gaussian noise added. Figure 2.15 and Figure 2.16 show the influence of on-chip feedback cavity for the three and five QW devices, respectively. The desired region of operation for narrow linewidth is the blue shaded regions in plots (a) and (b). The five QW device shows a more clear pattern for regions of linewidth narrowing than the three QW device. The islands of instability are periodic and grow in size with increasing SOA current. In both cases, the linewidth starts to re-broaden for large SOA currents and eventually fails to mode-lock. The re-broadening is due to the increased ASE noise being injected back unfiltered into the cavity and eventually the round trip gain of the feedback cavity longitudinal modes is sufficient to start multi-mode operation and we observe periodic spur tones around the comb frequencies. The optimum bias conditions for the three QW device was found at 2.5mA SOA current and 7mA tuner current. The 3dB linewidth is reduced from 44kHz to 29kHz. For the five QW device the optimum bias was at 0.25mA SOA current and 2mA tuner current. The 3dB linewidth was reduced from 200kHz to 136kHz. The linewidth is reduced by ~1.5 times in both cases.

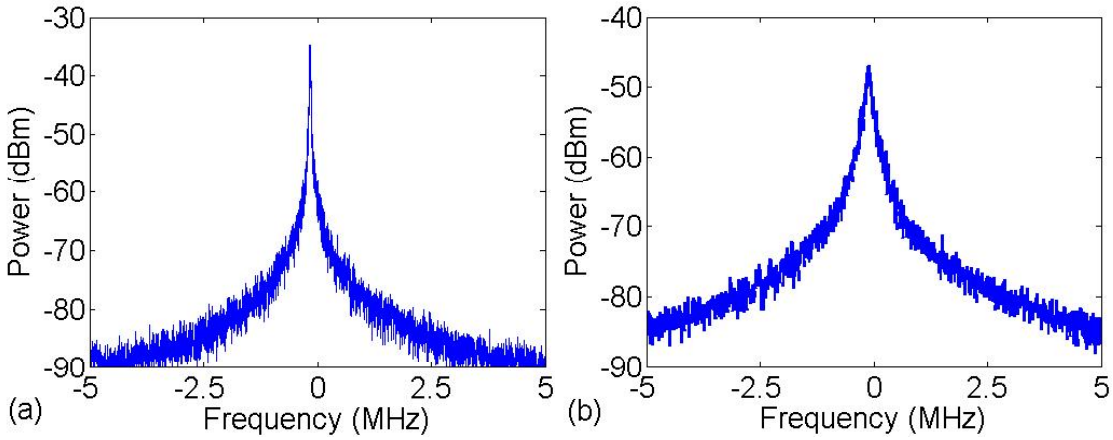


**Figure 2.17. RF spectrum showing the best linewidth achieved with feedback for the three (a) and five (b) QW device centered at 17.362GHz and 17.367GHz respectively. RBW-10kHz.**

Table 3.1 shows the summary of linewidths with and without feedback for the two devices. For a perfect Lorentzian lineshape, the 10dB linewidth should be 3 (=√9) times the

3dB linewidth and the 20dB linewidth is ~10 (=√99) times the 3dB linewidth. The five QW device shows an ideal Lorentzian behavior as the linewidth is quite broad, however, the three QW device shows broadening from excess Gaussian noise, despite using battery powered supplies. This could be from temperature fluctuations. If we disregard the Gaussian noise contribution and fit a pure Lorentizan to match the 20dB linewidth, the 3dB linewidth is at best ~16kHz (=159/√99), which is a record for QW based mode-locked laser diodes. The RF spectrums for the optimal bias conditions of feedback for both three and five QW device are shown in Figure 2.17. For comparison, the timing jitter by integrating phase noise from 100kHz to 100MHz for the three QW device improved from 2.7ps to 1.2ps using feedback. This is similar to the value achieved in the harmonically mode-locked long cavity laser covered in the earlier section.

**TABLE 3.1**
**Summary of linewidth improvement with on-chip feedback.**

| RF linewidth (kHz) measured @ | Three QW device | |
|---|---|---|
| | Without feedback | With feedback |
| 3dB | 44 | 29 |
| 10dB | 103 | 60 |
| 20dB | 292 | 159 |
| | Five QW device | |
| 3dB | 200 | 136 |
| 10dB | 607 | 409 |
| 20dB | 2010 | 1356 |

3. Discussion

In this section we will analyze the measurement results and provide suggestions to improve the laser performance in the future. We shall start the discussion with the expression for RF linewidth ($\Delta\nu_{RF}$) in a mode-locked laser [31], re-written here as Eqn. 3.1.

$$\Delta\nu_{RF} = C_1\left(\Delta\nu_{ST}\right) + C_2\left(RIN\right) \tag{3.1}$$

where the expressions for $C_1$ and $C_2$ can be found in Reference [31]. $\Delta\nu_{ST}$ is the Schawlow-Townes optical linewidth. The first term is the direct contribution of optical phase noise to microwave phase noise and the second term is the noise due to AM-PM conversion, also known as the coupling between energy and timing fluctuations of the pulses in the cavity. The second term is usually quite small for semiconductor lasers because the relative intensity noise (RIN) is quite low. As indicated earlier in this chapter, the optical phase noise originating from spontaneous emission can be lowered by reducing the confinement factor ($\Gamma$) of the optical mode. The cavity being three dimensional, the confinement factor can be separated into the individual confinement factors in the lateral ($\Gamma_x$), transverse ($\Gamma_y$) and longitudinal ($\Gamma_z$) direction, i.e. $\Gamma=\Gamma_x\Gamma_y\Gamma_z$. In the lasers described in this section, we reduced the transverse confinement by reducing the number of QW and the longitudinal confinement by using the external cavity. Both techniques help to reduce the microwave linewidth. However, as observed in Reference [14] the reduction from the feedback cavity was not as appreciable as the mode-locking optical bandwidth was quite low (<100GHz). On closer inspection of the optical spectrum, we find that the reason for low bandwidth is because of the existence of a higher order lateral mode with a different group index, which modulates the gain spectrum due to the Vernier effect. Mode-locking happens only when both groups of modes are locked.

On reviewing the results, we propose the following suggestions to improve the laser performance. First, the back mirror reflectivity was designed to be quite high in the interest of keeping the output power from the front mirror high. Since the optical linewidth reduction increases with decreasing back mirror reflectivity, the reflectivity can be reduced to allow

greater coupling to the external cavity. Second, since the power out of the back mirror is sufficiently high and the waveguide loss was quite low (<1dB/cm) the feedback cavity SOA can be removed and replaced with a variable optical attenuator (VOA) such as a Mach-Zehnder interferometer (MZI) switch in the external cavity or an MZI based loop mirror to directly tune the coupling between the two cavities. This reduces the ASE noise introduced in the feedback cavity. If the SOA is necessary, then a filtered feedback configuration using ring resonators is necessary to filter out the excess noise. Third, longer delay lines can be fabricated for lower waveguide loss systems. A general rule being the length of the feedback cavity $L_p$ should be less than $1/(2\alpha)$, where $\alpha$ is the waveguide propagation loss in $cm^{-1}$ [32]. Last, we could reduce the number of quantum wells further, but should also increase the absorber length accordingly.

### *D. Summary*

To recap the experimental data presented in the previous two sections, we demonstrate two main techniques to lower microwave phase noise in high repetition rate passively mode-locked lasers. First, we try incorporating a long passive section inside the laser cavity to reduce the longitudinal confinement factor. We also show that adding a ring resonator into the cavity can successfully suppress the optical supermodes of the cavity spaced at the fundamental repetition rate of the long cavity by more than 55dB. Although the microwave phase noise was reduced by 14dB, the output optical power was lowered from introducing the long passive section because of finite waveguide loss.

Second, we try designing the laser by moving the long passive section outside the laser main cavity and make a coupled cavity laser. The output optical power and threshold current are preserved in this design, however, the reduction of phase noise from external feedback

was limited to 6dB. This can be improved by removing the SOA from the long feedback cavity because the waveguide loss was low enough to provide sufficiently high feedback in one roundtrip. Furthermore, the SOA was converting most of the coherent photons in the pulse to incoherent ones. Reducing transverse confinement by reducing the number of quantum wells from five to three was very effective as we observed nearly 8dB microwave phase noise improvement. Thus we have developed two fully integrated chip scale mode-locked laser designs that can be used in the generation of high frequency and low jitter microwave signals.

# 3. Lowering Phase Noise of Tunable Lasers

Semiconductor tunable laser research has a long history and has influenced many applications like optical cross connects, dynamic add/drop multiplexers, wavelength conversion, and dense wavelength division multiplexing (DWDM) sparing in high capacity long haul communication links. This is mainly because of their compact size and low power consumption. As optical communications shift to more complex modulation formats, narrow linewidth lasers become a necessity. For example, a 16-QAM modulation format requires a laser linewidth <300kHz [33]. Furthermore for DWDM based systems, lasers have to be tunable to align to a certain grid. Tuning can also be exploited in switching scenarios and for improving network resilience to downtime and typically requires tuning across the communication band. One of the key challenges to this day has been to achieve both narrow linewidth and wide tunability for a semiconductor laser.

In this chapter we present two tunable diode lasers that each use the linewidth reduction techniques introduced in Chapter 1. In order to continue from where we left in Chapter 2, the first laser we discuss uses an on-chip delayed feedback which narrows the laser linewidth by more than a factor of three and achieves a linewidth below 100kHz in its entire 54nm tuning range. In the second laser we identify a negative optical feedback effect from the resonant laser mirrors that reduces the laser linewidth down to 160kHz. We believe these techniques can be exploited in future designs to realize compact narrow linewidth tunable lasers.

## *A. Coupled Cavity Tunable Laser*

In this section we theoretically analyze, design and measure the performance of a widely tunable semiconductor laser integrated with an on-chip external cavity. Controlling both the

feedback strength and phase from the integrated external cavity to the laser is essential to improve the performance. The advantages of monolithically integrating the external cavity are improved stability, no tightly controlled anti-reflection coating of the laser facets, no external alignment of mirrors, and lower coupling losses caused by mode-mismatch. The external cavity used here comprises of a 4cm long silicon (Si) waveguide, which is an order of magnitude longer than the length of the main laser cavity.

We organize the laser results into four sub-sections. First, we provide the design details of the fabricated laser followed by a theoretical analysis of the influence of the external cavity and its influence on laser linewidth, modulation response and relative intensity noise (RIN). Next, we show the measured data for wavelength tuning and laser linewidth. Finally, we summarize our results and suggest further improvements that can be made to the laser.

1. Laser Design

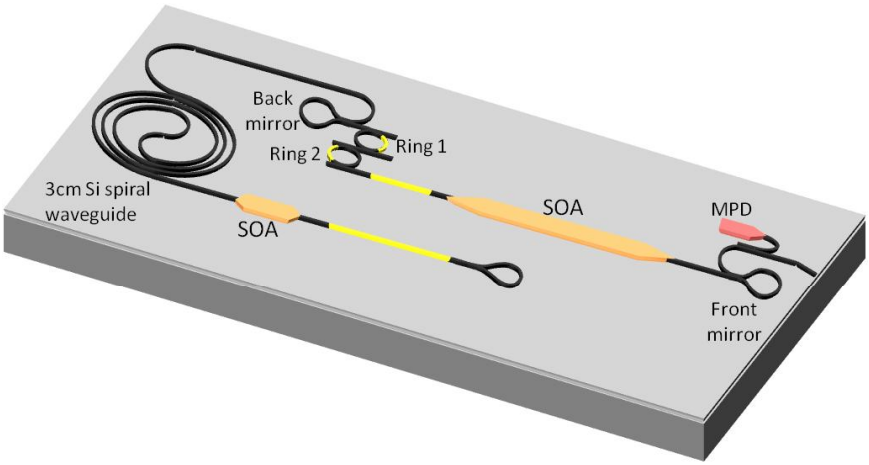


**Figure 3.1. A schematic view of the tunable laser, with an integrated external cavity. Tuners are yellow (two phase sections and two rings for wide tuning), and SOAs are orange (one is the laser active section, and one is used as an ON/OFF switch or to control the level of feedback). The monitor photodiode (MPD) is used to measure the laser output power for adjustment of laser parameters.**

A schematic of the monolithically-integrated widely-tunable laser with external cavity is shown in Figure 3.1. A 1.2mm long gain section is placed inside a ~2.5mm long Fabry-Perot

(FP) cavity formed using Sagnac loop-mirrors in silicon. The lasing wavelength is determined by the tuning section comprising of two silicon microring resonators and a cavity phase section, all of which are controlled by thermal phase tuners. The front loop mirror (at the output of the laser) has a 10% power reflection and the output of the laser is terminated at the facet at an angle of 7° to minimize reflections. The back loop-mirror, after the wavelength tuning section, has a power reflection of 60%, and the rest of the light is fed into the external cavity. In order to allow for a long external cavity, a low-loss waveguide platform is needed. Here we utilize optimized silicon waveguides with a propagation loss of 0.67dB/cm. The external cavity is ~4cm long and has its own phase adjustment section and a 560μm long semiconductor optical amplifier (SOA). As the propagation loss in Si waveguide is very low, there is quite strong feedback from the external cavity (~5dB loss per round-trip). The feedback is present even when the SOA in the external cavity is reverse-biased, possibly from reflections at its tapers or from its insufficient attenuation. The external cavity is attached to the main laser cavity on the side with the tuning section as the microrings filter out the broadband spontaneous emission from the feedback cavity SOA before reaching the gain section in the main laser cavity. The feedback cavity SOA can be forward biased to reduce the loss, amplify the light, or even make the external cavity lase at sufficiently high bias current.

### 2. Theory

We present the necessary equations that govern the linewidth, relative intensity noise (RIN) and modulation response of the fabricated external cavity laser. We include some necessary measurements to verify the theory throughout this section.

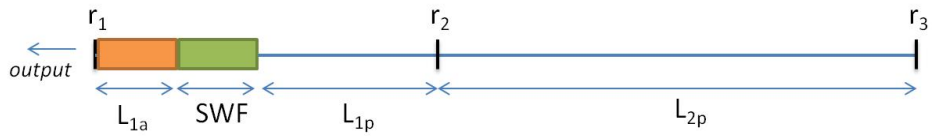


**Figure 3.2. Schematic of the laser used for modeling. SWF - single wavelength filter. Orange rectangle - gain section.**

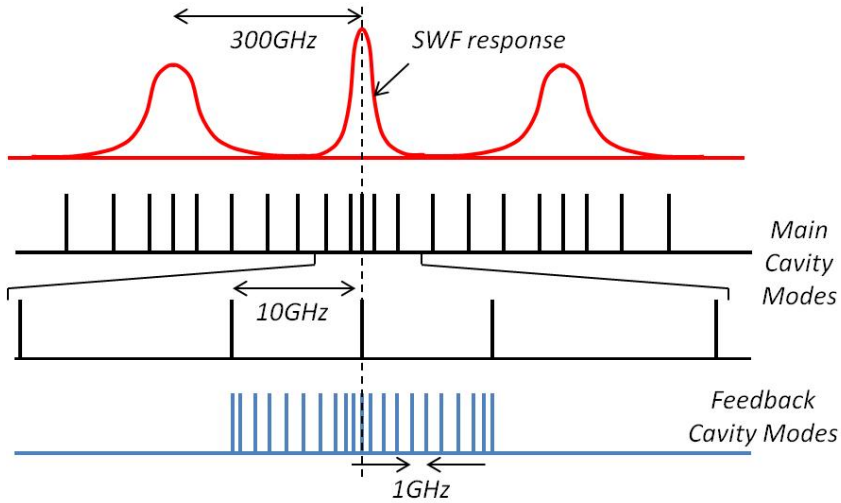


**Figure 3.3. The mode locations in the main cavity and the feedback cavity, showing non-uniform mode spacing. Only a few modes are shown for simplicity.**

The expressions shown in this section are re-derived from [34] and [35]. The laser cavity is modeled as shown in Figure 3.2. The tunable single-wavelength-filter is designed using the Vernier effect from the drop port response of two ring resonators with slightly different radii. We would like to study modes from two base cavities. One formed between $r_1$ and $r_2$, which we call the main cavity and the other between $r_2$ and $r_3$, which we call the feedback cavity. Figure 3.3 shows the mode spacing from the two cavities. We observe that the mode spacing is not uniform due to the cavity length enhancement or enhanced photon lifetime for wavelengths near the ring resonator transmission maximum. This is true even for the feedback cavity modes as the photon lifetime is enhanced for the wavelengths around the main cavity modes. We see this effect in the modulation response of the device, as shown

later in the text. The feedback cavity length is nearly ten times the main cavity length and hence has much smaller longitudinal mode spacing.

In order to determine the linewidth reduction factor, we find the effective reflectivity of the cavity to the right of the gain section. This can be done in two steps. First, we consider the single wavelength filter (SWF) and the passive section ($L_{1p}$) along with $r_2$ to form an effective wavelength dependent high $Q$ mirror with reflectivity $r_{eff}$. Second, we derive the net reflectivity ($r_{eff}'$) including the external cavity as a response from a Fabry-Perot filter with reflectivities $r_{eff}$ and $r_3$. The expression for $r_{eff}$ and $r_{eff}'$ are

$$r_{eff} = r_2 X^2 \left( \frac{|\kappa|^2 Y}{1-\tau^2 Y^2} \right)^2 \left( \frac{|\kappa|^2 Z}{1-\tau^2 Z^2} \right)^2 \tag{4.1}$$

$$X = e^{-\alpha_p L_{1p}} e^{-j\beta_p L_{1p}} \tag{4.2}$$

$$Y = e^{-\alpha_p \pi R_1} e^{-j\beta_p \pi R_1} \tag{4.3}$$

$$Z = e^{-\alpha_p \pi R_2} e^{-j\beta_p \pi R_2} \tag{4.4}$$

$$r'_{eff} = \frac{r_{eff} + r_3 W}{1 + r_{eff} r_3 W} \tag{4.5}$$

$$W = e^{-2\alpha_p L_{2p}} e^{-2j\beta_p L_{2p}} \tag{4.6}$$

where $R_1$ and $R_2$ are the radii of the ring resonators. $\alpha_p$, $\beta_p$ are the waveguide electric field propagation loss and the effective propagation constant for the lasing mode respectively. $\kappa$, $\tau$ are the coupling and transmission field coefficients, respectively, for the couplers used in the rings. The linewidth reduction $F^2$ is then given by the following expressions [35],

$$A = \frac{1}{\tau_{in}} \mathrm{Re}\left\{ i \frac{d}{d\omega} \ln r_{eff}(\omega) \right\} \tag{4.7}$$

$$B = \frac{\alpha_H}{\tau_{in}} \mathrm{Im}\left\{ i \frac{d}{d\omega} \ln r_{eff}(\omega) \right\} \tag{4.8}$$

$$F = 1 + A + B \tag{4.9}$$

$$\Delta\nu = \frac{\Delta\nu_0}{F^2} \tag{4.10}$$

where $\alpha_H$ is the linewidth enhancement factor. $\tau_{in} = 2n_{eff}L_{1a}/c$ where $n_{eff}$ is the effective index of the gain section and $c$ is the speed of light respectively. $\Delta\nu$ and $\Delta\nu_0$ are the linewidths with and without the high $Q$ cavity enhancement respectively. The $A$ term, corresponding to the linewidth reduction from reduced longitudinal mode confinement, is often denoted as the ratio of the passive section path length to the gain section path length. The $B$ term corresponds to the reduction from the negative feedback effect where a decrease in wavelength, increases reflectivity thereby increasing photon density in the main cavity which decreases carrier density, ultimately increasing the wavelength due to the carrier plasma effect. This negative feedback effect occurs only on the long wavelength side of the resonance and is optimum at the wavelength of highest slope in the transmission spectrum. On the short wavelength side of the resonance the effect is reversed and operates in positive feedback, broadening the linewidth.

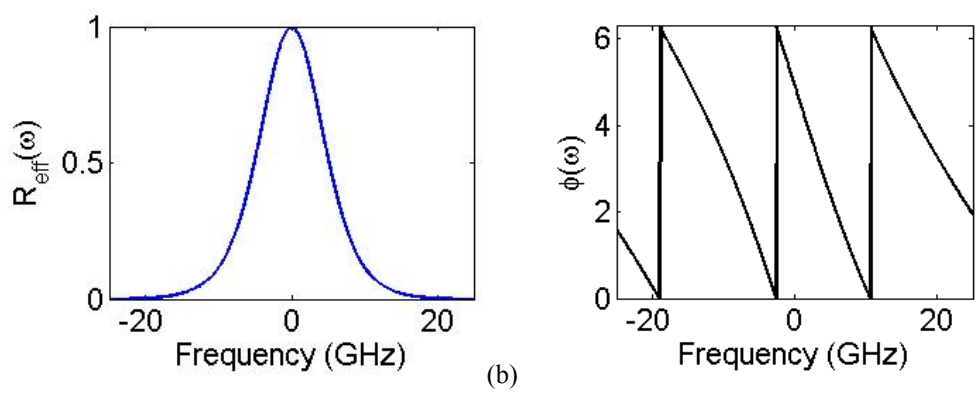


(a) (b)

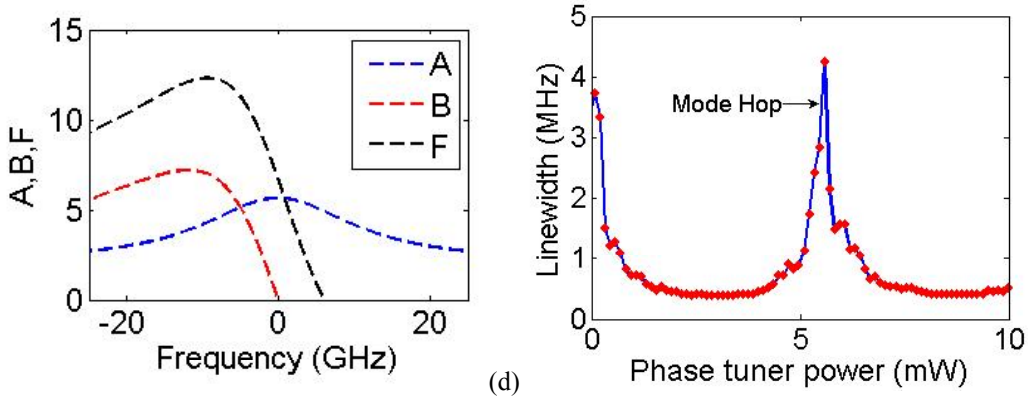


**Figure 3.4. Normalized reflection (a), phase (b) and linewidth reduction factor (c) of the laser without external cavity as a function of frequency offset from resonance ($\alpha_H$=4). (d) Measured linewidth (red diamonds) as a function of laser phase tuner power. The blue line is a guide to the eye.**

Figure 3.4 shows the effective reflection spectrum (a) and phase (b) for the laser without the feedback cavity. The lasing wavelength is decided by the phase condition $\varphi_{SOA} + \angle r_{eff}(\omega) = 2\pi$ where $\varphi_{SOA}$ is the roundtrip phase acquired in the gain section. Figure 3.4 (c) shows the wavelength dependent linewidth reduction. The wavelength dependence is asymmetric with respect to the resonance wavelength and the peak reduction is observed on the red side of the resonance. We observe this asymmetric dependence of linewidth reduction by tuning the phase of the main cavity with thermal tuner and recording the linewidth. Increasing the tuner current (or power) red shifts the lasing wavelength and decreases the linewidth. Figure 3.4 (d) shows the measured linewidth as a function of input tuner power. We see a reduction in linewidth from ~4MHz to 375kHz. We believe this is due to an increase in *F* from 3 to 9.6 over π radians. The pattern repeats after a phase change of 2π as the laser mode hops to the next cavity mode and the linewidth reduction process repeats.

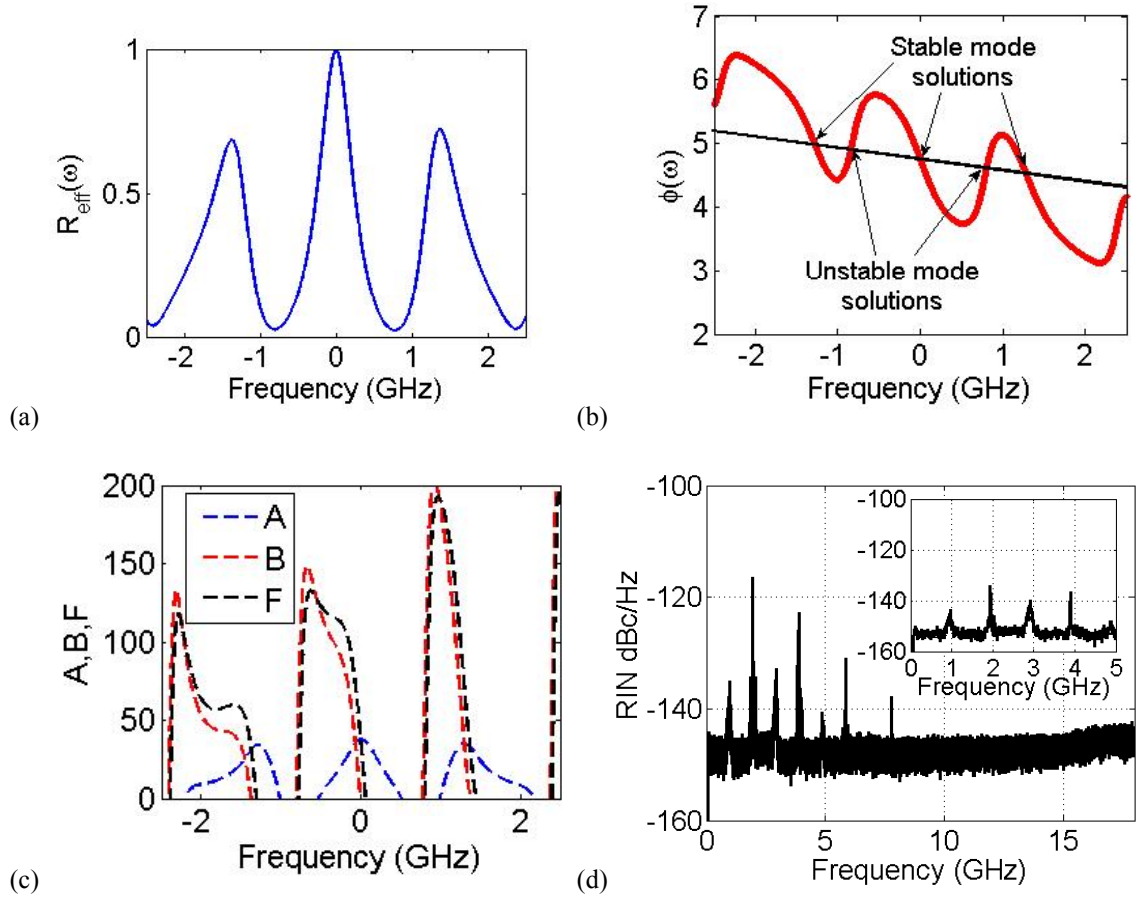


**Figure 3.5. (a) Normalized reflection, (b) phase and (c) linewidth reduction factor of the laser with external cavity as a function of frequency offset from resonance ($\alpha_H = 4$). (d) RIN measurement when external SOA is under high bias current (Resolution bandwidth (RBW) – 3MHz). Inset: Close-up RIN over a narrow frequency range showing alternating broad and narrow peaks. RBW – 500kHz.**

We can replace $r_{eff}$ with $r_{eff}'$ in Equations (4.7) and (4.8) to get the linewidth reduction with the external cavity. Figure 3.5 (a) shows the reflection spectrum with the external cavity. The original passband shown in Figure 3.4 (a) is modulated to give rise to a narrower passband (note the change in scale on *x*-axis). The phase condition is shown in Figure 3.5 (b) and shows an important feature due to the introduction of the feedback cavity. The laser cavity phase condition is met when the sum of the roundtrip phase in the SOA and the phase of the complex mirror reflectivity is $2\pi$. This is graphically shown as the intersection of the black line ($2\pi$- $\varphi_{SOA}$) and the red line (mirror phase). However, the points indicated unstable correspond to the saddle point stationary solutions [36]. Hence there exists alternating stable

and unstable mode solutions to the extended laser cavity. We observe this phenomenon in the RIN (amplitude noise) measurement when the external SOA is biased with a sufficiently large current. As seen in Figure 3.5 (d) we observe alternating broad and narrow peaks corresponding to the unstable and stable modes respectively. In the linewidth measurement we only observe the stable modes as the unstable modes are either too weak compared to the measurement noise floor or do not have any phase coherence. Figure 3.5 (c) shows the linewidth reduction achievable. We would like to point out that the A term in the external cavity case is not simply the ratio of passive section length to the gain section length but is attenuated by the roundtrip loss of the external cavity. This is the key difference to having the long Si delay line inside or outside the main lasing cavity, and explains the reason for the two approaches taken in the earlier chapter. At the cavity resonance the reduction factor (F) is roughly ~32 corresponding to a linewidth reduction of ~1000. We show this improvement in the measurement section. Red tuning the wavelength to get higher reduction was difficult in this case due to laser instability from mode hoping. By using higher *Q* ring resonators this mode hoping can be quenched.

We move on to the modulation response of the laser. The expression for the modulation transfer function *H(ω)* is adopted from [34] with the assumption that the lasing wavelength is not detuned from the cavity mode, for simplicity and we find this expression is sufficient to explain the measurements at operating conditions.

$$H(\omega) \cong \frac{\omega_R^2}{\omega_R^2 + (j\omega + \gamma)\left(j\omega + \kappa\left(1 - e^{-j\omega\tau_{ext}}\right)\right)} \tag{4.11}$$

$$\omega_R^2 = v_g a N_p \left(\frac{1}{\tau_p} - 2\kappa\right) \tag{4.12}$$

$$\kappa = \frac{\left(1-r_2^2\right)r_3}{r_2}\frac{c}{2n_{eff}\left(L_{1a}+L_{1p}+L_r\right)} \tag{4.13}$$

$$\tau_{ext} = 2n_{eff}L_{2p}/c \tag{4.14}$$

where $\gamma$ is the usual definition for the damping factor. $v_g$, $a$, and $N_p$ are the average group velocity, differential gain and photon density respectively. $\tau_p$ is the photon lifetime in the main cavity. $L_r$ is the effective length of the pair of rings. $\tau_{ext}$ is the round-trip time in the external cavity. Figure 3.6 shows the measured and theoretical curves for the modulation response of the laser with and without the external cavity. The measurements were made using a lightwave component analyzer. As discussed earlier, since the external cavity mode spacing is not uniform, the value of $\tau_{ext}$ is frequency dependent. We observe this effect as non-uniform peak spacing in the measurement. The error, however, is marginal.

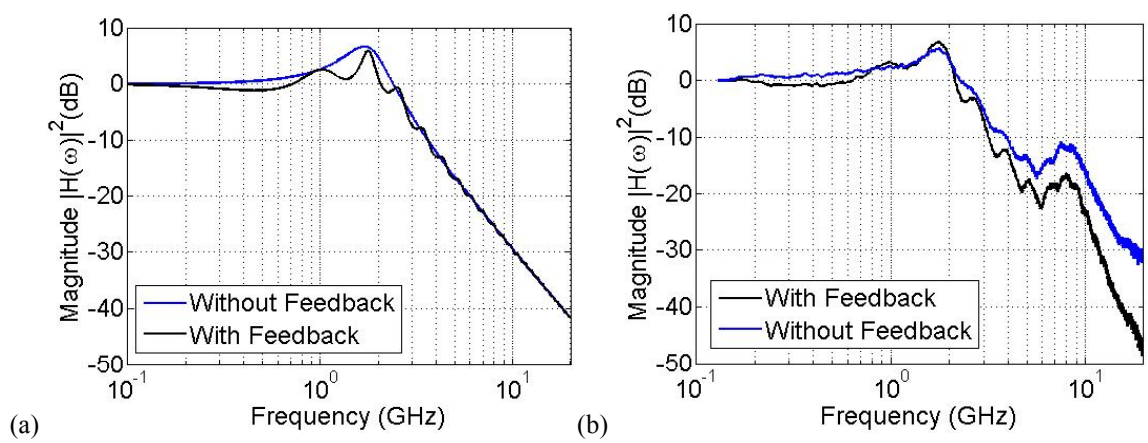


**Figure 3.6. (a) Theoretical and (b) measured curves for normalized modulation response of the laser with and without external cavity stabilization. The laser quiescent current was 70mA. The peaks around 8GHz in measured spectra are due to photon-photon resonance [37] that is not included in our simplified theoretical model.**

The peak at 8GHz is from the photon-photon resonance between the lasing mode and the neighboring mode of the main cavity lying within the ring resonator bandwidth. This phenomenon has successfully been modeled [37] and with careful tailoring of the laser parameters, could even be exploited to increase the 3dB modulation bandwidth of the laser.

The feedback from the external cavity helps suppress this peak or in other words improves the SMSR. The ripple in the measurement without feedback is due to residual reflections in the external cavity.

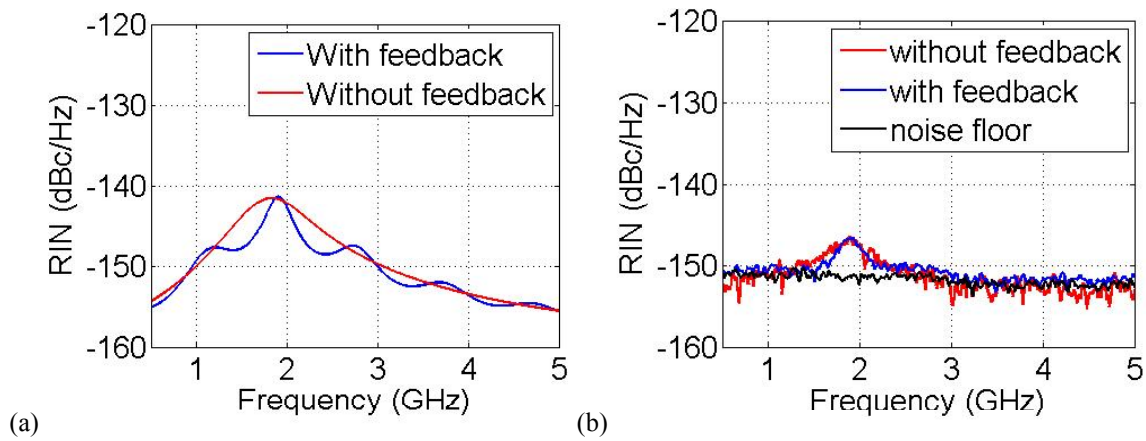


**Figure 3.7. (a) Theoretical and (b) Measured RIN spectrum with and without external cavity stabilization. RBW – 1MHz.**

The modulation transfer function for small signals shown in Eqn. (11) can be used to model the relative intensity noise from the laser [8]. We express RIN per unit bandwidth with the following equation

$$\frac{RIN}{\Delta f} = \frac{2h\nu}{P_0} + 16\pi\left(\Delta\nu_{ST}\right)\frac{\omega^2 + \left(1/\tau_{\Delta N}^2\right)}{\omega_R^4}\left|H\left(\omega\right)\right|^2 \tag{4.15}$$

where $P_0$, $\Delta\nu_{ST}$ and $\tau_{\Delta N}$ are the laser output power from the front mirror, Schawlow-Townes linewidth and the differential carrier lifetime respectively. A comment on detuning the wavelength from the ring resonance frequency to reduce linewidth, through the *B* term in Equation (4.8), was made earlier. Although beneficial in bringing the linewidth down, biasing on the slope couples frequency noise into amplitude noise [38] and this contribution is not included in Equation (4.15). However, we find this term is negligible for most frequencies. Figure 3.7 shows the RIN spectrum, both measurement and theory, for the cases with and without feedback. The measurements were limited by the noise floor of the

equipment and the modulation of the relaxation resonance peak in the case with feedback is barely visible, however, we do observe a narrowing effect of the peak at 1.8GHz. The RIN is below the noise floor (<-150 dBc/Hz) at all other frequencies, not shown in Figure 3.7, from 10MHz to 18GHz.

3. Linewidth and Wavelength Tuning Measurements

The laser operates in O-band and is tunable over a 54nm range from 1237.7nm to 1292.4nm with high side-mode suppression ratio exceeding 45dB across the entire tuning range (see Figure 3.8). They deliver >10mW of output power. The power is somewhat reduced by lower reflection (60%) from the back mirror, and can be further increased with a booster SOA outside the laser. The threshold current is around 30mA.

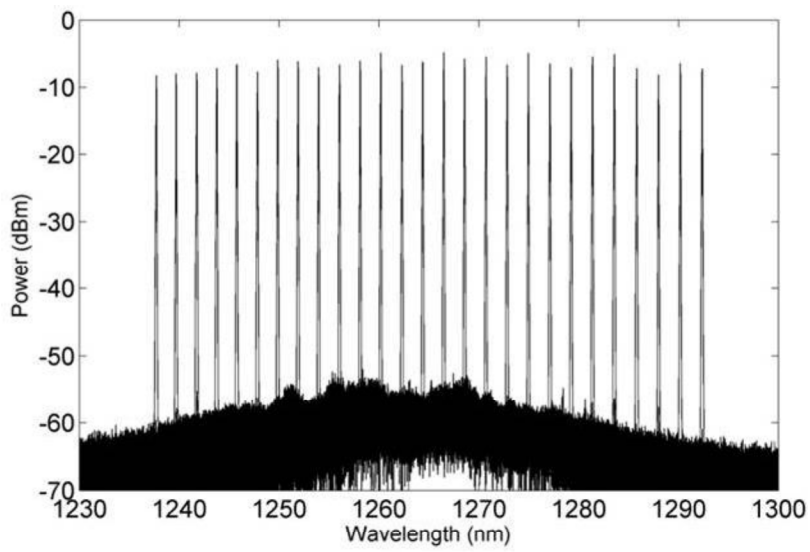


**Figure 3.8. Overlaid optical spectra from 27 different set points showing >54nm tuning range with SMSR > 45dB (RBW - 0.02 nm).**

The modulation response and relative intensity noise (RIN) of the laser show three distinct operation regimes: (1) external cavity turned off, (2) external cavity turned on while keeping the laser single-mode and (3) external cavity turned on when laser is operating in several of external-cavity modes.

As shown in Chapter 2, we can design a single very-long cavity laser utilizing the benefits of hybrid-silicon platform. Such an approach would lower the longitudinal confinement factor and would result in lower linewidth, but filtering a single-mode from such a cavity would be very challenging and the threshold current would increase. In short, we require a large FSR, high Q filter with very low loss to keep the laser single mode. In an external cavity design, one can make a standard single-mode tunable hybrid-silicon laser with low threshold (30 mA range) and provide feedback from integrated low-loss external cavity in order to reduce the linewidth.

The linewidth measurements were made by the delayed self-heterodyne method. The measurements were averaged 100 times on the electrical spectrum analyzer. With a stable commercial laser, we have verified that the setup can measure linewidths lower than 30kHz. To minimize external effects, in all measurements we have used an anti-reflection coated lensed fiber tip and two dual stage isolators, each having measured isolation greater than 50dB. In all linewidth measurements, unless specified otherwise, we have monitored that the laser is indeed single mode by measuring the spectrum with an optical spectrum analyzer and by measuring the laser beat signal with a 10GHz photodiode. The spacing of mode splitting due to the external cavity is around 0.97GHz, which is well within the bandwidth of the photodiode. For >12mA bias currents to the external SOA, the external cavity starts to lase and modes separated by ring FSR (~300GHz) and external cavity stable mode spacing (~2GHz) appear at the laser output.

The reflection from the external cavity is always present for all feedback SOA bias conditions, and it was practically impossible to measure the performance of the unperturbed laser. As we were unable to completely turn-off the external cavity, we have tried to estimate the linewidth of the unperturbed laser in two ways. First we measured the linewidth of a

similar laser design that has no external cavity. This laser has a higher back mirror reflectivity and has a modified silicon waveguide circuit with the same ring resonator geometries for wavelength tuning, however, the total cavity length and gain sections are similar. We estimate that higher back-mirror reflectivity reduces the linewidth, but at the same time the configuration of the microring resonators provided a lower $Q$ filter which would have increased the linewidth. Measured linewidths of these test structure lasers were 345kHz, 355kHz and 370kHz for three devices tested. The corresponding bias currents were 96mA, 74mA and 65mA.

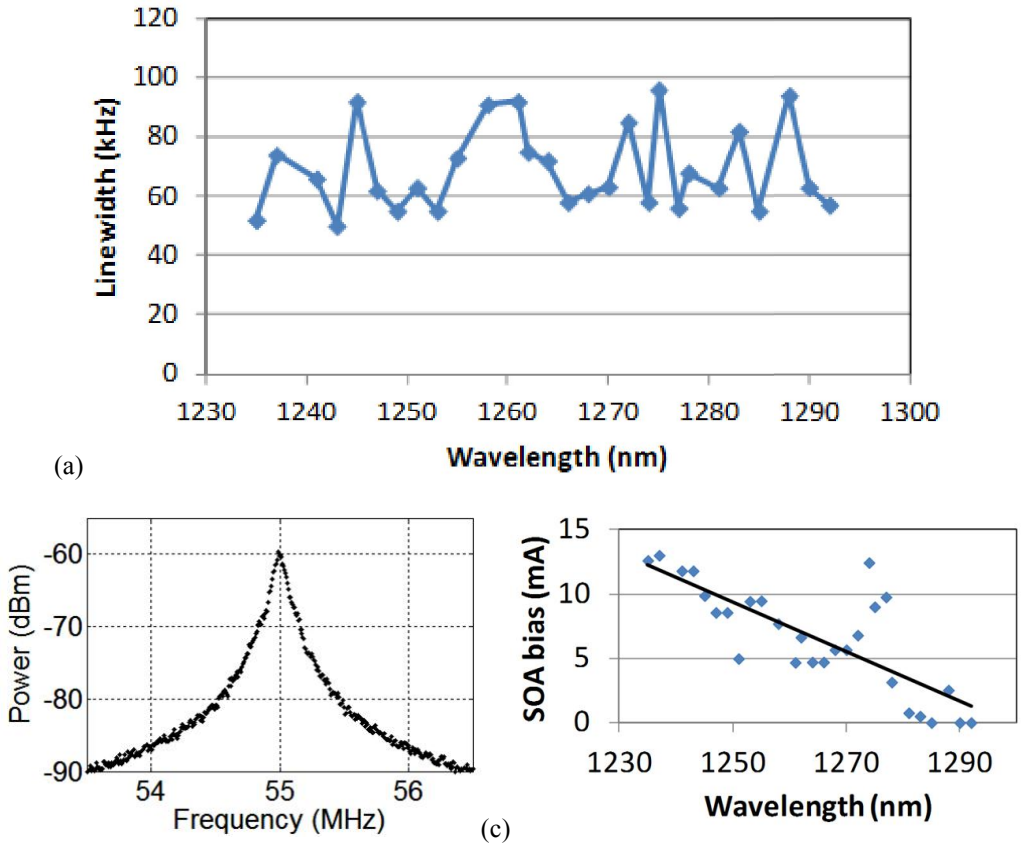


**Figure 3.9. (a) Best measured linewidth across the full tuning range. (b) Measured spectrum for the 50kHz result (RBW - 30kHz). (c) Bias currents (blue diamonds) applied to external SOA for linewidths measured and shown in (a) and a trend line (black).**

We also tried to measure the linewidth of the external-cavity laser at low laser bias currents (45mA) and with external SOA reverse biased at -3V where the influence of

external cavity is lowest. Linewidths with the external cavity turned off, and at 45mA laser bias were around 300kHz.

Finally we measured the linewidth of the laser with optimized feedback from the external cavity. We show these results in Figure 3.9. The linewidths were below 100kHz across the entire tuning range and the best single-mode linewidth is 50kHz. The quoted 3dB linewidths are calculated from -20dB points by assuming a Lorentzian lineshape [39]. The bias currents of laser corresponding to linewidth results shown are between 75 and 128mA, while the external SOA bias currents are between 0 and 13.06mA (see Figure 3.9 (c)). It is interesting to note that the external SOA bias currents for minimum linewidth tend to increase as the wavelength decreases. One explanation could be the wavelength dependence of the gain/loss in the external SOA. Below transparency, the absorption is higher on blue side of spectra, so higher bias currents are needed for same level of feedback. We were able to measure even lower linewidths (below 20kHz) at higher currents supplied to external SOA, but the laser was multimode with mode spacing determined by the external cavity length. In this case the RIN and frequency noise spectrums have peaks at this mode separation. This shows that the external cavity can provide even better performance if the filtering section is optimized. We also believe that the external SOA increased the noise in the feedback signal due to random spontaneous emission events.

The measurements were done on a temperature controlled stage with temperature set at 20ºC, but as the lasers were unpackaged and there was no temperature fluctuation feedback applied to the laser, we believe that the performance could be further improved if the lasers were packaged.

4. Summary and Future Work

We demonstrated a widely-tunable semiconductor laser with monolithically integrated 4cm long external cavity. We have shown tuning in excess of 54nm around the O-band as well as record linewidths <100kHz across the whole tuning range. Such narrow-linewidths allow for more advanced modulation formats in coherent transmission systems leading to better spectral efficiency. The excellent performance is enabled by leveraging the strengths of hybrid integration with low-loss silicon based waveguides. Further performance improvement can be realized by (1) packaging the devices to insulate them from external thermal influences, (2) introducing higher *Q* rings in the tuning section and (3) increasing the length of the external cavity using low propagation loss high aspect ratio $Si_3N_4$ waveguides [40].

In this work we have used an SOA to control the level of feedback, but were unable to completely shut-off the external cavity. The SOA, when driven below transparency, also increases the noise due to random spontaneous emission events potentially limiting the linewidth improvement from long external cavity. An alternative approach could use a variable optical attenuator (VOA).

### *B. Coupled Ring Resonator Mirror Based Tunable Laser*

In this section we will look at a tunable laser whose center wavelength is in the C-band. This laser is a good example of the linewidth improvement obtained from the optical negative effect discussed earlier. The laser design does not include long Si delay lines and hence it is very compact. This tunable laser uses two coupled ring resonator (CRR) mirrors in silicon on either side of the gain section to form the laser cavity. As a consequence we are able to demonstrate high optical output power (>15mW) and low linewidth (160kHz). We

organize this section as follows. First, the details of the laser design are covered followed by the linewidth and wavelength tuning measurement results. Next, we identify design errors in the fabricated CRR mirrors and suggest improvements. Finally we conclude with a brief summary of the results.

1. Laser Design and Fabrication

The advantage of using ring resonators, as opposed to Bragg gratings, in a tunable laser was first shown by Liu et al. [41]. The resonance enhancement of cavity length together with the Vernier effect can simultaneously provide a narrow linewidth and a wide tuning range. Traditional mirror designs using ring resonators usually have unwanted ports through which useful laser light is left untapped [42-46]. The advantage of using a CRR mirror design is that we avoid having a drop port bus waveguide to form the necessary filter shape and have a simple two output-port laser. One or more of the directional couplers in a CRR mirror can be made 100% to produce light in a single direction. The microscope image and a schematic of the fabricated laser are shown in Figure 3.10.

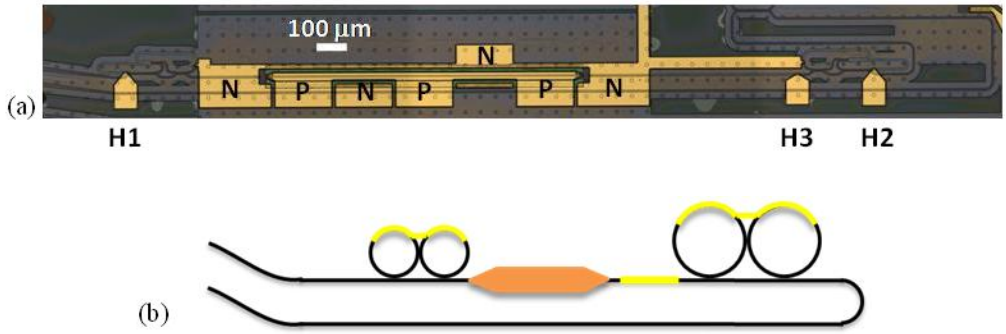


**Figure 3.10. (a) Microscope image of the hybrid silicon laser. (b) Schematic of the laser showing the design using CRR mirrors. Wavelength tuning is achieved by thermally tuning the waveguides (black lines) underneath the tuners (yellow lines). The orange section is the SOA for gain. P-laser anode, N-laser cathode, H1, H2, H3-positive terminal for each heater pads. The negative terminal of all heaters is shorted to laser cathode.**

The laser cavity is formed by two coupled ring resonator pairs on either side of the SOA. Each pair has a particular circumference that modulates the mirror loss spectrum to provide a

unique wavelength where the reflectivity is high. Tuning is achieved by heating each mirror to control the lasing wavelength. The circumferences chosen for each pair are 471μm and 513μm respectively. These numbers were limited by the minimum bend radius and the directional coupler lengths to achieve the different coupling coefficients. The Si waveguides were fully etched with a rectangular cross-section to minimize process variations in etch depth. The top silicon thickness of the SOI is 500nm and the waveguide width is 400nm to keep the bend radius small and for single mode operation. The waveguide width tapers out to 950nm under the SOA. The length of the SOA is 1040μm including the tapers. The active region comprises of 7 InGaAlAs quantum wells [47]. The output waveguides on both sides taper out to a waveguide width of 5μm and terminate at the facet at an angle of 7° to minimize reflections.

The design of the CRR mirror as a filter and as a reflector for lasers has been studied extensively by many authors [48-50]. The CRR mirror can provide various filter shapes with multiple resonances after each free spectral range (FSR). However, for a reflector in a tunable laser design we chose the coupling strengths that were required to achieve a single resonance peak. Figure 3.11 (a) shows a CRR mirror with labels for power coupling coefficient for the three couplers. In our design we have $\kappa 1=\kappa 2=2.25\%$ and $\kappa 3=36\%$ which relaxes the tolerance for the stronger coupler. The mirror loss is also better by 2dB at this design value compared to the minimum loss obtainable with symmetric coupler designs ($\kappa 1=\kappa 3\neq\kappa 2$). The suppression ratio of the interstitial peaks is >12dB which should be more than sufficient to suppress the longitudinal modes by >40dB. The reflection spectrum of each CRR mirror and the composite spectrum are shown in Figure 3.11 (b-c) for a waveguide loss of 5dB/cm. The output spectrum is not influenced by the relative distance between couplers within the CRR mirror.

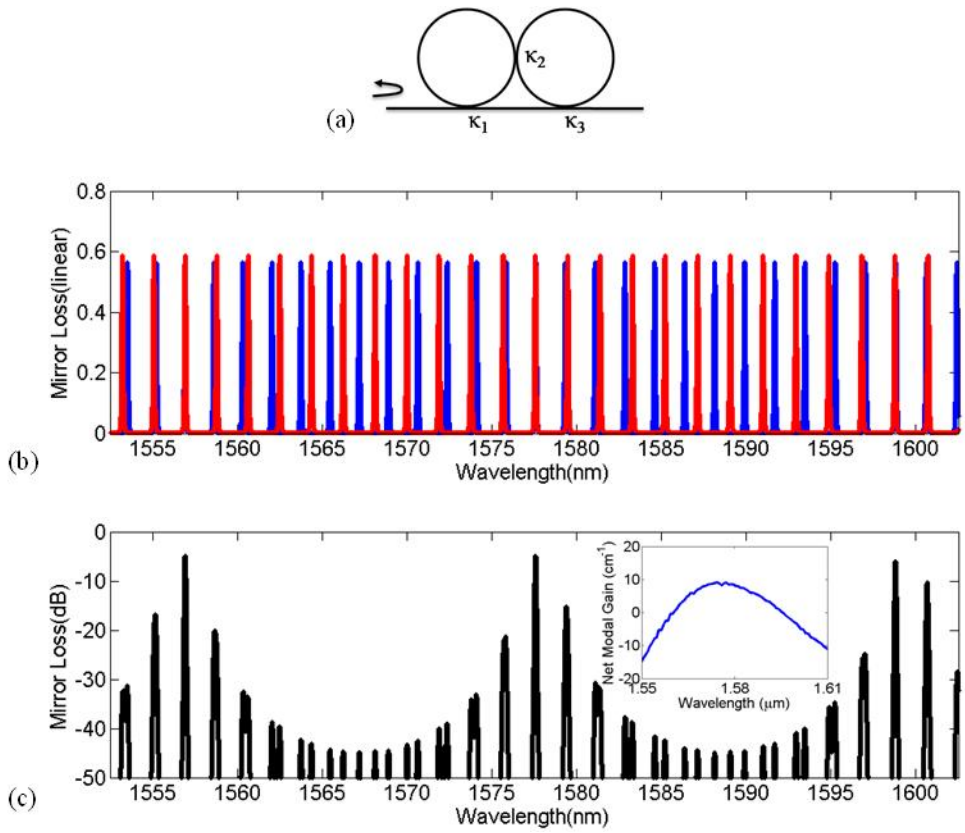


**Figure 3.11. (a) CRR mirror schematic. Reflection spectrum of each CRR mirror (a) and the composite mirror loss spectrum (b) of the laser cavity. Inset: Net modal gain ($\Gamma g$-$<\alpha_i>$) of a 1mm long SOA, where $\Gamma$ is the confinement factor, g is the material gain and $<\alpha_i>$ is the internal loss per unit length.**

2. Measurement Results

The laser was measured on a temperature controlled stage set at 20°C. The threshold current is 56mA. The light-current-voltage (L-I-V) curve from using an integrating sphere and collecting light outputs from both sides is shown in Figure 3.12. The kinks in the curve are due to mode hoping from the changing cavity phase with input current. The output light is coupled into a 2μm spot-size lensed fiber and used to measure the optical spectrum and linewidth. The wavelength tuning is achieved using three thermal tuners: one each for tuning the CRR mirrors and one for tuning the longitudinal cavity modes.

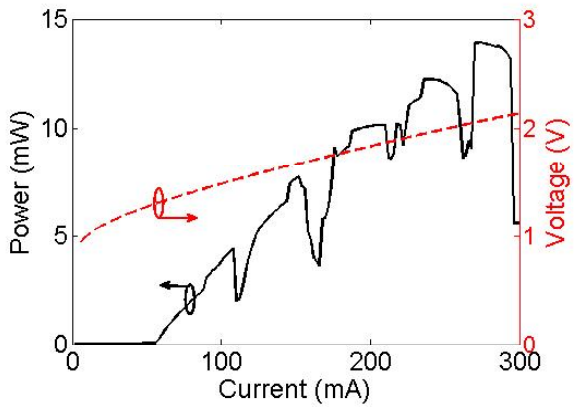


**Figure 3.12. L-I-V curve for the tunable laser diode at 20°C.**

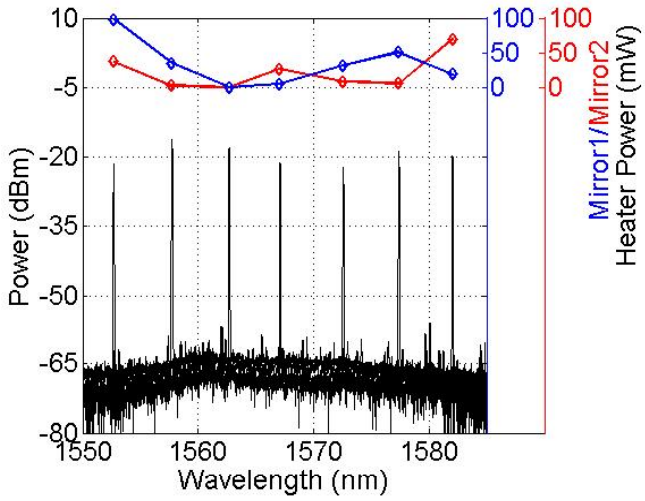


**Figure 3.13. Coarse tuning of the laser between 1553nm and 1582nm.**

Figure 3.13 shows the coarse tuning of the laser along with the heater powers on each mirror. The side-mode suppression ratio is >40dB over the full span. The wavelength of the laser did not trend well with the heaters' input power and we discuss a few possible reasons for this in the following sub-section. The tuning efficiency of the heater was measured by reverse biasing the SOA and monitoring the photocurrent while sweeping the wavelength of input light into the laser. By recording the change in wavelength of the transmission spectrum with heater power, we calculate the required tuning power for one FSR shift as 91mW and 103mW for the 471μm and 513μm long rings, respectively. The linewidth of the

laser was measured using a delayed self-heterodyne technique using 20km of single mode large effective area fiber (SM-LEAF). The minimum linewidth measurable with this setup is ~10kHz. The output power of the laser is amplified using an L-band erbium doped fiber amplifier (EDFA) before sending it to the linewidth measurement setup. The linewidth measured at an input current of 195mA and no bias on the heaters is 160kHz, as shown in Figure 3.14. The wavelength at this current is 1576.6nm. The current source was battery powered while measuring the linewidth. The wavelength shift with temperature was 0.106nm/°C in the range of 20°C to 50°C.

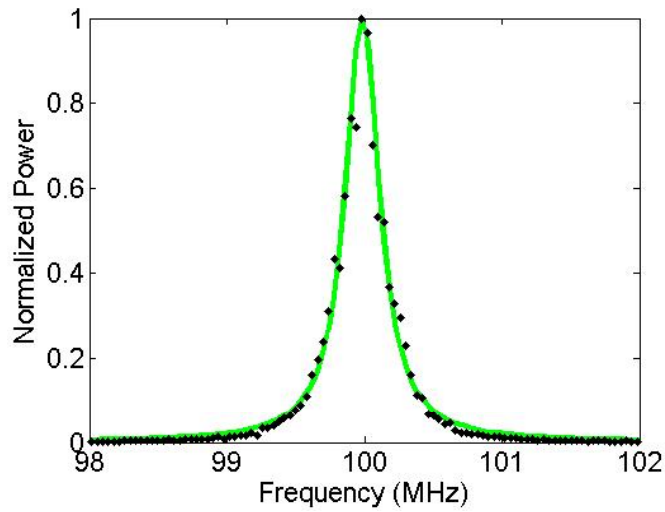


**Figure 3.14. Self heterodyne linewidth measurement (black dots) and the corresponding Lorentzian fit (green line). The resolution bandwidth is 10kHz.**

3. Discussion

One key feature of ring resonator based laser designs is the effective cavity length enhancement near resonance wavelength. As the wavelength approaches the resonance wavelength, the laser cavity appears longer due to increased photon lifetime in the ring. This is evident in the spacing of the longitudinal modes of the lasing cavity. Figure 3.15 shows simulation results for the effective cavity length of the laser and the non uniform spacing of

the longitudinal modes. The effective length was observed to be increased by roughly a factor of three. This is due to the large reduction in group velocity at resonance. The locations of the longitudinal modes satisfy the equation,

$$2\beta_a L_a + 2\beta_p L_p + \angle M_1 + \angle M_2 = 2N\pi \tag{4.16}$$

where $\beta_a$, $\beta_p$ and $L_a$, $L_p$ are the propagation constants and the lengths of the active and passive sections respectively. $\angle M_1, \angle M_2$ are the phases acquired by the reflected electric field at the two mirrors. N is an integer. Therefore, one has to be cautious of increasing the cavity Q by making the couplers weak as this might result in multiple longitudinal modes within a resonance peak of the ring to start lasing.

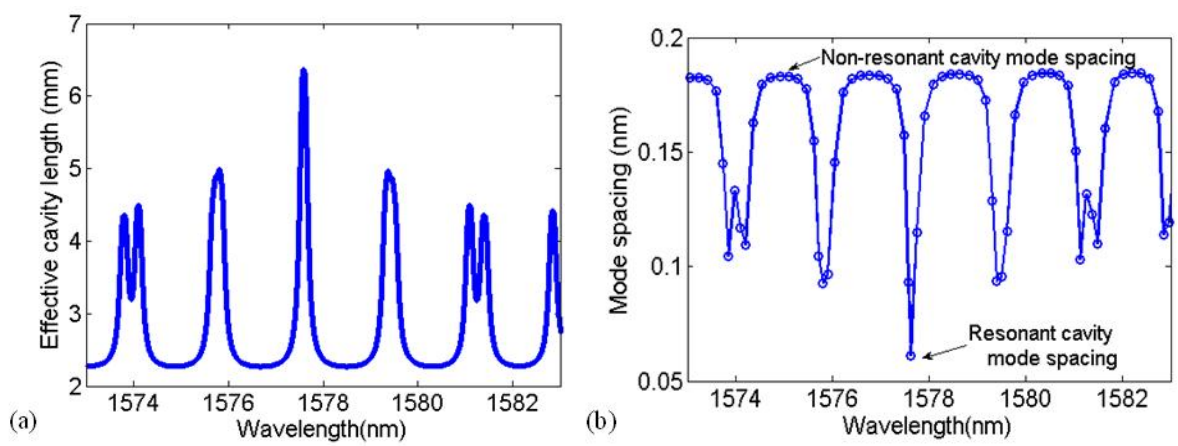


**Figure 3.15. Simulation results for (a) effective cavity length as a function of wavelength showing almost tripling of length at resonance and (b) location of each longitudinal mode and the spacing from its nearest neighbor, reduced by one-third at resonance.**

An important observation was made while measuring the linewidth for different SOA bias current. The linewidth decreased from ~5MHz down to ~200kHz for a change in current of ~25mA and the lowest linewidth occurs just before a mode-hop event. The output power at best increases by a factor of two and cannot explain the factor of 25 in linewidth reduction. Under close inspection, we observe that the change in wavelength with current due to heating is -330MHz/mA due to rising active region temperature. Over 25mA this

corresponds to a lasing frequency change of ~8GHz. The spacing between longitudinal modes near resonance is also ~8GHz measured using a high resolution optical spectrum analyzer (OSA). This confirms the reason for periodic mode hopping every 25-30mA and the reduced FSR due to resonant length enhancement. Additionally, it also points to the fact that the lowest linewidth occurs on the long wavelength side of the rings resonance. This can be explained using the optical negative feedback effect that occurs when the mirror loss has a steep dependence on wavelength. This effect is the likely reason for the significant decrease (>10x) in linewidth in our lasers and also in other laser designs using ring resonators observed by other research groups [42, 43, 51].

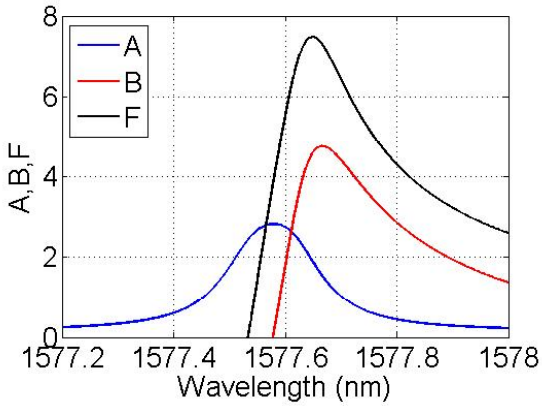


**Figure 3.16. Simulated values for parameters A, B, F around resonance wavelength (1577.58nm) showing large reduction in linewidth ($\propto 1/F^2$) on the long wavelength side of the resonance.**

The feedback effect is very fast and has a potential for broad band frequency noise reduction. Although detuning the lasing wavelength off-resonance reduces the contribution to linewidth reduction from cavity length enhancement, the improvement from the negative feedback mechanism is much larger and thus provides an overall reduction in linewidth. This could be an important phenomenon that could be exploited in the future for designing integrated narrow linewidth lasers. This was included in the theory formulated by G. Agrawal et al. [35], in the form of a reduction factor 'B' associated with the derivative of

mirror loss with frequency without the physical explanation. Figure 3.16 shows the simulated values for A, B, and F for this laser (see Section A, Equations (4.7), (4.8), and (4.9), for definition of A, B, and F). The linewidth of the laser with the resonant mirrors is given by $\Delta\nu_{ST}/F^2$ where $\Delta\nu_{ST}$ is the modified Schawlow-Townes linewidth including the linewidth enhancement factor. The further advantage of this approach is that, there is no appreciable increase in RIN due to conversion of frequency noise to amplitude noise.

**Figure 3.17. Thermal image of the heater when supplied with 30mW(4V), showing non-uniform heating at the hairpin bend in the center due to crosstalk.**

A second important note is that the rings for a single mirror are resonantly coupled to each other. Since the couplers are all not identical, the effective ring circumferences are different even if the physical cavity lengths are made the same. This is due to the difference in absolute phase shift acquired along the different coupler lengths. This leads to a resonance splitting and misaligned resonances in a Vernier cavity [52]. Therefore, it is important to have individual tuners to compensate for this error. For full versatile control, the number of tuners required for this laser design is five, two for each mirror and one to tune the longitudinal mode of the laser cavity within the resonance peak, each capable of tuning a full $2\pi$. The tuning map of our laser was also affected by non-uniform heating of the waveguides in each ring of the CRR mirror. Figure 3.17 shows the thermal image of the tuners, taken with a commercial thermoreflectance microscope. The thermal map shows non-uniform

heating near the hairpin bends of the tuners. The non-uniform heating and lack of individual tuners on the rings are the reasons for the unpredictable tuning map in our fabricated lasers.

4. Summary

In conclusion we have demonstrated a tunable laser on the heterogeneous silicon platform using coupled ring resonator mirrors. The CRR mirror design does not use a drop port waveguide and preserves the laser power to just two ports and can be reduced to one port if necessary. The resonant mirrors also allow the reduction of optical linewidth using an optical negative feedback mechanism and can be a useful feature for designing future narrow linewidth tunable lasers. The laser demonstrated has an output power >15mW and a linewidth of 160kHz. The coarse tuning range is 29nm and the side-mode suppression ratio is >40dB over the full tuning range. A more predictable tuning map is possible by designing individual heaters on each ring of the CRR mirror and by designing the ring lengths so as to avoid the resonance splitting and spacing the heaters appropriately to avoid thermal cross talk.

### *C. Conclusions*

We demonstrate two all-optical noise reduction techniques for tunable lasers, viz. on-chip delayed optical feedback and negative optical feedback using resonant mirror design. Both the techniques are wavelength independent effects i.e. linewidth reduction is possible in the entire tuning range. At optimum bias conditions, they do not influence the tuning capacity or the SMSR of the laser and use minimal electrical power. They do require precise control on the bias currents and voltages. The hybrid silicon platform is the enabling technology to realize these design concepts on a single chip. This technology certainly holds great promise in advancing the tunable laser research.

# 4. Reliability of Hybrid Silicon DFB Lasers

## *A. Introduction*

Silicon is an inefficient light emitter, so approaches to epitaxially grow III-V materials on silicon wafers have been pursued for over thirty years [53]. However, the reliability of these devices have been poor due to the threading dislocations and stacking faults resulting from the lattice mismatch, difference in coefficient of thermal expansion, and the problems of growing polar materials on non-polar substrates [54]. Wafer bonding III-V materials to silicon results in high quality III-V layers without threading dislocations or stacking faults, but with a thin oxide layer at the interface between the III-V layer and silicon layer [55]. This approach has resulted in low threshold, high power lasers [56], high speed modulators [57] and high efficiency photodetectors [58] and integrated CWDM transmitters [59].

Since lasers epitaxially grown on silicon have shown poor reliability in the past, it is important to investigate the reliability of hybrid silicon lasers before it is adapted into a production line. The first reported work [60] on reliability of optical devices made from growing InP on Si included strained superlattice layers to reduce stress and interface defects. Therefore, this work also investigates whether superlattices between the lasing region and the silicon/III-V interface affect the laser and photodetector reliability. At present the typical reliability requirement for optical transmission systems is a median time to failure (MTTF) in excess of 10 million hours (>1000yrs) under full rated power [61]. It is customary to obtain data from accelerated aging tests where bias current and junction temperature exceed those during normal operation, to shorten time to device failure. We restrict ourselves to hybrid Si DFB lasers with AlGaInAs MQW active region only. Section B of this chapter

describes the experiment in detail following which we analyze the results in Section C. Section D includes our conclusions and future work in this area.

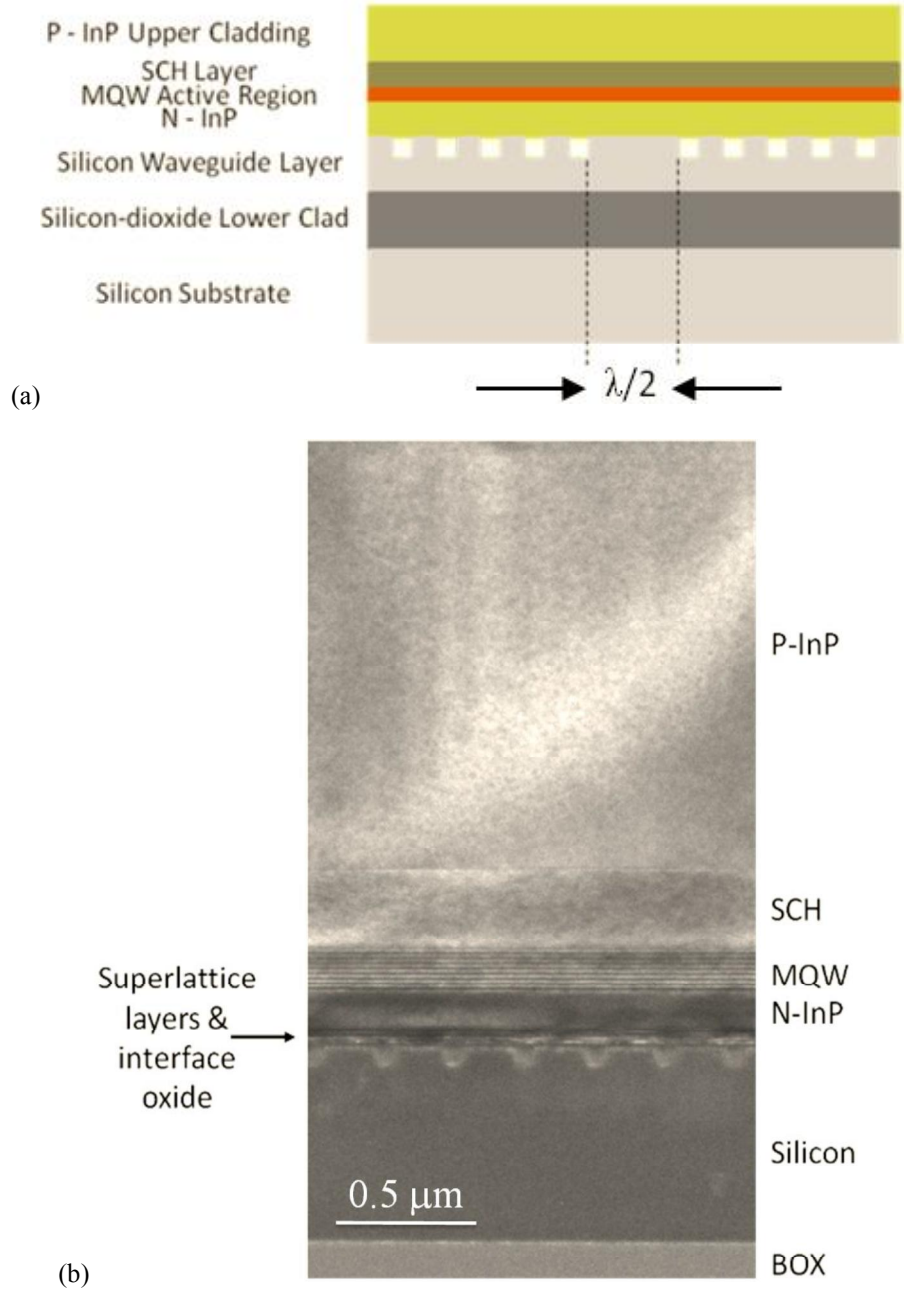


**Figure 4.1. (a), (b) Schematic diagram and TEM image of the longitudinal cross-section of a symmetric quarter-wave shifted hybrid Si DFB laser [62] © 2013 IEEE.**

### *B. Experiment*

Figure 4.1 shows the schematic and a TEM image of the longitudinal cross section of a quarter wave shifted hybrid Si DFB laser [56]. Ten pieces were cleaved off from a silicon-on-insulator (SOI) wafer and patterned with Si waveguides. One of the three epitaxial structures (A, B or C), shown in Table 4.1, was transferred onto the pre-patterned pieces and processed further to make a total of 10 dies with 300 laser diodes each. The dimensions of a single die are 8 mm×8 mm. Each laser diode was integrated with an on-chip photodetector on either side to monitor output power. The work by Sugo et al. [60] showed a laser diode made from growing InP on Si including strained superlattice interface layers to reduce stress and interface defects. They achieved stable laser operation up to 2000hrs. Thus, to prevent defects originating from the bonded interface, due to thermal expansion mismatch of Si and III-V, from propagating to the active region, structures A and B included unstrained and strained (-1% well, 1% barrier) superlattice layers, respectively. Structure C was a control design with a thicker n-InP layer to maintain similar hybrid optical mode profile.

Preliminary experiments [63] on the quality of transferred epitaxial layers for the three structures showed a similar conclusion as reported in Reference [60]. The yield was also significantly higher for the structures that included superlattice layers (99% for Structure A, 93% for Structure B vs. 60% for Structure C). The yield percentage includes only quarter-wave shifted DFB lasers of the same length (360μm). The metal stack for p and n contacts were Pd/Ti/Pd/Au and Ni/Ge/Au/Ni/Au, respectively.

The threshold currents extracted from Light-Current (L-I) curves for 550 devices before aging are shown in Figure 4.2 (a). Similar threshold distribution is observed for the three structures. The measurements were done on-chip, using pin-probes, at 25°C in continuous-wave (CW) mode. The simulated band diagram for the three structures can be seen in Figure

4.2 (b)-(d). The representative L-I curves, from 50 DFB laser diodes of structure A, in Figure 4.2 (e) shows the uniform distribution of threshold current and slope efficiency in these devices.

The waveguide facets were polished and AR coated. A 7° angle for the output Si waveguide was chosen to minimize reflections. Fourteen devices from each epitaxial structure were singulated. The singulated dies were Indium bonded on ceramic sub-mounts for good thermal contact. The Light-Current (L-I) curves were re-measured after packaging and no degradation was found. In order to collect light from a surface normal detector the dies are rotated on the sub-mount at a 67° angle from the edge of the ceramic using the flip-chip bonder. A pair of DFB laser diodes along with on-chip photodetectors was wire-bonded to the pads on the sub-mount. A thermistor is also mounted to monitor the temperature during aging. A scanning electron microscope (SEM) image of a complete carrier is shown in Figure 4.3.

**TABLE 4.1**
**Epitaxial layer structure of the three wafers used in this work.**

| Thickness (nm) | Layer/ Doping ($cm^{-3}$) | Structure A | Structure B | Structure C |
|---|---|---|---|---|
| 100 | P-contact/ $1\times10^{19}$ | P - $In_{0.53}Ga_{0.47}As$ | P - $In_{0.53}Ga_{0.47}As$ | P - $In_{0.53}Ga_{0.47}As$ |
| 1500 | Cladding/ $1\times10^{18}$ | P - InP | P - InP | P - InP |
| 250 | SCH/ $1\times10^{17}$ | $In_{0.528}Al_{0.132}Ga_{0.34}As$ | $In_{0.528}Al_{0.132}Ga_{0.34}As$ | $In_{0.528}Al_{0.132}Ga_{0.34}As$ |
| 7<br>10 | MQW/ u.i.d | $In_{0.653}Al_{0.055}Ga_{0.292}As$ (×8)<br>$In_{0.45}Al_{0.089}Ga_{0.461}As$ (×9) | $In_{0.653}Al_{0.055}Ga_{0.292}As$ (×8)<br>$In_{0.45}Al_{0.089}Ga_{0.461}As$ (×9) | $In_{0.653}Al_{0.055}Ga_{0.292}As$ (×8)<br>$In_{0.45}Al_{0.089}Ga_{0.461}As$ (×9) |
| | N-contact | N – InP (110 nm/$1\times10^{18}$ $cm^{-3}$) | N – InP (110 nm/$2\times10^{18}$ $cm^{-3}$) | N – InP (140 nm/$2\times10^{18}$ $cm^{-3}$) |
| 7.5<br>7.5 | Superlattice/ $1\times10^{18}$ | $In_{0.85}Ga_{0.15}As_{0.327}P_{0.673}$ (×2)<br>InP (×2) | $In_{0.794}Ga_{0.206}As_{0.145}P_{0.855}$ (×3)<br>InP (×3) | |
| 10 | Bonding/ $1\times10^{18}$ | InP | InP | InP |

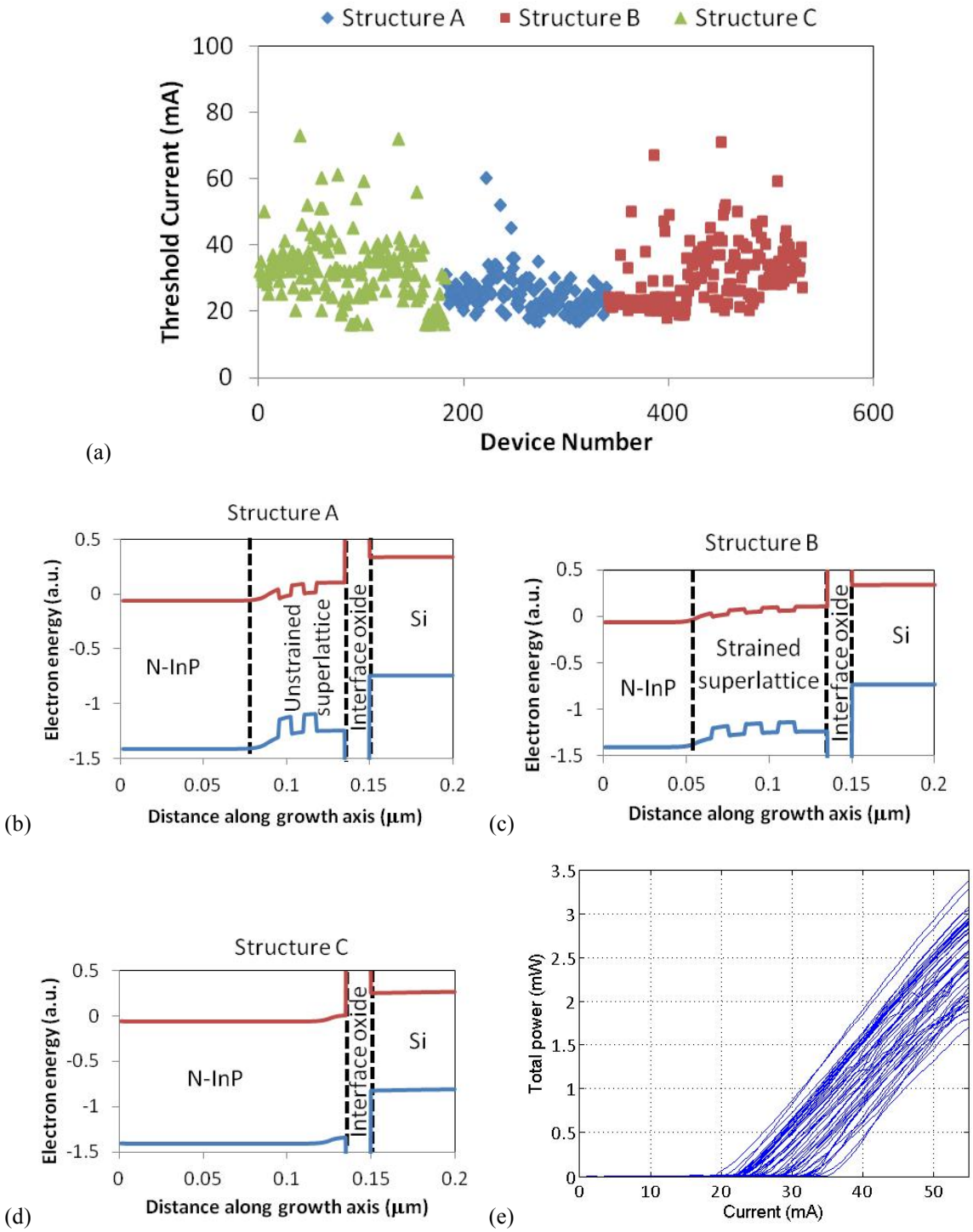


**Figure 4.2. (a) Threshold current of DFB lasers with three different epitaxial layer structures before aging tests, (b)-(d) The simulated conduction band (red) and valence band (blue) diagram for the three structures, (e) Representative Light-Current (L-I) curves for 50 DFB laser diodes of structure A before aging [62] © 2013 IEEE.**

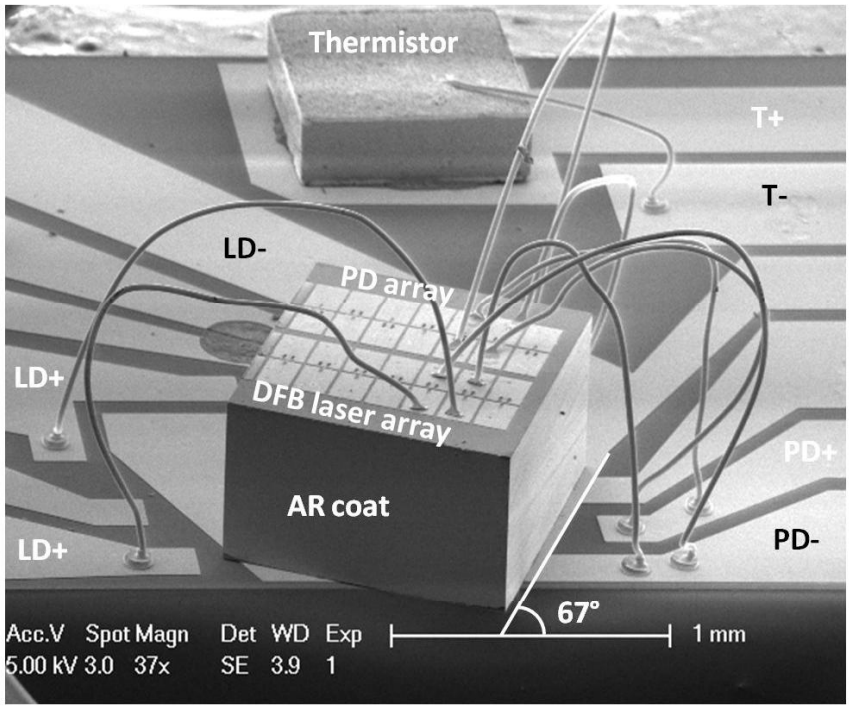


**Figure 4.3. Scanning electron microscope (SEM) image of a complete carrier used in the aging test [62] © 2013 IEEE.**

### *C. Results and Discussion*

The aging tests were done at five different temperatures, viz. 25°C, 50°C, 60°C, 70°C and 85°C while the devices were biased at 80 (5.56) or 100 (6.94) mA (kA/cm$^2$). All the devices had a 4μm current channel defined using proton implantation on a 14μm wide mesa. The Si waveguide width is 1.5μm. Room temperature (25°C) Light-Current (L-I) curves were taken at certain intervals during the aging test. The threshold current during the period of aging, at different bias conditions and temperature is shown in Figure 4.4 (a)-(f). Regardless of the design and aging condition, most devices showed no significant degradation in this time period. The threshold current of two devices degraded with time at 70°C. As suggested in an earlier work [61], a sub-linear fit is used to evaluate the median time to failure (MTTF). With a criterion for failure as 50% increase in threshold, we estimate the lifetime of devices using Eqn. 2.1 and 2.2.

$$I_{th}/I_{th}(0) = 1 + at^m \tag{2.1}$$

$$MTTF = \left(\frac{0.5}{a}\right)^{1/m} \tag{2.2}$$

where $I_{th}$ and $t$ are threshold current and aging time respectively. The values for fitting parameters $a$ and $m$, for the data shown in Figure 4.4 (g)-(h) are as follows. Structure A: a=0.004678, m=0.43 and Structure B: a=0.002215, m=0.51. This corresponds to MTTF values, at 70°C, of 48533hrs and 39827hrs for structures A and B, respectively. Due to failures there were no degradation data for structure C available for fitting.

We also investigated the thermal aging of hybrid silicon photodetectors [58]. The dark current of on-chip photodetectors, biased at -4V, before and after aging tests, are shown in Figure 4.5 for comparison. There is an increase in dark current for structures A and B, however, they are still significantly lower than the values for structure C. This shows that superlattice structures immensely help in retarding defects from reaching the active layer, apart from increasing the yield and quality of hybrid Si lasers. The lowest dark current, after aging tests, continues to be observed mainly in the strained superlattice layer case. A statistical interpretation is not accurate because of a small number of data points in each case after aging.

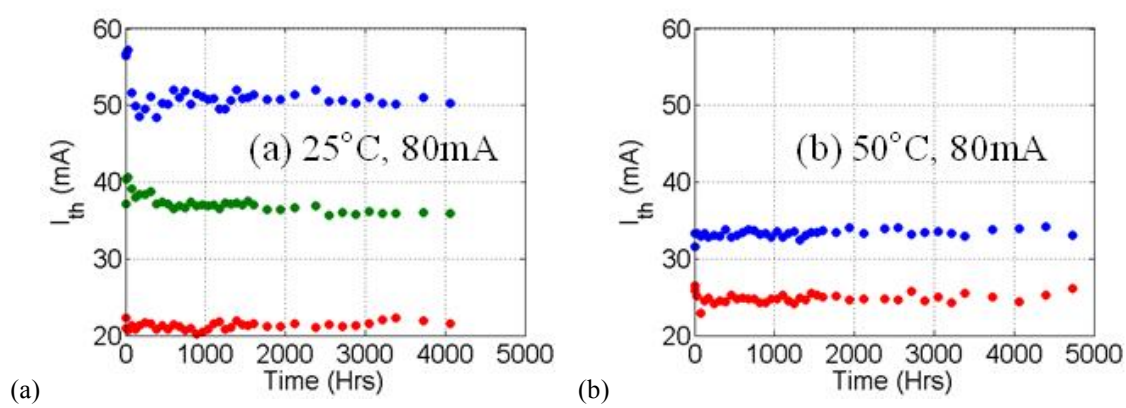

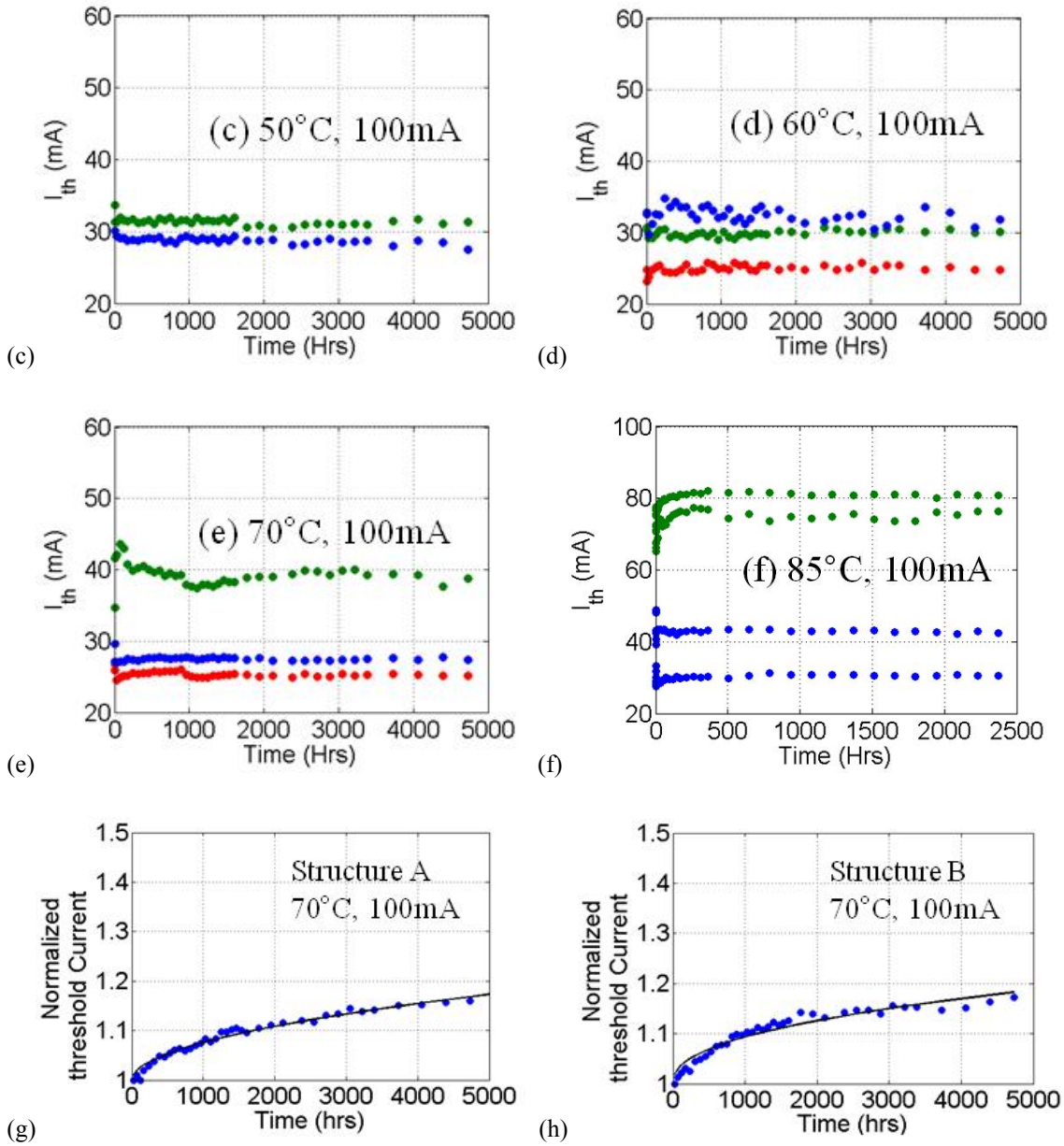


**Figure 4.4. (a)-(f) Threshold current of devices at various aging conditions - Structure A (blue), Structure B (red) and Structure C (green). (g)-(h) Degradation data for two structures along with the sub-linear fit (black) [62] © 2013 IEEE.**

A device that failed after 1000hrs of aging at 70°C under 7kA/cm$^2$ of injection current was tested for identifying the failure mechanism. A transmission electron microscope (TEM) image of a 15μm long portion of the laser cavity section in the region of peak internal power is shown in Figure 4.6. The contours in Figure 4.6 (b) are due to bending and thickness fluctuations across the sample. The entire cross-section was carefully observed for defects in

the active region. Although we were able to locate a few edge dislocations at the interface between InP and Si, there were no defects in the multiple quantum well (MQW) active region found.

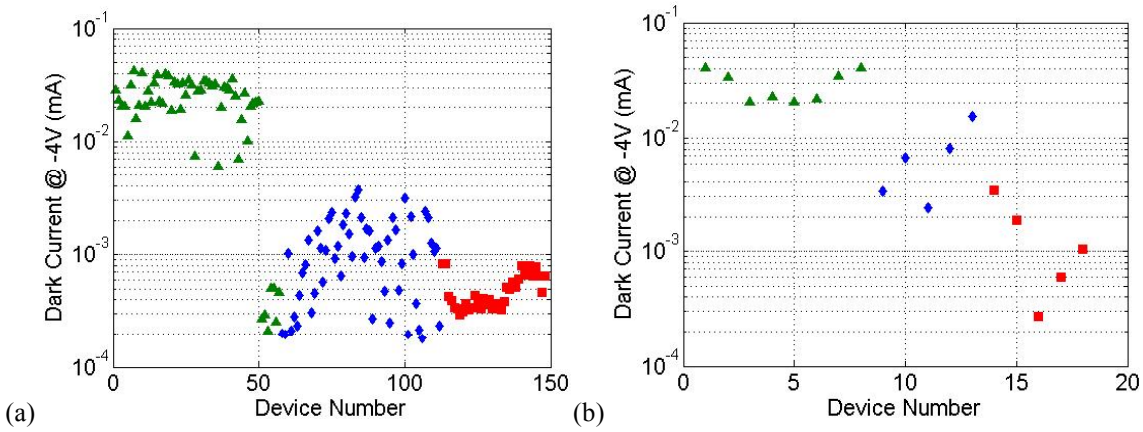


**Figure 4.5. Dark current (-4V) of photodetectors fabricated on structures A (blue), B(red) and C(green), (a) before aging test and (b) after aging test [62] © 2013 IEEE.**

The thickness of the lamella was 387nm across 15μm which suggest that the dislocation density in the active region is lower than $1/(387\times10^{-7}\times15\times10^{-4}) = 1.7\times10^{7}$ $cm^{-2}$. This suggests that dislocations are not a possible failure mechanism. Since the activation energy of the failure mode is unknown at present we believe that contact degradation and dielectric failure are the next big suspects, as the contacts were optimized for performance and not long term reliability. Additionally, it is unclear if this is an isolated issue as there were devices that did not fail or degrade at the same temperature and bias condition, in which case these devices would be screened out before deployment.

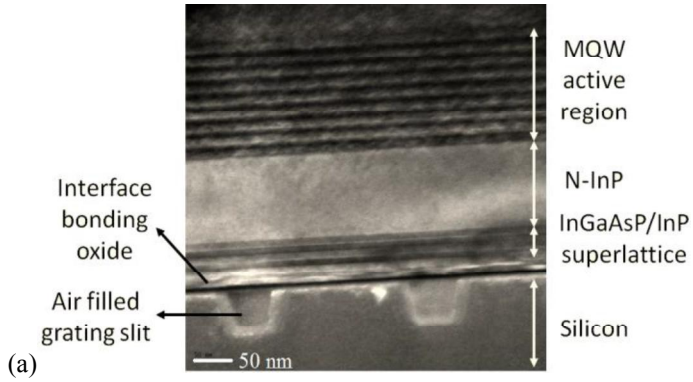

(b)
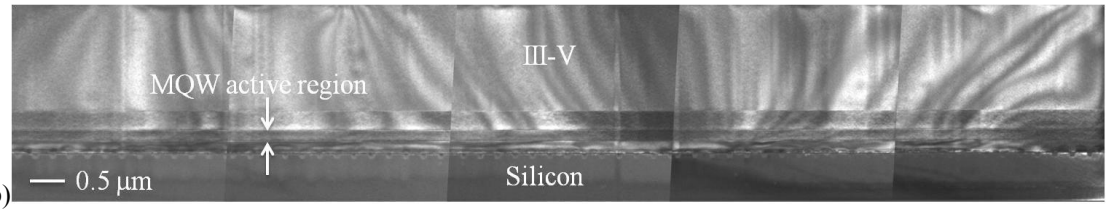


**Figure 4.6. (a) Close-up TEM image of a failed device made using an epitaxial wafer with structure A showing no defects in the active layer. (b) A stitched image of a 15μm long longitudinal cross-section of the same laser diode with no defects in the active layer [62] © 2013 IEEE.**

### *D. Conclusion*

The main modes of degradation in laser diode sources are: dislocations that affect the crystallinity of MQW layers in the active region, metal diffusion and alloy reaction that affect the electrode, solder instability (reaction and migration) that affect the bonding parts or dielectric failure. These modes are enhanced by current injection and high temperature operations. Facet damage is not very important in the context of PICs with on-chip light sources. We have conducted aging tests on DFB laser diodes and photodetectors on the hybrid Si platform and conclude that dislocations are not the dominant failure mechanism. The laser diodes with a superlattice showed no significant degradation in threshold current after 5000hrs of aging at 70°C and 2500hrs at 85°C. 50% degradation in threshold current of some diodes at 70°C is estimated to take ~40000hrs. Most devices did not show any form of degradation, and there was not a significant difference in lasers with or without strain in the superlattice and the control sample, in terms of aging. We did observe a difference in leakage current of photodiodes, indicating that strained superlattices give the minimum leakage current. This suggests that the platform is suitable for making reliable active optical devices, including lasers, modulators and photodetectors on silicon.

## 5. Hybrid Mode Locking

The goal of this section is to present results that show the advantage of harmonically locking long cavity lasers using optical intra-cavity filters rather than hybrid-locking using an external microwave source. In other words, correlating photons among the multiple pulses inside a harmonically mode-locked laser diode with saturable absorbers is best done optically. We fabricated mode-locked lasers with long cavities identical to those shown in Chapter 2, Section B, but without the intra-cavity filter.

We begin by investigating the passive mode-locking behavior of a 3.967cm long mode-locked laser diode (2GHz cavity). The output light (CCW) is fed into a high speed u2t photodetector (50GHz bandwidth) followed by an RF amplifier (18dB gain, 25GHz bandwidth) and an electrical spectrum analyzer (ESA). The data is recorded for different SOA currents and absorber voltages. The plot of RF power at the first five harmonics is shown in Figure 5.1 (a-e). Figure 5.1 (f) shows a weighted sum of the RF powers at these five harmonics, where the weights are chosen to compensate for the envelope of the power spectral density of a Gaussian pulse. This plot helps to identify the region of device operation where all the harmonics are maximized, i.e. the device is well mode-locked. As a guide to the eye, a region M1 is marked on Figure 5.1 (f) to show the region of interest.

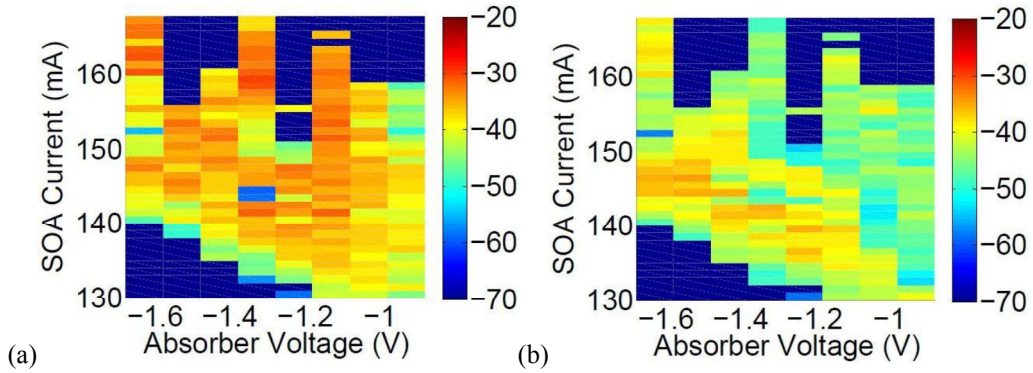

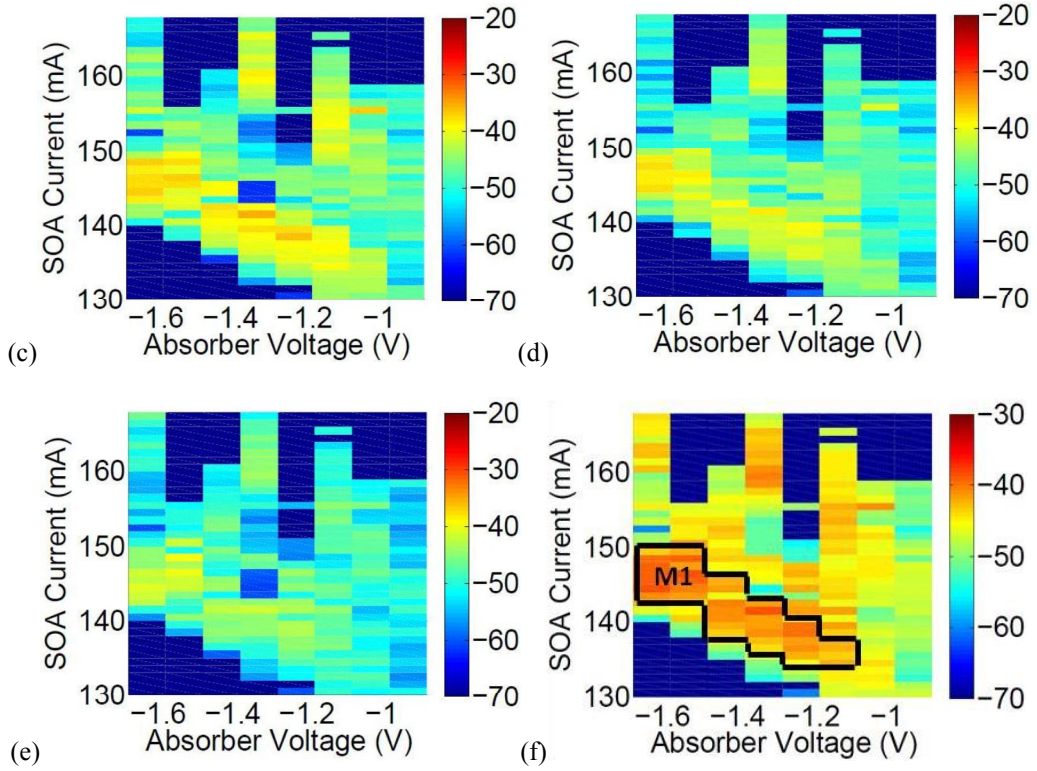


**Figure 5.1. (a-e) RF power as a function of SOA current and SA voltage at the first five harmonics; fundamental (1.99GHz), 2nd (3.98GHz), 3rd (5.97GHz), 4th (7.96GHz) and 5th (9.95GHz) respectively. (f) Weighted sum of RF powers at the first five harmonics. Resolution bandwidth (RBW) - 3MHz [23] © 2014 IEEE.**

Figure 5.2 shows data from a high resolution optical spectrum analyzer (RBW - 20MHz), an autocorrelator and an electrical spectrum analyzer all at 140mA of SOA current and -1.3V on the absorber. This bias point was chosen based on Figure 5.1 (f). At this stage, the absorber has no RF drive and the plots indicate passive mode-locking. We used an EDFA after the chip output to measure the pulses with the autocorrelator. The time-bandwidth product (TBP) is 1.5, indicating that the pulse is chirped. The electrical spectrum shows equidistant peaks at multiples of 1.99GHz. The RF linewidth (3dB) is roughly 14kHz evaluated using a Voigt fit to the spectral data (Figure 5.2 (d)). A Voigt fit is chosen because the RF amplifier introduces Gaussian noise to the spectral data.

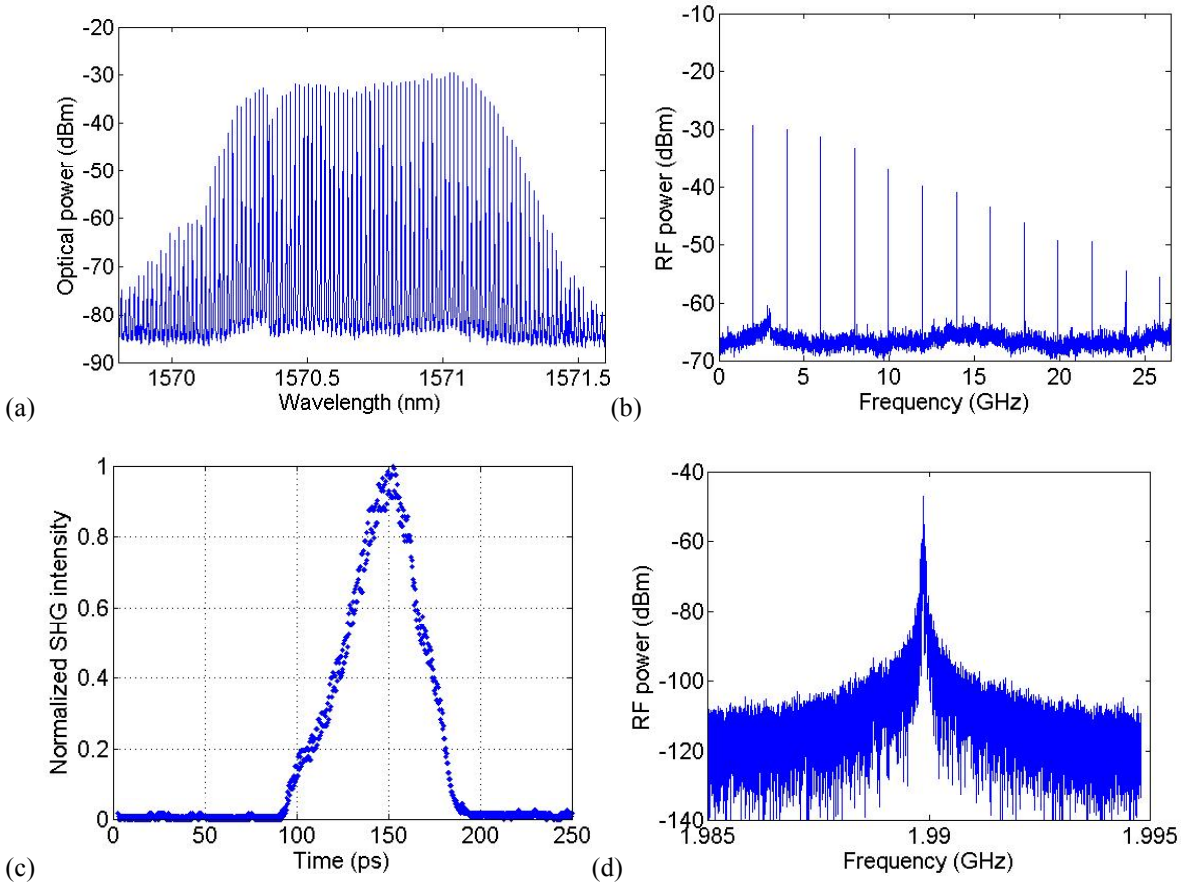


**Figure 5.2. Optical spectrum (a), autocorrelator trace (b), electrical spectrum – wide span (c) and close-in (d). The RBW in (c) and (d) are 3MHz and 1kHz respectively. The SOA current is 140mA and the SA voltage is -1.3V [23] © 2014 IEEE.**

We continue to hybrid mode-lock this laser using an external signal generator. The results from hybrid mode-locking at 1.99GHz (fundamental) are shown in Figure 5.3. The pulse train data is obtained from a sampling oscilloscope (bandwidth 70GHz) along with a u2t photodetector with a bandwidth of 50GHz. The frequency of the generator is swept around the passive mode-locking frequency and an optimum operating frequency was identified at a point where the ESA showed periodic peaks with no spurs. Hybrid mode-locking at 1.99GHz shows fewer lines in the optical spectrum and a larger pulsewidth of 30ps. The RF linewidth follows the linewidth of the signal generator in all hybrid locking experiments. The pulse train in Figure 5.3 (c) shows a weak leading pulse which may be due to improper locking of some of the optical modes with the signal generator.

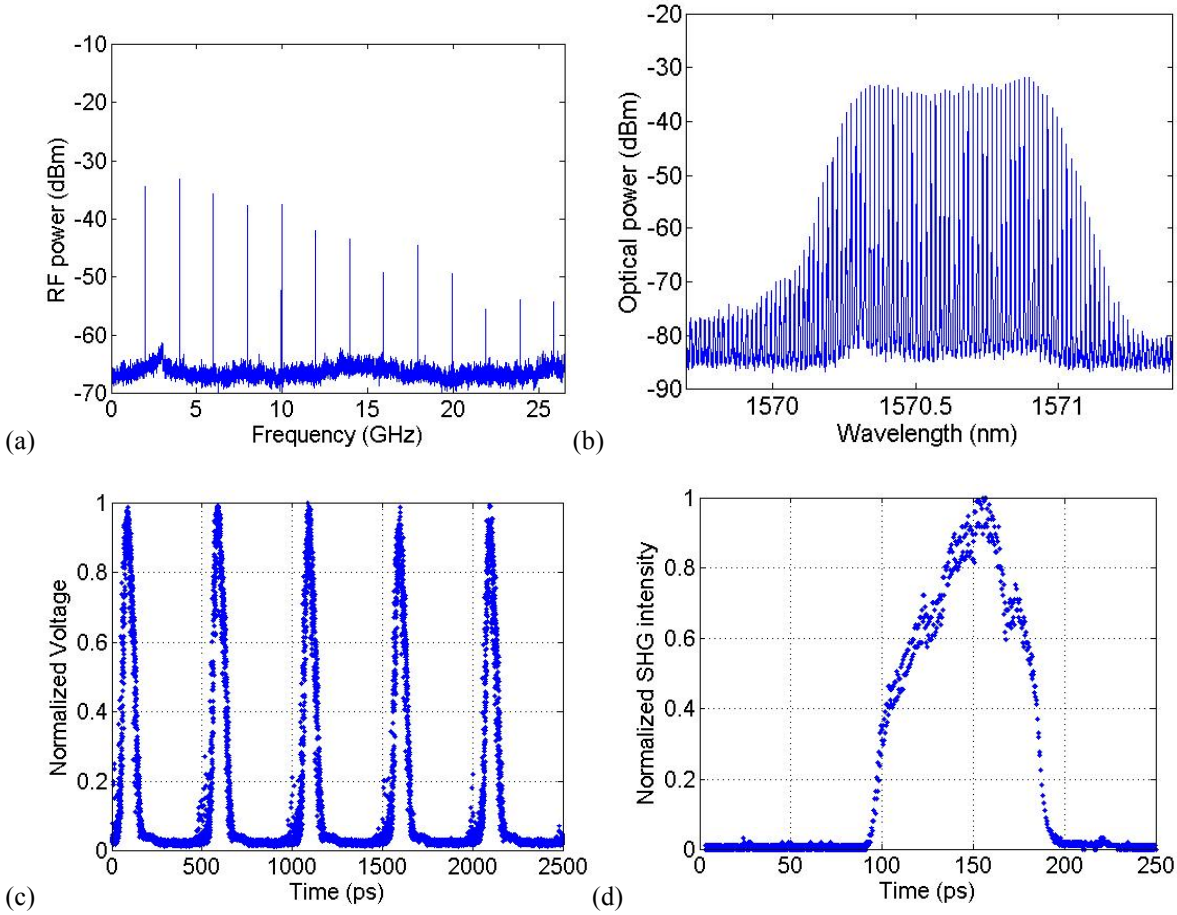


**Figure 5.3. Electrical spectrum (RBW – 3MHz) (a), optical spectrum (b), sampling oscilloscope trace (c) autocorrelator trace (d) for active locking at 2GHz. The bias conditions are same as in Figure 5.2. The RF power at the signal generator is 0dBm [23] © 2014 IEEE.**

We move on to study the MLLD when operated at its higher harmonics. Figure 5.4 and Figure 5.5 show data collected when the absorber was driven at two of the higher harmonics, 7.96GHz ($4^{th}$ harmonic) and 20GHz ($10^{th}$ harmonic) respectively. The best harmonic mode locking was seen at 7.96GHz, both in terms of pulse train quality and suppression of the fundamental tone (1.99GHz) on the ESA. The pulse width remains the same as in fundamental mode-locking case. However, the optical spectrum reveals that the power in the supermode noise spurs is significant compared to the power in the main group of modes, with only a 10dB reduction seen near the peak of the spectrum.

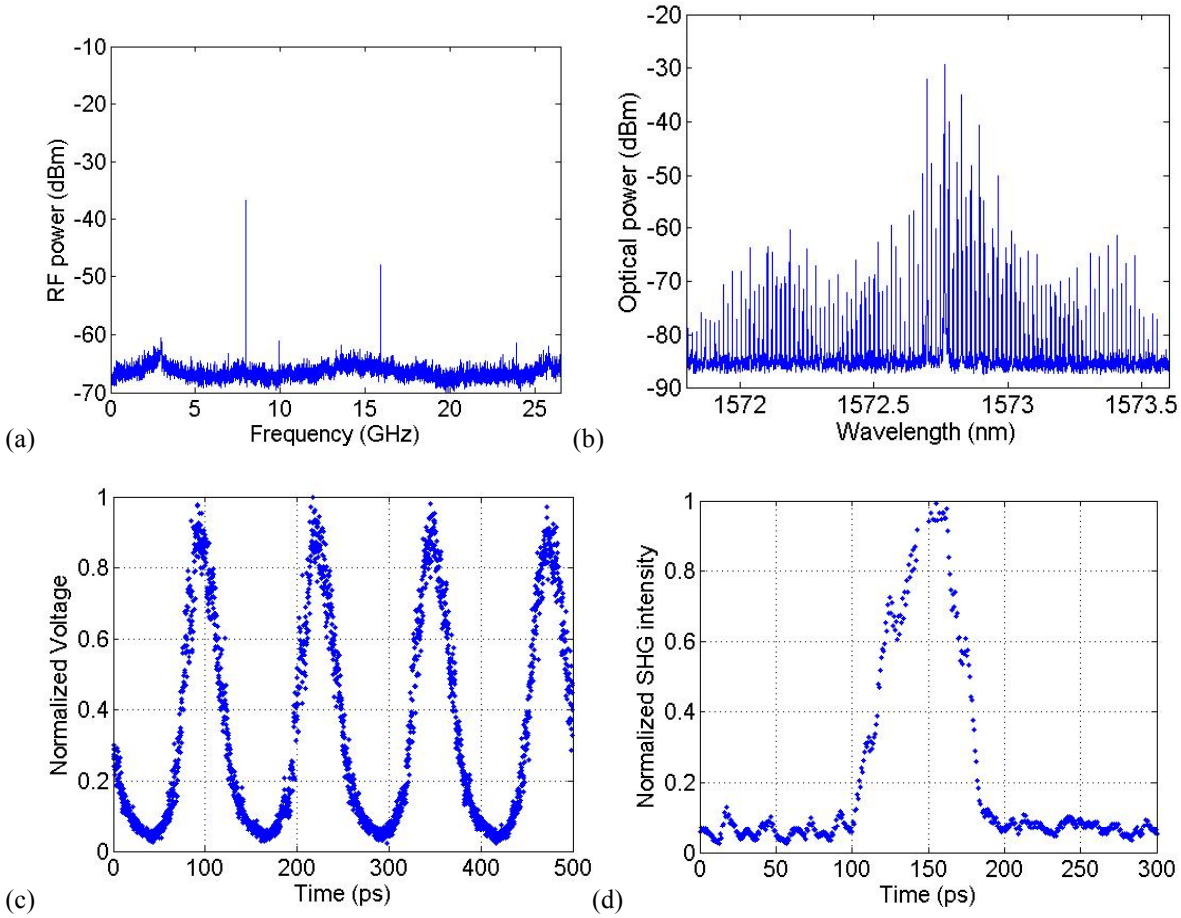


**Figure 5.4. Electrical spectrum (RBW – 3MHz) (a), optical spectrum (b), sampling oscilloscope trace (c) autocorrelator trace (d) for harmonic locking at 7.96GHz. The bias conditions are same as in Figure 5.2. The RF power at the signal generator is 0dBm [23] © 2014 IEEE.**

We were unable to obtain good electrical side-mode suppression ratio (SMSR) when the absorber was driven at other harmonics. This device behavior at different hybrid mode-locking frequencies can be explained by the following. Unlike a fundamentally mode-locked laser, the modes of a harmonically mode-locked laser may not be separated by the repetition rate i.e. the microwave drive frequency; the distribution of energy among the modes depends on the distribution of spectral phase [64]. In order to achieve perfect harmonic mode-locking the spectral phase has to be constant across all the modes. At the tenth harmonic we were required to increase the RF input power to 10dBm and achieved a maximum 25dB suppression of all other harmonics on the ESA. However, the optical spectrum shows near to

no suppression of the supermodes noise spurs. This shows the importance of the optical filter inside the cavity which was able to suppress the supermodes by 55dB when passively mode-locked.

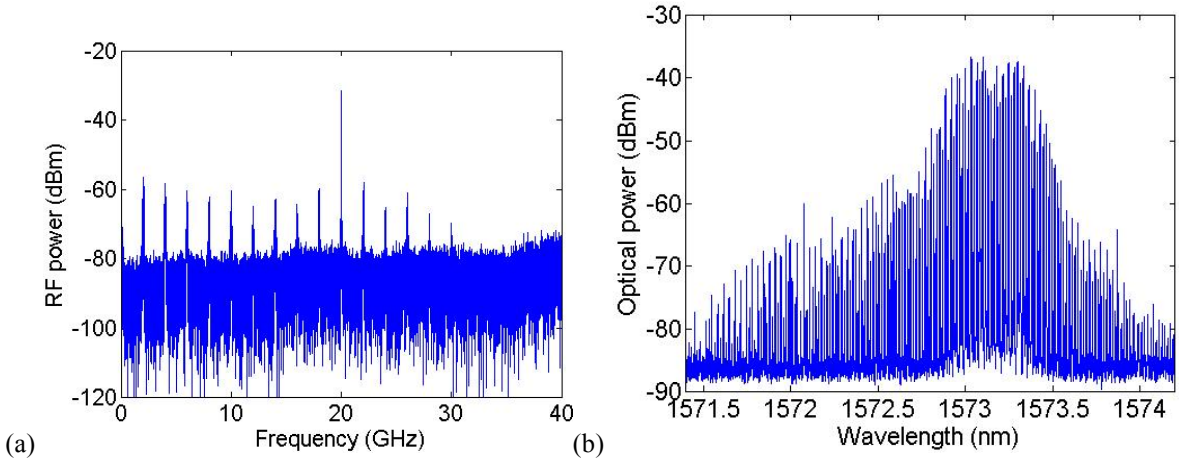


**Figure 5.5. Electrical spectrum (RBW – 3MHz) (a), optical spectrum (b), for harmonic locking at 20GHz. The SOA current is 206mA and the SA voltage is -1.4V. The RF power at the signal generator is 10dBm [23] © 2014 IEEE.**

In conclusion, a long cavity laser diode mode-locked using a saturable absorber was used to generate higher repetition rate pulses using an external microwave signal. Although the RF linewidth under hybrid locking is the same as that of the signal generator, the supermode noise is prohibitively large for generating low jitter signals. This is due to the broad timing window generated by the sinusoidal drive signal at the absorber which does not effectively filter the longitudinal modes with the wrong phase condition, and may be improved with a wave shaped electrical input that creates a sharp “pulse-like” timing window at the absorber.

The ideal way to re-distribute the photon energy into the desired longitudinal modes is through the introduction of a sharp wavelength selective periodic filter that modulate the cavity roundtrip loss for the different longitudinal modes of the laser. This helps to ensure that at steady state most of the new photons generated in the gain section through stimulated emission are at the desired frequency spacing. The periodic wavelength dependent loss was

introduced using a ring resonator in Chapter 2 and was shown to be very effective and requires very little power to passively tune the ring resonator, as opposed to wave shaping the microwave signal input.

# 6. Conclusions and Future Work

The objective of this thesis can be divided into two main parts. In the first part, we include the first demonstration of a fully integrated long cavity mode-locked laser and a fully integrated coupled cavity tunable laser. We also investigate two other techniques to lower optical or microwave phase noise which are lowering the number of quantum wells in the active region and by using all optical negative feedback. The key advantages of the techniques tested are simple design, compact footprint and low power consumption. The techniques are also photonic circuit based solutions and can be developed and optimized in parallel with the III-V diode design. Additionally, optical feedback techniques can provide noise reduction over a larger bandwidth compared electrical or opto-electronic feedback techniques. The summary of the various phase noise reduction demonstrations for mode-locked lasers and tunable lasers are presented in Section A and Section B respectively.

In the second part, we look at the reliability of distributed feedback (DFB) lasers fabricated using the recently developed hybrid silicon technology platform. The study was carried out to observe if the defects generated during the oxygen plasma assisted wafer bonding process can propagate to the multiple quantum well (MQW) active region over time and degrade the laser performance. The study also investigated the effect of adding strained layer superlattice near the bonded interface to block defect propagation. Accelerated aging tests were conducted on the lasers and the results are summarized in Section C. We finally end this chapter with some suggestions for future work.

### *A. Low Phase Noise Mode-Locked Lasers*

In Chapter 2, we demonstrate two main techniques to lower microwave phase noise in high repetition rate passively mode-locked lasers. First, we show a 14dB reduction in phase noise of a 20GHz signal by incorporating a long passive section inside the laser cavity to reduce the longitudinal confinement factor. We also show that adding a ring resonator into the cavity can successfully suppress the optical supermodes of the cavity spaced at the fundamental repetition rate of the long cavity by nearly 55dB. On the other hand, a sinusoidal microwave excitation of the saturable absorber using an external signal generator is not as effective in suppressing the supermodes of the long cavity as demonstrated in Chapter 5.

Second, we designed a laser with the long passive section, for lowering the longitudinal confinement factor, outside the laser main cavity to form a coupled cavity laser. The output optical power and threshold current are improved in this design, however, the reduction of phase noise from external feedback was limited to 6dB. The main limitation was from the spontaneous emission noise from the semiconductor optical amplifier (SOA) in the long feedback cavity. Furthermore, the SOA was converting most of the coherent photons in the pulse to incoherent ones with random optical phase.

In a second experiment, reducing transverse confinement factor by reducing the number of quantum wells from five to three was very effective as we observed nearly 8dB microwave phase noise improvement. In conclusion, reducing the transverse and longitudinal confinement factor are powerful techniques to lower optical phase noise in semiconductor mode-locked lasers and we have developed two fully integrated chip scale designs that can be used in the generation of high frequency and low jitter microwave signals.

### *B. Low Phase Noise Tunable Lasers*

In Chapter 3, we demonstrate two all-optical noise reduction techniques for tunable lasers, viz. on-chip delayed optical feedback and negative optical feedback using resonant mirror design. First, we demonstrated a widely-tunable semiconductor laser with monolithically integrated 4cm long external cavity, which narrows the laser linewidth by more than a factor of three. We have shown tuning in excess of 54nm around the O-band as well as record linewidths <100kHz across the whole tuning range. Once again the reduction was limited by the noise figure of the SOA in the feedback cavity. In a second laser design using resonant laser mirrors we identify a negative optical feedback effect that reduces the laser linewidth down to 160kHz. Both the techniques are wavelength independent effects i.e. linewidth reduction is possible in the entire tuning range. At optimum bias conditions for the laser, the coupled cavity improves the SMSR of the laser and uses only minimal additional electrical power. However, they do require precise control on the bias currents and voltages. Thus these two experiments provide evidence of significant optical phase noise reduction in semiconductor lasers by reducing longitudinal confinement factor and by incorporating resonant filters to provide negative optical feedback. Hybrid silicon platform is the underlying key technology that allows for implementation of these noise reduction strategies.

### *C. Reliability Study*

The aging tests conducted on DFB laser diodes and photodetectors on the hybrid silicon platform showed that dislocations are not the dominant failure mechanism. The laser diodes with a superlattice showed no significant degradation in threshold current after 5000hrs of aging at 70°C and 2500hrs at 85°C. 50% degradation in threshold current of some diodes at 70°C is estimated to take ~40000hrs. Most devices did not show any form of degradation,

and there was not a significant difference in lasers with or without strain in the superlattice and the control sample, in terms of aging. We did observe a difference in leakage current of photodiodes, indicating that devices that included the strained layer superlattice gives the minimum leakage current. We conclude that the platform is suitable for making reliable active optical devices, including lasers, modulators and photodetectors on silicon. Inclusion of a superlattice layer is beneficial in improving yield and keeping the photodetector dark current low.

### *D. Future Work*

Phase noise in high repetition rate semiconductor mode-locked lasers can be lowered further by going to fewer quantum wells in the active region along with an appropriate increase in absorber length. Reducing the taper reflections and eliminating higher order transverse or lateral modes in the gain section is essential in achieving a perfect Lorentzian phase noise spectrum. Removing the external cavity SOA in the coupled cavity laser configuration will help improve the RF linewidth. A design that has not been attempted in this thesis is the use of negative optical feedback using a resonant filter to lower phase noise in mode-locked lasers. This would require careful path length control to match the filter free spectral range (FSR) and a multiple of the repetition rate of the laser.

Next, with reference to lowering optical phase noise in semiconductor tunable lasers, the negative optical feedback technique deserves more attention. Using high quality factor (Q) resonators can bring down the linewidth of tunable lasers significantly. Coupled cavity lasers should be designed for high levels of feedback without any SOA in the feedback cavity to reduce additional spontaneous emission noise. The reflectivity of the mirror that is common

to the two coupled cavities can be made tunable to adjust the level of feedback and optimize for narrowest linewidth.

Finally, the reliability study can be extended to higher temperatures to look for other long term failure mechanisms. The devices that showed threshold current degradation did not show any increase in series resistance so the contacts and electrical diode characteristics are preserved. The DFB laser was not perfectly suited for a thorough electroluminescence (EL) study, however, preliminary EL images showed no dark line defects. Future investigation should consider either a dielectric failure mechanism or a simple Fabry-Perot laser with simple electrode design for EL study.

## Appendix 1. Temperature Effects on Photoluminescence

As an aside to the reliability study conducted on hybrid silicon lasers we also studied the effects of laser processing steps and high temperature metal contact anneal on the III-V material quality after bonding to an SOI wafer. We use photoluminescence (PL) to track any changes to the quantum wells. Experiment shows that the residual film stress after III-V-to-Si wafer bonding and thermal cycles during the device processing have little to no influence on the quantum well (QW) luminescence. However, as the interface is taken to higher contact anneal temperatures we see that the PL intensity drops below half its original value around 410$^{o}$C. At 440$^{o}$C, blisters start to appear on the surface and the III-V material has no residual luminescence.

The III-V device fabrication steps viz. dielectric deposition and metallization, involves thermal cycles at temperatures similar to or higher than the bonding temperature. After substrate removal, the strain is concentrated in the III-V epitaxial layers with multiple quantum well (MQW) active region. Thermal cycles or stress from deposited dielectric or metal can facilitate existing defects at bonding interface to propagate towards active region or generate new ones.

A square III-V material around 1cm$^2$ was bonded to a pre-patterned SOI chip. Detailed bonding process is discussed in Reference [4]. The III-V epitaxial layer structure is listed in Table A1.1. To simulate typical device fabrication steps, after substrate removal two cycles of 500nm $SiN_x$ deposition using Plasma-enhanced chemical vapor deposition (PECVD) followed by 30min reactive ion etching (RIE) to remove the $SiN_x$ layer, were performed. The temperature in the PECVD chamber is 265°C. Oxygen plasma descum at a power of 100W in the planar etcher was performed for 5min between each cycle. Finally, the sample was

heated in a rapid thermal annealer (RTA) with forming gas at 360°C for 30sec to simulate metal contact anneal.

**TABLE A1.1**
**Material composition and thickness of all layers in the overlying III-V material (top to bottom), after substrate removal.**

| III-V epitaxial layers | |
|---|---|
| Material composition of each layer | Layer thickness(nm) |
| P - $In_{0.53}Ga_{0.47}As$ | 100 |
| P - InP | 1500 |
| Upper SCH - $In_{0.5289}Al_{0.166}Ga_{0.3051}As$ | 150 |
| Quantum Well (×10) - $In_{0.4884}Al_{0.015}Ga_{0.4966}As$ | 11 |
| Barrier (×11) - $In_{0.5702}Al_{0.284}Ga_{0.1458}As$ | 7 |
| Lower SCH - $In_{0.5284}Al_{0.193}Ga_{0.2786}As$ | 100 |
| N - InP | 100 |
| Superlattice - $In_{0.85}Ga_{0.15}As_{0.327}P_{0.673}$ (×2)<br>InP (×2) | 7.5 each |
| Bonding layer - InP | 10 |

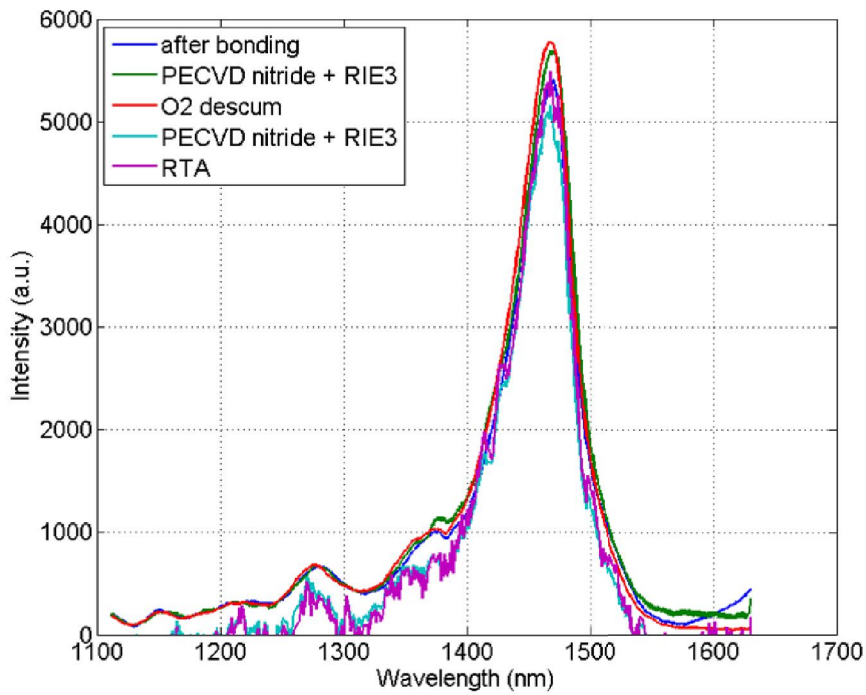


**Figure A1. 1. Median photoluminescence spectrum across the 1cm$^2$ bonded region after each process step.**

Photoluminescence (PL) is used to measure variation in wavelength, intensity and full-width at half maximum (FWHM) of transferred MQWs. The pump power, slit width,

number of grating lines and shutter open time were held constant in all measurements at 0.5mW, 500µm, 150 and 400ms, respectively. Figure A1. 1 shows the median PL spectrum, across the 1cm$^2$ sample, after each process step. The PL peak wavelength remains the same at 1467.4nm with the standard deviation improving from 3.3nm to 2.3nm. The FWHM reduces from 57nm to 52nm with significant reduction in standard deviation from 11nm to 7nm. The PL intensity shows similar improvement with the standard deviation of the log normal distribution going from 0.34 to 0.24. This is similar to previously observed MQW PL improvement when comparing transferred III-V epilayers with as grown wafer [10]. Additional thermal cycles at reasonable temperature range help annihilate epitaxial growth defects. This also suggests that the hybrid III-V on Si platform can sustain the stress, both thermal and mechanical, during a device process run. The small improvements in the distribution of the PL spectrum across the sample indicate the possibility of maintaining uniform device performance and high yield.

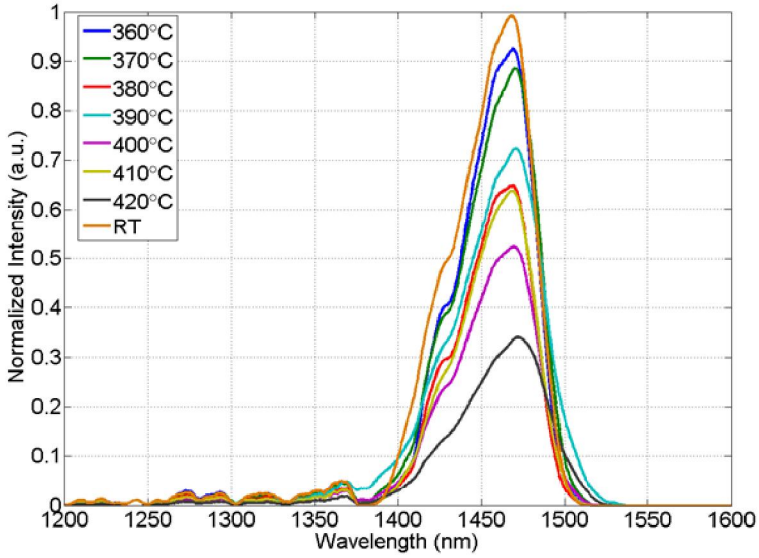


**Figure A1. 2. Normalized photoluminescence spectra from the bonded sample, at 10°C increments from 360°C to 420°C. RT - room temperature.**

Good ohmic contact on InP requires high doping or anneal around 400$^{o}$C which is much higher than bonding anneal temperature (300$^{o}$C) and PECVD process temperature (265$^{o}$C). Previously fabricated hybrid Si devices were all metalized at 350-360$^{o}$C. In order to study if bonded sample can sustain higher anneal temperature, another bonded sample with the substrate removed was cleaved into 7 pieces, one for each anneal temperature from 360°C to 420°C in steps of 10°C in the RTA. The temperature of each sample is increased linearly to the set temperature in 20sec and held for 30sec. The sample is then brought to room temperature gradually.

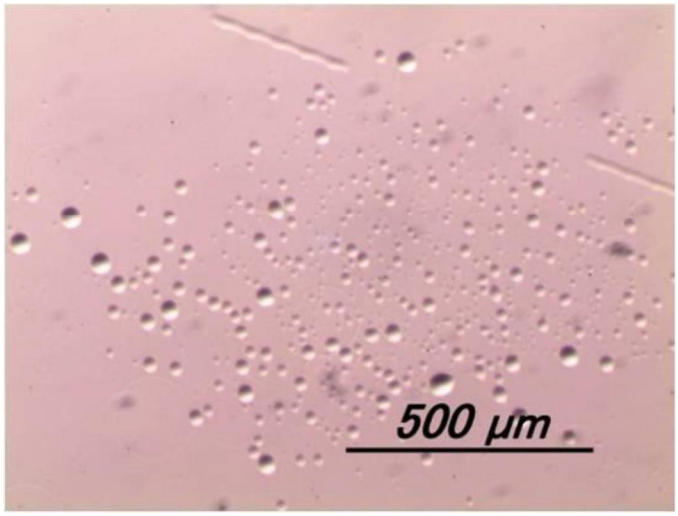


**Figure A1. 3. Blister formation on the surface when annealed at 440°C for 30sec in a forming gas environment.**

The PL spectrum for each temperature, shown in Figure A1. 2, is normalized with their respective spectrum taken before annealing. We observe no change in PL peak wavelength with rising temperature, showing no change in the ground state for electrons and holes in the quantum well. The PL intensity and FWHM degrade progressively until 420°C, beyond which no PL signal is observed. Furthermore, for temperatures above 440°C the surface is decorated with blisters (~20µm in diameter) showing permanent plastic deformation of the III-V material in Figure A1. 3. The safe region for high temperature operation for this

platform is below 370°C. This is the temperature at which the PL intensity falls to 90% of the value after bonding. The PL intensity of the as-grown III-V wafer annealed at 440°C without bonding showed no change, confirming that the degradation originates from thermal stress at the bonding interface.

The PL degradation and blister formation on III-V surface are primarily due to the excessive thermal stress at the bonding interface caused by the expanding gasses trapped in between the III-V and Si layers. The gasses are mainly hydrogen and water vapor, generated during the bonding process as polymerization by-products. Chong et al. [65] have shown that the temperature limit of 440°C observed in this work can be surpassed by using in-plane out-gassing channels rather than vertical out-gassing channels.

In conclusion, experimental evidence on the effects of thermal stress on hybrid III-V-on-Si bonded samples, using photoluminescence, is presented. There is little effect on the luminescence of the active region after wafer bonding and during post-bond device fabrication where maximum temperature is 360$^{o}$C. Post-bond thermal cycles with temperature above 370$^{o}$C results in obvious PL degradation. Plastic deformation is observed on III-V epitaxial layers at temperatures above 440$^{o}$C.

## Appendix 2. Coupled Opto-Electronic Oscillator

In this section we demonstrate the feasibility of using a hybrid silicon mode-locked laser (MLL) in a coupled optoelectronic oscillator (COEO) configuration for generating a 20GHz microwave signal. The COEO is a special case of regenerative mode-locking, where the gain in the opto-electronic feedback loop is unity and the phase is 2π. This condition gives rise to two coupled oscillators. The benefit being that the cavity lengths of the two oscillators can be quite dissimilar and the oscillator with the shorter cavity derives the stability from the longer cavity and can be used to suppress microwave or optical phase noise. However, the length of the longer cavity is limited by the filtering quality of the short cavity. If the mode spacing of the longer cavity is smaller than the filtering provided by the short cavity oscillator we generate supermodes that degrade phase noise.

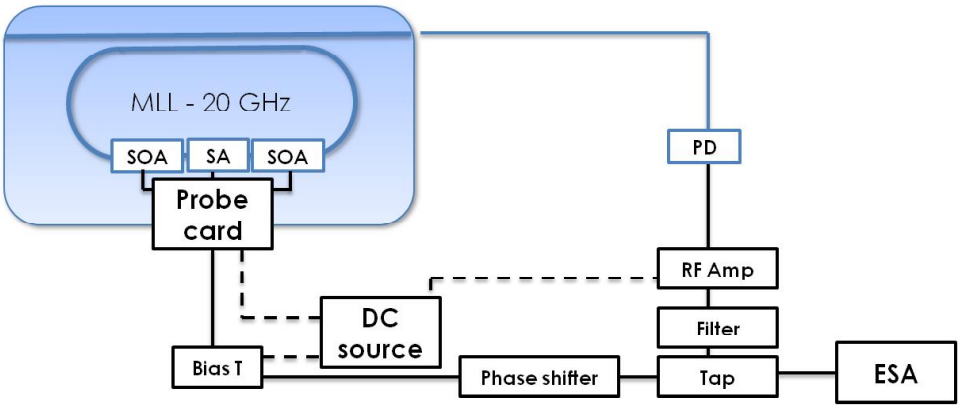


**Figure A2. 1. Circuit schematic of the COEO using a hybrid silicon mode-locked laser chip. PD-Photodetector, ESA-Electrical spectrum analyzer.**

Figure A2. 1 shows the schematic of the COEO circuit. It includes a ring laser cavity fabricated on a silicon-on-insulator (SOI) substrate with a hybrid section that provides gain. This is the same short cavity ring laser described in Chapter 2, Section B. The cavity length is designed for a repetition rate of 20GHz and includes a 50μm long saturable absorber (SA) in the center of the semiconductor optical amplifier (SOA), which is isolated from the gain

regions using proton implants. The set point for the SOA drive current was 189mA and the saturable absorber (SA) bias was 0V, a mode-locked regime for the laser. The optical power from the laser is facet coupled out using a 2µm spot size fiber. We use a commercial u2t photodetector with 50GHz bandwidth and a responsivity of 0.55A/W. The optical power reaching the detector is ~1mW. The microwave filter has a bandwidth of 400MHz centered at 20GHz and the small signal RF gain of the amplifier is 42dB. We use a 14dB electrical tap to analyze the microwave signal.

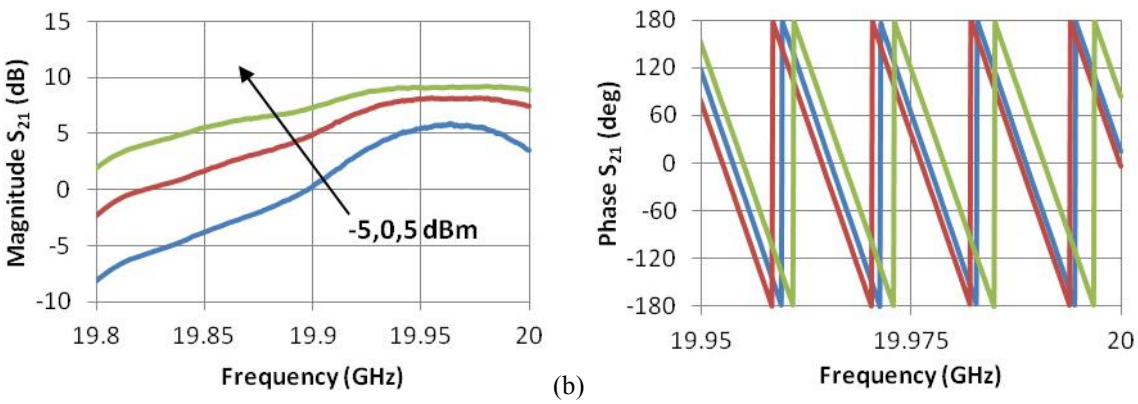


**Figure A2. 2. Measured magnitude (a) and phase (b) open loop response ($S_{21}$) for different launch power, measured by breaking the loop in Figure A2. 1 after the phase shifter.**

Figure A2. 2 shows the open-loop $S_{21}$ for this oscillator circuit at three different input RF powers using an HP lightwave component analyzer, 8703A. The bandwidth change directly corresponds to the locking range for the mode-locked laser. The $S_{21}$ curves show the Barkhausen criteria for phase being met for several modes within the RF filter bandwidth. The main frequency selection mechanism comes from the locking range of the mode-locked laser. Figure A2. 3 shows the RF spectrum and phase noise of the free-running oscillator. The instantaneous 3dB line-width is 14kHz with a signal to noise ratio >50dB. The spurs in the phase noise plot originate from the various competing fiber modes in the oscillator's feedback loop. For comparison, we also included the phase noise of the short and

harmonically locked long cavity laser, from Chapter 2, to show the continuous improvement achievable with longer passive sections in optical or opto-electronic cavities. The improvement with ~10m external feedback cavity length at 1MHz is ~30dB. The only drawback being that the filters are not narrow enough to suppress the competing longitudinal modes completely.

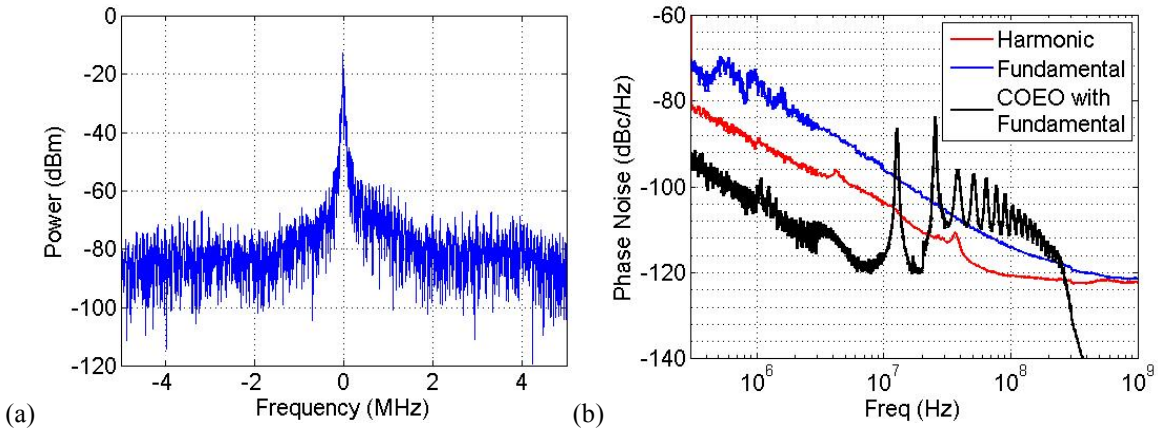


**Figure A2. 3. (a) RF spectrum centered at 19.96GHz and (b) Phase noise vs. frequency offset from the carrier for three different microwave photonic oscillators.**

The frequency stability and microwave side-mode-suppression can be enhanced by incorporating a high quality-factor (Q) resonator in the laser cavity [40, 66] or a second opto-electronic feedback path of different length. In a COEO the Q seen by the microwave oscillator is enhanced beyond the intrinsic loaded Q of the resonator because of gain in the laser cavity and hence can substitute the need for long lengths of fiber.

In conclusion, we have demonstrated a photonic microwave oscillator using the hybrid silicon mode-locked laser with ~30dB improvement in microwave phase noise at 1MHz offset from the carrier. The advantage of optical techniques for generation of microwave signals, as opposed to electrical techniques, is that the phase noise does not increase with signal frequency. The phase noise in photonic oscillators is dominated by spontaneous emission noise and is independent of the microwave frequency, however, electrical

oscillators have more noise at higher frequencies due to increasing propagation losses. Therefore, reducing spontaneous emission noise in photonic oscillators is necessary to make high microwave frequency low phase noise oscillators.

## References


[1] A. S. Jordan, "Some thermal and mechanical properties of InP essential to crystal growth modeling," *Journal of Crystal Growth,* vol. 71, pp. 559-565, 1985/6// 1985.

[2] Y. Okada and Y. Tokumaru, "Precise determination of lattice parameter and thermal expansion coefficient of silicon between 300 and 1500 K," *Journal of Applied Physics,* vol. 56, pp. 314-320, 1984.

[3] H. Wada and T. Kamijoh, "Room-temperature CW operation of InGaAsP lasers on Si fabricated by wafer bonding," *Photonics Technology Letters, IEEE,* vol. 8, pp. 173-175, 1996.

[4] D. Liang and J. E. Bowers, "Highly efficient vertical outgassing channels for low-temperature InP-to-silicon direct wafer bonding on the silicon-on-insulator substrate," *Journal of Vacuum Science and Technology B,* vol. 26, pp. 1560-1568, 2008.

[5] P. Rojo Romeo, J. Van Campenhout, P. Regreny, A. Kazmierczak, C. Seassal, X. Letartre, G. Hollinger, D. Van Thourhout, R. Baets, J. M. Fedeli, and L. Di Cioccio, "Heterogeneous integration of electrically driven microdisk based laser sources for optical interconnects and photonic ICs," *Optics Express,* vol. 14, pp. 3864-3871, 2006.

[6] G. Roelkens, D. Van Thourhout, R. Baets, R. Nötzel, and M. Smit, "Laser emission and photodetection in an InP/InGaAsP layer integrated on and coupled to a Silicon-on-Insulator waveguide circuit," *Optics Express,* vol. 14, pp. 8154-8159, 2006.

[7] A. W. Fang, H. Park, O. Cohen, R. Jones, M. J. Paniccia, and J. E. Bowers, "Electrically pumped hybrid AlGaInAs-silicon evanescent laser," *Optics Express,* vol. 14, pp. 9203-9210, 2006.

[8] L. A. Coldren, S. W. Corzine, and M. L. Mašanović, "Dynamic Effects," in *Diode Lasers and Photonic Integrated Circuits*: John Wiley & Sons, Inc., pp. 247-333.

[9] C. H. Henry, "Theory of the linewidth of semiconductor lasers," *Quantum Electronics, IEEE Journal of,* vol. 18, pp. 259-264, 1982.

[10] D. Liang, J. E. Bowers, D. C. Oakley, A. Napoleone, D. C. Chapman, C.-L. Chen, P. W. Juodawlkis, and O. Raday, "High-Quality 150 mm InP-to-Silicon Epitaxial Transfer for Silicon Photonic Integrated Circuits," *Electrochemical and Solid-State Letters,* vol. 12, pp. H101-H104, April 1, 2009 2009.

[11] P. W. Juodawlkis, J. C. Twichell, G. Betts, J. J. Hargreaves, R. D. Younger, J. L. Wasserman, F. J. O'Donnell, K. G. Ray, and R. C. Williamson, "Optically sampled analog-to-digital converters," *Microwave Theory and Techniques, IEEE Transactions on,* vol. 49, pp. 1840-1853, 2001.

[12] M. D. S. Srinivasan, M. J. R. Heck, J. Hutchinson, E. Norberg, G. Fish, J. Bowers, "Low phase noise hybrid silicon mode-locked lasers," *Front. Optoelectron.,* vol. 7, pp. 265-276, 2014-09-09.

[13] R. Rosales, K. Merghem, A. Martinez, A. Accard, F. Lelarge, and A. Ramdane, "High repetition rate two-section InAs/InP quantum-dash passively mode locked lasers," in *Compound Semiconductor Week (CSW/IPRM), 2011 and 23rd International Conference on Indium Phosphide and Related Materials*, pp. 1-4.

[14] L. A. Jiang, K. S. Abedin, M. E. Grein, and E. P. Ippen, "Timing jitter reduction in modelocked semiconductor lasers with photon seeding," *Applied Physics Letters,* vol. 80, pp. 1707-1709, 2002.

[15] L. Drzewietzki, S. Breuer, and W. Elsäßer, "Timing jitter reduction of passively mode-locked semiconductor lasers by self- and external-injection: Numerical description and experiments," *Optics Express,* vol. 21, pp. 16142-16161.

[16] L. Chang-Yi, F. Grillot, L. Yan, R. Raghunathan, and L. F. Lester, "Microwave Characterization and Stabilization of Timing Jitter in a Quantum-Dot Passively Mode-Locked Laser via External Optical Feedback," *Selected Topics in Quantum Electronics, IEEE Journal of,* vol. 17, pp. 1311-1317.

[17] G. Fiol, M. Kleinert, D. Arsenijevi, and D. Bimberg, "1.3 μm range 40 GHz quantum-dot mode-locked laser under external continuous wave light injection or optical feedback," *Semiconductor Science and Technology,* vol. 26, p. 014006.

[18] T. Yilmaz, C. M. Depriest, A. Braun, J. H. Abeles, and P. J. Delfyett, "Noise in fundamental and harmonic modelocked semiconductor lasers: experiments and simulations," *Quantum Electronics, IEEE Journal of,* vol. 39, pp. 838-849, 2003.

[19] S. Cheung, J.-H. Baek, F. M. Soares, R. P. Scott, X. Zhou, N. K. Fontaine, M. Shearn, A. Scherer, D. M. Baney, and S. J. B. Yoo, "Super-Long Cavity, Monolithically Integrated 1-GHz Hybrid Mode-Locked InP Laser for All-Optical Sampling," in *Integrated Photonics Research, Silicon and Nanophotonics and Photonics in Switching*, Monterey, California, p. PWD2.

[20] S. Latkowski, V. Moskalenko, S. Tahvili, M. Smit, E. Bente, and L. Augustin, "Monolithic 2.5 GHz Quantum Well InGaAsP Extended Cavity Modelocked Ring Laser with an Integrated Phase Modulator," in *Semiconductor Laser Conference (ISLC), 2014 International*, pp. 62-63.

[21] M. J. R. Heck, M. L. Davenport, P. Hyundai, D. J. Blumenthal, and J. E. Bowers, "Ultra-long cavity hybrid silicon mode-locked laser diode operating at 930 MHz," in *Optical Fiber Communication (OFC), collocated National Fiber Optic Engineers Conference, 2010 Conference on (OFC/NFOEC)*, pp. 1-3.

[22] H. K. Tsang, C. S. Wong, T. K. Liang, I. E. Day, S. W. Roberts, A. Harpin, J. Drake, and M. Asghari, "Optical dispersion, two-photon absorption and self-phase modulation in silicon waveguides at 1.5μm wavelength," *Applied Physics Letters,* vol. 80, pp. 416-418, 2002.

[23] S. Srinivasan, A. Arrighi, M. J. R. Heck, J. Hutchinson, E. Norberg, G. Fish, and J. E. Bowers, "Harmonically Mode-Locked Hybrid Silicon Laser With Intra-Cavity Filter to Suppress Supermode Noise," *Selected Topics in Quantum Electronics, IEEE Journal of,* vol. 20, pp. 8-15.

[24] E. J. M. Bente, Y. Barbarin, M. R. Heck, and M. Smit, "Modeling of integrated extended cavity InP/InGaAsP semiconductor modelocked ring lasers," *Optical and Quantum Electronics,* vol. 40, pp. 131-148, 2008.

[25] J. F. Bauters, M. J. R. Heck, D. D. John, J. S. Barton, C. M. Bruinink, A. Leinse, R. G. Heideman, D. J. Blumenthal, and J. E. Bowers, "Planar waveguides with less than 0.1 dB/m propagation loss fabricated with wafer bonding," *Optics Express,* vol. 19, pp. 24090-24101.

[26] M. Piels, J. F. Bauters, M. L. Davenport, M. J. R. Heck, and J. E. Bowers, "Low-Loss Silicon Nitride AWG Demultiplexer Heterogeneously Integrated With Hybrid

III-V/Silicon Photodetectors," *Lightwave Technology, Journal of,* vol. 32, pp. 817-823.

[27] P. Hyundai, A. W. Fang, O. Cohen, R. Jones, M. J. Paniccia, and J. E. Bowers, "A Hybrid AlGaInAs - Silicon Evanescent Amplifier," *Photonics Technology Letters, IEEE,* vol. 19, pp. 230-232, 2007.

[28] J. P. Tourrenc, S. O'Donoghue, M. T. Todaro, S. P. Hegarty, M. B. Flynn, G. Huyet, J. G. McInerney, L. O'Faolain, and T. F. Krauss, "Cross-Correlation Timing Jitter Measurement of High Power Passively Mode-Locked Two-Section Quantum-Dot Lasers," *Photonics Technology Letters, IEEE,* vol. 18, pp. 2317-2319, 2006.

[29] P. Langlois, D. Gay, N. McCarthy, and M. Piché, "Noise reduction in a mode-locked semiconductor laser by coherent photon seeding," *Optics Letters,* vol. 23, pp. 114-116, 1998.

[30] M. L. Davenport, s. srinivasan, M. J. R. Heck, and J. E. Bowers, "A Hybrid Silicon/InP Integrated All-Passive Feedback Stabilized Mode-Locked Laser," in *Optical Fiber Communication Conference*, San Francisco, California, p. Th3A.5.

[31] F. Kefelian, S. O'Donoghue, M. T. Todaro, J. G. McInerney, and G. Huyet, "RF Linewidth in Monolithic Passively Mode-Locked Semiconductor Laser," *Photonics Technology Letters, IEEE,* vol. 20, pp. 1405-1407, 2008.

[32] T. L. Koch and U. Koren, "Semiconductor lasers for coherent optical fiber communications," *Lightwave Technology, Journal of,* vol. 8, pp. 274-293, 1990.

[33] M. Seimetz, "Laser Linewidth Limitations for Optical Systems with High-Order Modulation Employing Feed Forward Digital Carrier Phase Estimation," in *Optical Fiber communication/National Fiber Optic Engineers Conference, 2008. OFC/NFOEC 2008. Conference on*, 2008, pp. 1-3.

[34] R. Lang and K. Kobayashi, "External optical feedback effects on semiconductor injection laser properties," *Quantum Electronics, IEEE Journal of,* vol. 16, pp. 347-355, 1980.

[35] G. P. Agrawal and C. H. Henry, "Modulation performance of a semiconductor laser coupled to an external high-Q resonator," *Quantum Electronics, IEEE Journal of,* vol. 24, pp. 134-142, 1988.

[36] J. Mork, B. Tromborg, and J. Mark, "Chaos in semiconductor lasers with optical feedback: theory and experiment," *Quantum Electronics, IEEE Journal of,* vol. 28, pp. 93-108, 1992.

[37] A. Laakso and M. Dumitrescu, "Modified rate equation model including the photon-photon resonance," *Optical and Quantum Electronics,* vol. 42, pp. 785-791.

[38] A. Konosuke, Y. Ryuichi, Y. Nobuhide, K. Wataru, and Y. Hiroshi, "Experimental demonstration of linewidth reduction of laser diode by compact coherent optical negative feedback system," *Applied Physics Express,* vol. 7, p. 122701.

[39] L. B. Mercer, "1/f frequency noise effects on self-heterodyne linewidth measurements," *Lightwave Technology, Journal of,* vol. 9, pp. 485-493, 1991.

[40] J. F. Bauters, M. L. Davenport, M. J. R. Heck, J. K. Doylend, A. Chen, A. W. Fang, and J. E. Bowers, "Silicon on ultra-low-loss waveguide photonic integration platform," *Optics Express,* vol. 21, pp. 544-555.

[41] L. Bin, A. Shakouri, and J. E. Bowers, "Wide tunable double ring resonator coupled lasers," *Photonics Technology Letters, IEEE,* vol. 14, pp. 600-602, 2002.

[42] K. Sato, N. Kobayashi, M. Namiwaka, K. Yamamoto, T. Kita, H. Yamada, and H. Yamazaki, "High output power and narrow linewidth silicon photonic hybrid ring-

filter external cavity wavelength tunable lasers," in *Optical Communication (ECOC), 2014 European Conference on*, pp. 1-3.

[43] J. C. Hulme, J. K. Doylend, and J. E. Bowers, "Widely tunable Vernier ring laser on hybrid silicon," *Optics Express,* vol. 21, pp. 19718-19722.

[44] S. Keyvaninia, G. Roelkens, D. Van Thourhout, C. Jany, M. Lamponi, A. Le Liepvre, F. Lelarge, D. Make, G.-H. Duan, D. Bordel, and J.-M. Fedeli, "Demonstration of a heterogeneously integrated III-V/SOI single wavelength tunable laser," *Optics Express,* vol. 21, pp. 3784-3792.

[45] T. Creazzo, E. Marchena, S. B. Krasulick, P. K. L. Yu, D. Van Orden, J. Y. Spann, C. C. Blivin, L. He, H. Cai, J. M. Dallesasse, R. J. Stone, and A. Mizrahi, "Integrated tunable CMOS laser," *Optics Express,* vol. 21, pp. 28048-28053.

[46] J. H. Lee, I. Shubin, J. Yao, J. Bickford, Y. Luo, S. Lin, S. S. Djordjevic, H. D. Thacker, J. E. Cunningham, K. Raj, X. Zheng, and A. V. Krishnamoorthy, "High power and widely tunable Si hybrid external-cavity laser for power efficient Si photonics WDM links," *Optics Express,* vol. 22, pp. 7678-7685.

[47] C. Zhang, S. Srinivasan, Y. Tang, M. J. R. Heck, M. L. Davenport, and J. E. Bowers, "Low threshold and high speed short cavity distributed feedback hybrid silicon lasers," *Optics Express,* vol. 22, pp. 10202-10209.

[48] C. Youngchul, K. Doo-Gun, and N. Dagli, "Reflection properties of coupled-ring reflectors," *Lightwave Technology, Journal of,* vol. 24, pp. 1865-1874, 2006.

[49] O. Schwelb, "Band-limited optical mirrors based on ring resonators: analysis and design," *Lightwave Technology, Journal of,* vol. 23, pp. 3931-3946, 2005.

[50] I. Chremmos and O. Schwelb, "Optimization, bandwidth and the effect of loss on the characteristics of the coupled ring reflector," *Optics Communications,* vol. 282, pp. 3712-3719, 2009.

[51] P. Dong, T.-C. Hu, T.-Y. Liow, Y.-K. Chen, C. Xie, X. Luo, G.-Q. Lo, R. Kopf, and A. Tate, "Novel integration technique for silicon/III-V hybrid laser," *Optics Express,* vol. 22, pp. 26854-26861.

[52] M. Popovic, C. Manolatou, and M. Watts, "Coupling-induced resonance frequency shifts in coupled dielectric multi-cavity filters," *Optics Express,* vol. 14, pp. 1208-1222, 2006.

[53] M. K. Lee, D. S. Wuu, and H. H. Tung, "Heteroepitaxial growth of InP directly on Si by low pressure metalorganic chemical vapor deposition," *Applied Physics Letters,* vol. 50, pp. 1725-1726, 1987.

[54] M. Sugo, H. Mori, M. Tachikawa, Y. Itoh, and M. Yamamoto, "Room temperature operation of an InGaAsP double heterostructure laser emitting at 1.55 μm on a Si substrate," *Applied Physics Letters,* vol. 57, pp. 593-595, 1990.

[55] D. Liang, D. Chapman, Y. Li, D. Oakley, T. Napoleone, P. Juodawlkis, C. Brubaker, C. Mann, H. Bar, O. Raday, and J. Bowers, "Uniformity study of wafer-scale InP-to-silicon hybrid integration," *Applied Physics A,* vol. 103, pp. 213-218.

[56] A. W. Fang, E. Lively, Y.-H. Kuo, D. Liang, and J. E. Bowers, "A distributed feedback silicon evanescent laser," *Optics Express,* vol. 16, pp. 4413-4419, 2008.

[57] Y. Tang, J. D. Peters, and J. E. Bowers, "Over 67 GHz bandwidth hybrid silicon electroabsorption modulator with asymmetric segmented electrode for 1.3 μm transmission," *Optics Express,* vol. 20, pp. 11529-11535.

[58] H. Park, A. W. Fang, R. Jones, O. Cohen, O. Raday, M. N. Sysak, M. J. Paniccia, and J. E. Bowers, "A hybrid AlGaInAs-silicon evanescent waveguide photodetector," *Optics Express,* vol. 15, pp. 6044-6052, 2007.

[59] B. Koch, A. Alduino, L. Ling, R. Jones, M. Morse, B. Kim, L. Wei-Zen, J. Basak, L. Hai-Feng, R. Haisheng, M. Sysak, C. Krause, R. Saba, D. Lazar, L. Horwitz, R. Bar, S. Litski, L. Ansheng, K. Sullivan, O. Dosunmu, N. Na, Y. Tao, F. Haubensack, I. w. Hsieh, J. Heck, R. Beatty, J. Bovington, and M. Paniccia, "A 4x12.5 Gb/s CWDM Si photonics link using integrated hybrid silicon lasers," in *Lasers and Electro-Optics (CLEO), 2011 Conference on*, pp. 1-2.

[60] M. Sugo, H. Mori, Y. Sakai, and Y. Itoh, "Stable cw operation at room temperature of a 1.5μm wavelength multiple quantum well laser on a Si substrate," *Applied Physics Letters,* vol. 60, pp. 472-473, 1992.

[61] J.-S. Huang, "Temperature and current dependences of reliability degradation of buried heterostructure semiconductor lasers," *Device and Materials Reliability, IEEE Transactions on,* vol. 5, pp. 150-154, 2005.

[62] S. Srinivasan, N. Julian, J. Peters, L. Di, and J. E. Bowers, "Reliability of Hybrid Silicon Distributed Feedback Lasers," *Selected Topics in Quantum Electronics, IEEE Journal of,* vol. 19, pp. 1501305-1501305.

[63] D. Liang, S. Srinivasan, J. Peters, A. Fang, and J. E. Bowers, "Demonstration of Enhanced III-V-On-Silicon Hybrid Integration by Using a Strained Superlattice as a Defect Blocking Layer," *ECS Transactions,* vol. 33, pp. 421-426, October 1, 2010.

[64] F. Quinlan, S. Ozharar, S. Gee, and P. J. Delfyett, "Harmonically mode-locked semiconductor-based lasers as high repetition rate ultralow noise pulse train and optical frequency comb sources," *Journal of Optics A: Pure and Applied Optics,* vol. 11, p. 103001, 2009.

[65] C. Zhang, D. Liang, and J. E. Bowers, "MOCVD Regrowth of InP on Hybrid Silicon Substrate," *ECS Solid State Letters,* vol. 2, pp. Q82-Q86, January 1, 2013.

[66] D. T. Spencer, J. F. Bauters, M. J. R. Heck, and J. E. Bowers, "Integrated waveguide coupled Si3N4 resonators in the ultrahigh-Q regime," *Optica,* vol. 1, pp. 153-157.